# INVESTIGATION OF BARIUM STRONTIUM SODIUM NIOBATE FERROELECTRICS AND CALCIUM MAGNESIUM SILICATE PHOSPHOR NANOMATERIALS FOR OPTOELECTRONICS APPLICATIONS

SOLOMON HAILEMARIAM DIDU

**SUPERVISORS:**

1. PROFESSOR MENBERU MENGESHA (PHD)
2. DR.NEBIYU GEMECHU (ASSO. PROF., PHD)

JIMMA, ETHIOPIA
JUNE, 2024

# INVESTIGATION OF BARIUM STRONTIUM SODIUM NIOBATE FERROELECTRICS AND CALCIUM MAGNESIUM SILICATE PHOSPHOR NANOMATERIALS FOR APPLICATIONS

SOLOMON HAILEMARIAM DIDU

A dissertation submitted to Department of Physics in fulfillment of the requirements for the degree of Doctor of Philosophy, in Physics.
at
Jimma University

# Confirmation of evaluation board whether the dissertation meets the accepted standard with respect to originality and quality.

”Investigation of Barium Strontium Sodium Niobate Ferroelectrics and Calcium Magnesium Silicate Phosphor Nanomaterials for Optoelectronics Applications”.

Solomon Hailemariam

This manuscript has been read and accepted for the Graduate Study in Physics in satisfaction of the dissertation requirement for the degree of Doctor of Philosophy.

Advisor: __________, Signature: __________,Date: __________

Co-Advisor: __________, Signature: __________,Date: __________

Examiner: __________, Signature: __________,Date: __________

Examiner: __________, Signature: __________,Date: __________

# Jimma University
# Department of Physics

This is to certify that the dissertation prepared by **Solomon Hailemariam Didu** Graduate studies entitled **”Synthesis and Investigation of Barium Strontium Sodium Niobate Ferroelectrics and Calcium Magnesium Silicate Phosphor Nanomaterials for Device Applications”** in fulfillment of the requirements for the Degree of DOCTOR OF PHILOSOPHY IN PHYSICS Complies with the regulations of the University and meet the accepted standards with respect to originality and Quality.

Professor Menberu Mengesha (PhD) June 12, 2024
Advisor Signature Date

Dr.Nebiyu Gemechu(Assoc.Prof,PhD) June 12, 2024
Co-Advisor Signature Date

Professor Abebe Belay (PhD) June 12, 2024
External Examiner Signature Date

Professor Olu Emmanuel (PhD) June 12, 2024
Internal Examiner Signature Date

(Dr.Tolu Biressa) June 12, 2024
Chairman Signature Date

JIMMA UNIVERSITY

Date: June 12, 2024

Author: **Solomon Hailemariam Didu**

Title: **Investigation of Barium Strontium Sodium Niobate Ferroelectrics and Calcium Magnesium Silicate Phosphor Nanomaterials for Optoelectronics Applications**.

Department: **Physics**

Degree: **PhD**. Convocation: **June 12** Year: **2024**

Permission is herewith granted to Jimma University to circulate and to have copied for non-commercial purposes, at its discretion, the above title upon the request of individuals or institutions.

Signature of Author———————-

# Acknowledgement

This journey would not have been possible without the support and help from many people. Five years of Ph.D. student life seems intimidating, but every moment is memorable not because of my scientific achievement (if there is any) but the experience shared with my family, friends and colleagues.

First, I would like to thank the Almighty GOD. It is only due to his blessings that I have been able to accomplish this work. I feel extremely grateful for pursuing my doctoral degree at the Jimma University, where I worked with the best scientists and mentors one could imagine. My deepest thanks go to my advisors, professor Menberu Mengesha and dr.Nebiyu Gemechu, who does not only guide me throughout the highs and lows of this process, patiently and encouragingly, but also always inspires me as a role model. I am indebted to their wealth of knowledge and devotion to education. Next I would like to deliver my deepest gratitude again to my supervisors, for their dedication, encouragement and outstanding scientific support during the whole doctoral program and this PhD dissertation work. Special thanks to professor Menberu Mengesha and dr.Nebiyu Gemechu for insightful scientific suggestions, discussions, and support during publication process.

I would also like to thank the committee members dr.Tolu Birressa and dr.Solomon Negash for their valuable guidance and participation in this dissertation.

I would like to thank all staff members in the physics department and Mr.Surapaneni Beheemswara Rao (India) for their supports and good discussions during my study and this PhD dissertation in particular without their help this work would not have come to this level. Then I would like to express my special gratitude to my wife Kezina Aba Zinab and children Abel, Kidus and Kety Solomon for their endless love, moral and economical support throughout the study (First Degree to PhD program study).

Finally I would like to express my deepest gratitude to:

- Professor Daniel Erenenso, Tenasse State University (USA) for purchasing chemical from Sigma-Aldrich Company USA.
- Mr.Mezgebe Getahun (USA) for chemical purchasing from Sigma-Aldrich Company USA.
- Dr.Fuad Abduro (China) for SEM and EDS Scanning
- Dr.Shimelis Addisu (Jimma University) for Installing softwatres and skill transfer
- Dr.Shimelis Lemma, Mr. Demeke Tesfaye (Adama Science and Technology University) for characterization of samples XRD, UV-Vis and PL Laboratory work.
- Professor Paulos Tadesse, Dr.Sintayehu Mekonnin and Mr.Kassahun Lewetegn (Arbaminch University) for Synthesis of samples Laboratory work.
- M/ss Titina Mulat (USA) for moral and financial support
- My Brothers Kifle, Sintayhu, Mera and Shambel Biniam Hailemariam and sisters Kelemua and Lome Hailemariam for their continuous moral and financial support
- Special thanks to my mother for her endless Mother's love and unwaved moral and financial support from Diploma to PhD program study acting as mother and father.
- Last but not least I extended my gratitude to Jimma University for the opportunity and financial support.
- Lastly I duely acknowledge my friends: Zemach Mamo, Wasihun Wolde, Kasahun Tesema, Woldegiorgis Gissa, Wolde Lema, Abebe and all others I donot list, for consistent moral and different supports during my travel for laboratory works.

# Abstract

This is a study report of rare earth Holmium ion additive Barium Strontium Sodium Niobate ($Ba_{(1.6-3/2X)}Sr_{2.4}Na_2Nb_{10}O_{30} : xHo^{3+}$) tungsten bronze structured ferroelectrics nanomaterial by conventional solid state reaction routes using Barium Carbonate ($BaCO_3$), Strontium carbonate ($SrCO_3$), Sodium Carbonate ($Na_2CO_3$) 99.90% NICE, and Niobium Oxide ($Nb_2O_5$) and Holmium oxide ($Ho_2O_3$) 99.99% Sigma-Aldrich as starting materials under normal stoichiometric ratio synthesis approach. The X-ray diffraction (XRD), the scanning electron spectroscopy (SEM), energy dispersive x-ray spectroscopy (EDS) and Fourier transform- infrared spectroscopy (FTIR) were used to study the structure, surface morphology/ microstructure, elemental composition/mapping and finger print functional groups identification respectively. The XRD pattern revealed Tetragonal Tungsten Bronze structured crystallite phase that best match with the JCPDS card number -00-039-1453 having space group of p4bm and lattice parameters of a = 12.33 $\mathring{A}$, b = 12.33 $\mathring{A}$ and c = 3.93 $\mathring{A}$. The average crystallite size of the synthesized sample obtained at the prominent peak (311) for position/$2\theta$=32.320 is 67.52 nm. The SEM images showed that surface microstructures have random and nearly uniform distribution of nanoparticles with different shapes and size on the surface. It is also nearly non-porous surface microstructure that is promising for enhancing optical properties having more particles on the surface. EDS analysis confirmed the presence of all the constituent elements with their proportional ratios of Wt.% and At %. EDS experimental results best fit with theoretically calculated values. For the pure metal oxide the FTIR results showed the bond vibration mode at wavenumber of 540.60 cm$^{-1}$, having only single collective metal oxide intense peak without impurities. When $Ho^{3+}$ or (ions) with concentration of 0.05 and 0.10 % added additional peaks was observed at 429.92 cm$^{-1}$ and 415.77 cm$^{-1}$ respectively; confirming the existence of

Ho-O bond vibration modes.

This dissertation work also aimed to report a study on the UV-Vis and Photoluminescence behaviors of rare earth holmium additive barium strontium sodium niobate ferroelectrics nanomaterials, produced by conventional high temperature solid-state reaction methods. The investigation included, UV-Vis, PL to examine the absorption and emission respectively. The UV-Vis revealed that the maximum absorption occurred at wavelength of 205 nm having highest intensity value obtained for the amount of 0.03 $Ho^{3+}$ and diminished in both directions. The PL result displayed the maximum emission spectra (322.8 a.u.) centered at wavelength of 572 nm for the excitation wavelength of 285 nm for 0.03 $Ho^{3+}$. Moreover, the synthesized nanomaterial is highly promising for optoelectronic applications as the results obtained from characterized parameters clearly indicated.

Calcium magnesium silicate was synthesized via sol-gel route using calcium carbonate $(CaCO_3)$, magnesim carbonate $(MgCO_3)$ and Stenotaphrum secundatum grass extract (in place of tetraethylorthosilicate - TEOS) as a starting materials. The x-ray diffraction (XRD), Fourier Transform Infra-Red Spectroscopy (FTIR), UV Visible (UV-Vis), Photoluminescence's (PLs) as well as scanning electron microscopy (SEM) and energy dispersive x-ray spectroscopy (EDX) were used to study the phase composition, functional groups identification, absorption spectra determination, examining excitation and emission spectra, surface morphology /microstructure and elemental composition analysis or mapping of the calcined product. The XRD analysis shows that the synthesized samples have tetragonal Calcium Magnesium Silicate - akermanite structure. FTIR confirmed the existence of the functional groups by $(Si-O-Si, Si-O, O-Ca-O, O-Mg-O, SiO4, Ca^{2+}, Mg^{2+})$ symmetric stretch, asymmetric stretch, vibrational mode and bending mode in the synthesized samples. UV-Vis revealed the occurrences of maximum absorption at wavelength of 280 nm and it increases in intensity with increasing its $Nb^{5+}$ concentration. PL also shows maximum emission at excitation wavelength of 280 nm at wavelength of 564 nm with emission intensity of 866 a.u. for concentration of 1.0 % $Nb^{5+}$. In PL analysis, we observe the intensity of emission increasing with increasing concentration of $Nb^{5+}$. SEM images shows that surface microstructures have porous, flux structures and EDX analysis confirmed the presence of all the constituent elements.

.

# ACRONYMS

- **TB** - Tungsten Bronze
- **TTB**- Tetragonal Tungsten Bronze
- **TTBs**- Tetragonal Tungsten Bronze structure
- **PT** - Lead Titanate
- **PZT**- Titanate Zirconate of Lead
- **MPB**- Morphotropic Phase Boundary
- **TC** - Transition Temperature
- **PBN**- Lead Barium Niobate
- **PLZT**- Lead Lanthanium Zirconate Titanate
- **SBN** - Strontium Barium Niobate
- **VO** - Oxygen Vacancy
- **XRD** - X-Ray Diffraction
- **SEM** - Scaning Elecron Microscopy
- **EDS/EDX**- Energy Dispersive X-Ray Spectroscopy
- **FTIR** - Fourier Transform Infrared Spectroscopy
- **TEM** - Transition Electron Microscope
- **EELS** - Electron Energy Loss Spectroscopy
- **TGA** - Thermogravitrometric Analysis
- **PL** - Photoluminescence
- **UV-VIS** - Ultra-Violet Vissible Spectroscopy
- **BSNN:xH**- $Ba_{(1.6-3/2X)}Sr_{2.4}Na_2Nb_{10}O_{30} : xHo^{3+}$

# Contents

# List of Figures

# List of Tables

# 1

# INTRODUCTION

## 1.1 Motivation

### Ferroelectric ceramics with tungsten bronze structure

Ferroelectricity a revolutionary century of discovery: A century after the discovery of ferroelectricity, we look at the physics that makes ferroelectrics materials so useful and the research that got us here. Ferroelectrics play very important roles in the field of electronic materials due to their wide applications in piezoelectric, pyroelectric, optoelectric and nonlinear optic devices. Pb-free ferroelectric materials have attracted the increasing scientific and commercial interests due to the serious environmental concerns [1-4]

Ferroelectrics are a very important family of functional materials, and they have received attention from a variety of fields, including material science, condensed matter physics and electrical engineering [1, 5-11]. Applications of ferroelectric materials are primarily governed by their polarization response to external stimuli. Due to the nature of domains, ferroelectrics exhibit hysteresis phenomena with respect to an external electric field. Classic ferroelectrics have a single P-E hysteresis loop, which represents field-controlled transitions between two equivalent ferroelectric states with different polarization directions [12]. Switchable polarizations under an electric field allow ferroelectrics to be used in memory and logic devices [13].

TUNGSTEN BRONZE oxides compose the largest dielectric family just next to the perovskites. Tungsten-bronze compounds have been considered as candi-

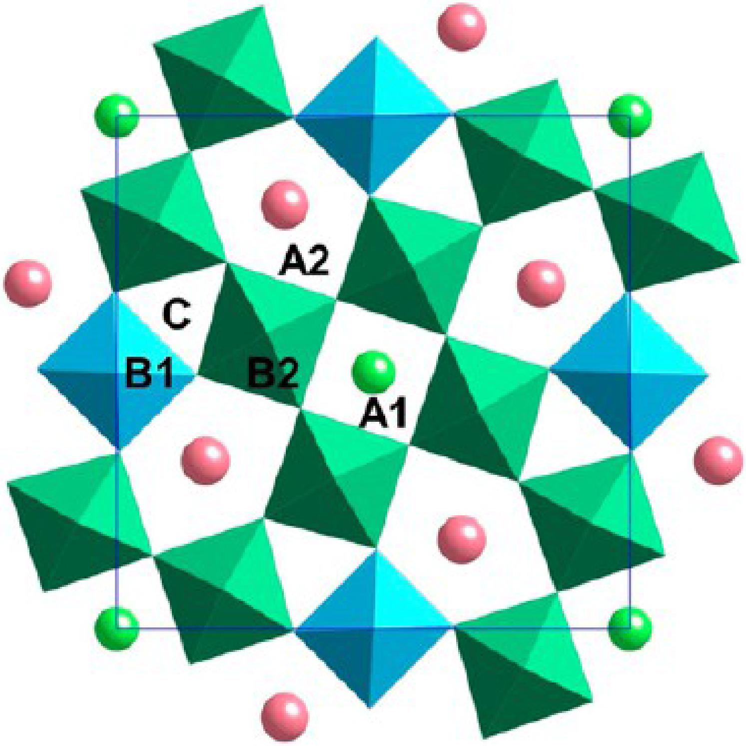

Figure 1.1: [001] Projection of the prototype tetragonal tungsten bronze structure illustrating the interstices described by the corner sharing octahedral [19]

dates to replace lead-based compounds. It is not very surprising that crystals with the tungsten- bronze structure are ferroelectric. As shown in Figure 1.1, the tungsten bronze structure is composed of ten distorted octahedral sharing corners in such a way that three different interstices (A1, A2, and C) are available for cation occupying in the general formula $(A1)_2(A2)_4(C)_4(B1)_2(B2)_8O_{30}$ [14]. The full-filled tungsten bronzes such as $K_3Li_2Nb_5O_{15}$ have attracted much attention for the nonlinear optic applications,[15, 16] whereas the nonfilled tungsten bronzes have been well studied due to their unique ferroelectric and piezoelectric characteristics [17, 18].

The octahedra of TB are linked by corners and are thus bonded in a way similar to the perovskites [20]. The unit cell is one octahedron tall in the c direction; and since there are ten octahedra in the cell, the axis is approximately.$\sqrt{10}$ times an octahedron width. Thus $\sqrt{10}$ a/c$\approx$1. The deviation from this value is a measure of the distortions of the $NbO_6$ octahedra and can be related [21] to the value of the spontaneous polarization P and the transition temperature $T_c$.

A-sites are occupied by mono to trivalent cations, B-sites are occupied by tetra-hexavalent ions and C-sites are often empty, are complex and disordered. It has been found very useful for many device applications. The properties of these types of materials can be tailored by making suitable modifications/substitutions at A, B or C sites. TB formula consists of A1, A2, C and B is 15, 12, 9 and 6-fold Oxygen coordinated sites in the crystal [22].

Recently, $M_4R_2Ti_4M'_6O_{30}$ and $M_5RTi_3M'_7O_{30}$ (M = Ba and Sr, R = Bi, La, Nd, and $Sm, M'$ = Ta and Nb) ceramics with filled tungsten bronze structure have received much scientific attention on their interesting dielectric and ferroelectric characteristics [23-26]. At room temperature, the filled tungsten bronze tantanates are usually paraelectric, whereas the filled tungsten bronze niobates are all ferroelectrics. $M_5RTi_3Nb_7O_{30}$ were usually considered as relaxor ferroelectrics due to the cross distribution of M and R ions in A1 site (tetragonal), and $M_4R_2Ti_4Nb_6O_{30}$ tended to indicate the normal ferroelectric nature due to their ordered structure in which M and R ions properly occupy the A2 (pentagonal) and A1 (tetragonal) sites, respectively [27, 28]. However, recent investigations found that $Ba_4La_2Ti_4Nb_6O_{30}$ [29-33] and $Sr_4La_2Ti_4Nb_6O_{30}$ [34, 35] etc. indicated the relaxor behavior, whereas $Sr_4Nd_2Ti_4Nb_6O_{30}$ [36] presented a diffuse ferroelectric phase transition followed by two low-temperature dielectric relaxations. Stennett et. al. and Levinet. al. reported the important effects of the ionic radius of rare-earth ion in A1 site on the dielectric behavior in $Ba_2MTi_2Nb_3O_{15}(M = Bi, La, Nd, Sm, Gd)$ [30] and $Ba_2(La_xNd_{1-x})Ti_2Nb_3O_{15}$ [31] ceramics. Meanwhile, the same autor's who researched on $(Ba_xSr_{1-x})_4Nd_2Ti_4Nb_6O_{30}$ [36] indicated that the ferroelectric transition in $M_4R_2Ti_4Nb_6O_{30}$ was not only affected by the ionic radius of rare-earth ion but also by the ionic radius of alkali ion. Moreover, the radius difference between A1- and A2-site cations dominated the dielectric nature of $M_4R_2Ti_4Nb_6O_{30}$ tungsten bronzes. Compounds with larger radius difference between A1- and A2-site cations tend to be normal ferroelectric, whereas compounds with smaller radius difference between A1- and A2-site cations tend to be relaxor ferroelectric.

It was also found that some of the oxides with distorted perovskite structure have complex but stable structure at room temperature with many interesting properties useful for devices. Out of them some materials with tungsten bronze (TB) structure have been found more favourable for high dielectric constant [37], electro optic [38], pyroelectric [39], piezoelectric [40], nonlinear optic [5], acousto-optic [41], photo-refractive [42] etc. devices. Most of the TB structure belongs to tetragonal or orthorhombic structure with small distortion of multiple perovskites. Some tungsten bronze ferroelectric ceramics are found to be stable at room temperature with diffuse phase transition and relaxor behavior. Also, structural flexibility and chemical versatility of these materials make them more suitable for device applications.

Currently, inorganic phosphor materials have drawn out a lot of attention because of their multiple applications, for instance, in cathode-ray tubes, photodiodes, lamps, and x-ray detectors, bio-detectors, color display, radiation dosimetry and dye removal [43-47]. Among the inorganic phosphor materials, silicate based became a lot of attention drawn materials for wide and multi-dimensional practical applications due to their unique features such as visible light transparency, good chemical resistance, high temperature strength, low thermal expansion, excellent conductivity, well known chemical and thermal stability, low cost and easy preparation [48, 49].

## 1.2 Statement of the problem

It has been a very important issue to search Lead (Pb)-free ferroelectric new materials because of the increasing environmental concerns, and the tungsten bronze family might provide the great potential for this challenge due to the various possibility of structural tailoring. More and more attentions are being paid to the ceramics with tungsten bronze (TB) structure [14-18] by many researchers, because of their potential technological superiority. Many TTBs display broad, frequency-dependent relaxor dielectric behavior rather than sharper frequency-independent normal ferroelectric anomalies, but the exact reasons that favor a particular type of dielectric response for a given composition remain unclear.

Recently, $M_4R_2Ti_4M_6O_{30}$ and $M_5RTi_3M_7O_{30}$ (M = Ba and Sr, R = Bi, La, Nd, and Sm, M = Ta and Nb) ceramics with filled tungsten bronze structure have received much scientific attention on their interesting dielectric and ferroelectric characteristics [23, 24, 26].

The flexibility of the structure of TB- oxides opens new rooms for non-lead based ferroelectric nanomaterials. In a look for lead-free novel materials for the development of new nanomaterials, TTBs are among attractive candidates. The various positive ion sites in the TTB structure permit for a wide range of chemical compositions, compositional flexibility and consequently for opening the possibility of controlling the main characteristics features of TTBs [50-53]. Taking into account the preliminary research outputs reported so far, the current studies revolve across the potential application of nanomaterials for imparting photoluminescence (PL) in materials [54, 55]. In addition, rare earth based crystals which follow the guest-host phenomenon to independently optimize the luminescence and crystal properties of the system has given due attention. It was also considered and focused as a central point in the system [56]. Rare earth oxides under the wide energy bandgap semiconductor have also drawn special attention due to their tunable electronic and optical characteristics features [57]. As a result of these remarkable features, the prepared ferroelectric nanomaterials and their characteristic photoluminescence response with various concentrations at different excitation wavelengths are in need of clear explanation. Again, the detailed mechanisms that tune the luminescence of nanomaterials of ferroelectrics types are not yet fully understood.

In the synthesis of silicate based phosphor materials, tetraethyl-orthosilicate (TEOS) is a primary precursor. Due to its high scarcity in most developing countries and difficulty to import it as well make the challenge magnified. This has been also a bottleneck for the growth of researches focusing on silicate based inorganic phosphor materials in such countries. Therefore, a new mechanism should be designed to alleviate this problem [58, 59]. Stenotaphrum secundatum grass is reported to be reach in silica [60] and it is widely available in almost all countries in the world. However, whether the extract of this grass can be used as a precursor for the synthesis of silicate based inorganic phosphors instead of TEOS is not really examined. Under this context, this statement of problem expected to answer the following basic research questions:

- What are the effects of the concentration of Holmium ions in the synthesized Barium Strontium Sodium Niobates with rare earth Holmium additive Ferroelectric Tungsten Bronze structure new material?
- How one determines the role of micro-structure/Elemental composition (SEM/EDS) and dopants/substitutes in ferroelectric Barium Strontium Sodium Niobates tungsten bronze structured with rare earth Holmium ion additive of different Concentrations?
- What are the characterization instruments and parameters used to determine Ferroelectric Tungsten Bronze structures system phase (XRD), functional group (FTIR), absorption (Uv-Vis) and photoluminescence (PL) values in tuning and controlling the properties for efficient device applications?
- What are the characterization instruments and parameters used to determine Calcium Magnesium Silicate crystal structures phase (XRD), functional group (FTIR), absorption (Uv-Vis) and photoluminescence (PL) values in tuning and controlling the properties for efficient device applications?

## 1.3 Objectives

### 1.3.1 General Objective

- To synthesis and Characterize Tungsten Bronze Structured Barium Strontium Sodium Niobate Ferroelectric and Calcium Magnesium Silicate Phosphor nanomaterials for Device Applications.

### 1.3.2 Specific Objectives

- To synthesis $Ba_{(1.6-3/2x)}Sr_{2.4}Na_2Nb_{10}O_{30} : xHo^{3+}$ for(x=0.00- 0.10 %)samples using solid state reaction techniques.

- To identify the crystal structure and crystallite size of the prepared samples $Ba_{(1.6-3/2x)}Sr_{2.4}Na_2Nb_{10}O_{30} : xHo^{3+}$ or (BSNN:xH) for (x=0.00- 0.10 %) using XRD.

- To determine surface Morphology, element types and composion of prepared samples (BSNN:xH) for (x=0.00- 0.10 %) using SEM/EDS.

- To determine absoption capacity of the powder solution samples (BSNN:xH) for (x=0.00- 0.10 %) using UV-Vis spectrometer.

- To identify the finger print functional groups (4000-400 cm-1) of the system (BSNN:xH) for (x=0.00- 0.10 %) using FTIR.

- To determine the photoluminescence property of the $Ba_{(1.6-3/2x)}Sr_{2.4}Na_2Nb_{10}O_{30} : xHo^{3+}$ with different concentration (x=0.00-0.10 %) using PL.

- To synthesis $(Ca_2MgSi_2O_7 : xNb^{5+})$ samples using Sol-gel route techniques.

- To determine the crystal structure and crystallite size of the prepared samples $(Ca_2MgSi_2O_7 : xNb^{5+})$ for (x=0.02, 0.04, 0.06 and 0.10 %) using XRD.

- To determine surface Morphology, element types and composion of prepared samples $(Ca_2MgSi_2O_7 : xNb^{5+})$ for (x=0.02, 0.04, 0.06 and 0.10 %) using SEM/EDS.

- To determine absoption property of the powder samples $(Ca_2MgSi_2O_7 : xNb^{5+})$ for (x=0.02, 0.04, 0.06 and 0.10 %) using UV-Vis spectrometer.

- To determine the photoluminescence property of the $(Ca_2MgSi_2O_7 : xNb^{5+})$ with different concentration (x=0.02, 0.04, 0.06 and 0.10 %) using PL.

## 1.4 Significance and Scope of the study

This research output would benefits experts to design efficient nanomaterials for device applications from Barium Strontium Sodium Niobates with rare earth additive(s) ferroelectric with Tungsten Bronze structure. The phosphor nanomaterials are very useful economical utility in medicine for treating damaged bones.It may serve as base for further study on the same topic, and to realize technological application in industrial scale production of ceramic materials with optimized efficiency. Meanwhile, the study is also delimited to synthesis and characterization of Barium Strontium Sodium Niobates with rare earth additive(s) ferroelectric Tungsten Bronze structure system experimentally.

## 1.5 Thesis Layout

Chapter 2 deals with the brief overview on Ferroelectrics and ferroelectrics nano-materials properties in general and TBs materials in particular. The mechanism of ferroelectrics, tetragonal tungsten bronze structured ferroelectrics and the different dopants effects, vacancies and sites occupation are discussed. In chapter 3, the different experimental techniques used for synthesis and characterization are discussed in detail. The main results of this study in chapters 4, 5, 6 and 7 are discussed. Chapter 4 deals with Synthesis and Characterization of $Ba_{(1.6-3/2x)}Sr_{2.4}Na_2Nb_{10}O_{30} : xHo^{3+}$ Ferroelectric nanomaterials by Solid state reaction routes for Device Applications. Investigation of Barium Strontium Sodium Niobate Ferroelectric nanomaterial with Holmium ion additive for Optoelectronic Application is covered in chapter 5. Green Synthesis of Niobium doped Calcium Magnesium Silicate Phosphor Using Stenotaphrum Secundatum Grass Extract discussed in chapter 6 and Finally, the summary conclusion and future directions are included in chapter 7.

# 2

# A Brief overview of Tungsten Bronze Structured Ferroelectrics

## 2.1 Ferroelectrics Materials

A ferroelectric material is one which exhibits spontaneous polarization in the absence of electric field, which may be switched in direction by application of electric field. Ferroelectric shows electrical properties like magnetic properties in ferromagnetic materials. Barium titanate, lead titanate (PT), titanate zirconate of lead (PZT), etc. are widely used and scrutinized as ferroelectric materials [61]. For instance, Safari presented a review of the basic concepts on ferroelectricity and various materials which possess electric and magnetic properties [62]. Ferroelectric materials have unique dielectric, pyroelectric, piezoelectric and electro-optic properties. These properties have various applications in capacitors, dielectric resonators, sensors, transducers, actuators, and ferroelectric non-volatile memories, dielectric memories, optical waveguides, displays, micro electro mechanical systems (MEMS), miniaturized mechanical and electro-mechanical elements [63-67]. Based on their distinctive properties, ferroelectric materials have been used to produce active elements of various devices [68, 69]. Thus the main focus on ferroelectric materials as compared to non-ferroelectric materials is due to their compact size and high dielectric constant.

## 2.2 Ferroelectrics Tungsten Bronzes

Pb-free ferroelectric materials have attracted increasing scientific and commercial interests due to serious environmental concerns. The structural flexibility of tungsten bronze oxides offers more opportunities for exploiting new Pb-free ferroelectric materials. The tetragonal tungsten bronze structure is composed of ten distorted octahedral sharing corners in such a way that three different interstices (2 tetragonal A1, 4 pentagonal A2, and 4 triangle C) are available for cations in the general formula $(A1)_2(A2)_4(C)_4(B1)_2(B2_8O_{30}$ [70]. In recent years, a number of Pb-free ferroelectrics with tetragonal tungsten bronze structures have been determined [19, 30, 31, 71, 72]. For $M_4R_2Ti_4Nb_6O_{30}$ and $M_5RTi_3Nb_7O_{30}$ (M= Ba, Sr; R = rare earth), their phase transition nature and ferroelectric properties strongly depend on the cation occupation and the difference in the radius between the A2 and A1 cations [19, 71]. $M_4R_2Ti_4Nb_6O_{30}$ (M= Ba, Sr; R = $Nd^{3+}$, $Sm^{3+}$, $Eu^{3+}$) tends to exhibit normal ferroelectric phase transitions due to its ordered structure. $M^{2+}$ occupies the pentagonal A2 site, and $R^{3+}$ is in the tetragonal A1 sites [30, 31, 72-77]. For compositions with larger R cations, a relaxor nature is observed in $Ba_4Bi_2Ti_4Nb_6O_{30}$ and $Ba_4La_2Ti_4Nb_6O_{30}$ [30, 62]. For $M_5RTi_3Nb_7O_{30}$ (M= Ba, Sr; R = rare earth), relaxor ferroelectric behavior is generally observed, and it is ascribed to the cross distribution of $M^{2+}$ and $R^{3+}$ cations at A1 (tetragonal) sites [78, 79]. A detailed structural study indicated that the relaxor nature is always associated with in-commensurate superlattice modulation. The decrease in the R cation size increases the driving force for commensurate superlattice modulation, which dominates the normal ferroelectric nature [19, 30, 31, 71].

More recently, the filled tungsten bronze ferroelectrics $M_4R_2Ti_4Nb_6O_{30}$ and $M_5RTi_3Nb_7O_30$ (M = Ba, Sr; R = rare earth) have received much scientific attention due to their unique and interesting ferroelectric properties [27, 28, 31, 32, 36, 71, 73, 78, 80-82]. The ferroelectricity in these materials is believed to come from the off-center displacements of B-site ions both along c-axis and in ab plane, and the ferroelectric ordering may affected by (1) oxygen octahedral tilting, (2) A-site cations

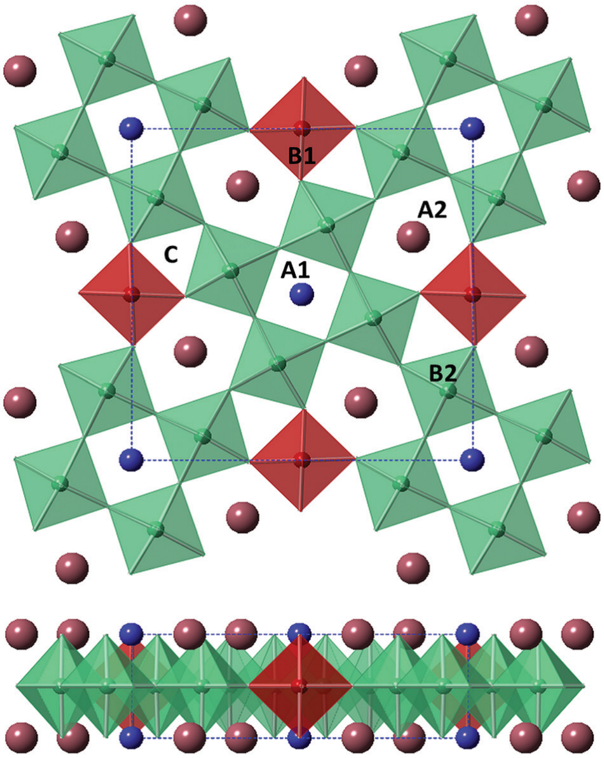

Figure 2.1: Tetragonal tungsten bronze (TTB) structure (space group P4/mbm) viewed along [001] (top) and [100] (bottom). Oxygen octahedral contains B1-cations (red) and B2-cations (green), respectively, with the unit cell indicated by blue dashed lines [83].

occupation, and (3) B-site cations occupation.

## 2.3 Structure Stability and General Formula of Filled Tungsten Bronzes

The structure stability of filled tungsten bronze can be discussed by the tolerance factor. Wakiya et al.[84] have suggested the tolerance factors for 12-fold coordination A1 site and 15-fold coordination A2 site given by the following equations:

$$t_{A1} = \frac{r_{A2} + r_O}{\sqrt{2}(r_B + r_O)} \tag{2.1}$$

$$t_{A2} = \frac{r_{A2} + r_O}{\sqrt{32 - 12\sqrt{3}}(r_B + r_O)} \tag{2.2}$$

$$t = \frac{2t_{A2} + t_{A1}}{3} \tag{2.3}$$

Where, $r_A$, $r_B$, and $r_O$ are the ionic radii of the $A-$ and $B-$ site ions and the $O^{2-}$ ion, respectively. The combination of these tolerance factors denoted as following gives a general measure to determine the structure stability of tungsten bronzes. The compositions with a $t$ around 1.00 can form a stable tungsten bronze structure, whereas the stable tungsten bronze structure cannot be expected in the compositions with a $t$ far away from 1.00.

## 2.4 Ferroelectric Properties of Tungsten Bronze Morphotropic Phase Boundary (MPB) Systems

On a binary phase diagram, a MPB appears as a nearly vertical line separating two distinct ferroelectric phases. This phase boundary generally occurs at a nearly constant composition over a wide temperature range up to the ferroelectric phase transition temperature, Tc; an example is for the bronze MPB system, $Pb_{(l-x)}Ba_xNb_2O_6$ (PBN), which possesses both orthorhombic and tetragonal structures near x = 0.37 [14, 85-87]. Poled ceramics or single crystals of such MPB ferroelectrics can show an enhancement of numerous physical properties because of the proximity in free energy of an alternate ferroelectric structure.

Crystal compositions in other ferroelectric families can also possess MPB regions, with perhaps the best known of these being perovskite PZT and PLZT. 'However, compositions in the tungsten bronze family have a number of potential advantages over the perovskites, particularly for optical device applications.

## 2.5 The Lead Barium Niobate (PBN) System

The lead barium niobate (PBN) solid solution is arguably the most studied and developed MPB system in the tungsten bronze family. In addition to sintered ceramics, PBN has also been developed in the form of hot-pressed, grain-oriented ceramics [88-90] and as bulk single crystals using the Czochralski growth methods [52, 90]. The latter have been especially useful for determining the directionally dependent ferroelectric properties in this system, revealing the unusual behavior which can occur for compositions near the morphotropic boundary. For example, near morphotropic tetragonal $Pb_{0.6}Ba_{0.4}Nb_2O_6$ (PBN:60) has single crystal dielectric constants of $\varepsilon_{11} = 1900$ along the a axis and $\varepsilon_{33} = 500$ along the c axis [91]. Spontaneous polarization in poled crystals is also large, in the range of $70\mu C/cm^2$ at room temperature based on recent measurements. The large spontaneous polarization and large dielectric constants available in morphotropic PBN are especially significant for optical applications.

## 2.6 The Strontium Barium Niobate (SBN) System

In $Sr_xBa_{(1-x)}Nb_2O_6$ (SBN) ceramic, the A site was partially filled with $Sr^{2+}$ and $Ba^{2+}$ cations in five of the six available positions (1/6 is vacant) while the C site is left empty. The electrical properties of SBN are strongly dependent on the Sr/Ba concentration ratio [5, 41, 42]. Moreover, the cation occupants affect the physical and chemical properties of SBN. SBN exhibits ferroelectric properties in the range of $0.25 \leq x \leq 0.75$. Modification of the SBN ceramic is viable in order to obtain the properties required for electro-optic devices or pyroelectric IR detector applications. However, modification of the Sr/ Ba ratio involves a very precise control of microstructure and composition, especially in the addition of dopants. It was reported that the modified material exhibited twice the pyroelectric coefficient and four times the dielectric constant compared to that of unmodified SBN [92]. Addition of a small amount of rare earth elements may result in the reduction of the Curie temperature, Tc, (temperature at which the material undergoes phase changes from ferroelectric to paraelectric phase) and enhancement of the pyroelectric coefficient to twice the value of the undoped SBN [93]. Doping also improves the dielectric properties of the material at room temperature and produces a more stable material [94]. Doping SBN with rare earth ions is far more effective technique to modify the physical properties of SBN compared to varying the Sr/Ba ratios. Previously, it has been shown that the $Sr_{(0.53)}Ba_{(0.47)}Nb_2O_6$ (SBN:53) ceramic exhibited optimal electrical properties in terms of dielectric constant, remnant polarization and pyroelectric coefficient, compared to the rest of the Sr/Ba composition [39].

## 2.7 The Role of Oxygen (O) Vacancies.

Additional work is required to understand the role of cation vacancies in TTB-structured ceramics but the influence of O-vacancies (VO ) on the incommensurate/commensurate modulation is comparatively clear. The dielectric constant and loss vs temperature data for $Ba_4RE_2Ti_5Nb_5O_{29}\Box$ (RE = La, Nd) in comparison with $Ba_4Nd_2Ti_4Nb_6O_{30}$ indicates that; the deficit of B site positive charge in $Ba_4RE_2Ti_5Nb_5O_{29}\Box$ is compensated by oxygen vacancies (VO ). For$Ba_4RE_2Ti_5Nb_5O_{29}\Box$, relaxor behavior is anticipated based on the ionic radius of La, as before and consistent with $Ba_4La_2Ti_4Nb_6O_{30}$. However, $Ba_4Nd_2Ti_5Nb_5O_{29}\Box$ is a relaxor rather than a normal ferroelectric and differs primarily with $Ba_4Nd_2Ti_4Nb_6O_{30}$ in that the former composition has all positions filled within the oxygen sublattice. To explain the difference in behavior, it is important to view the incommensurate to commensurate transition as essentially a change in tilt configuration of the oxygen sublattice; it is strongly influenced by oxygen stoichiometry.

## 2.8 The Role of A1-Site Vacancies

Figure 2.2 shows the relative permittivity versus temperature plots for $Ba_4RE_{(0.67)}\Box_{(1.33)}Nb_{10}O_{30}$ (RE = La, Nd, Sm, Gd, Y) ceramics, originally described by Gardner and Morrison [83] which illustrate that compositions with RE ion size $\leq 1.27\mathring{A}$ (Nd) show ferroelectric behavior consistent with the observations of Levin et al [31] and Stennett et al.[30] where as those with La (1.32 Å) exhibit a relaxation at low temperature.

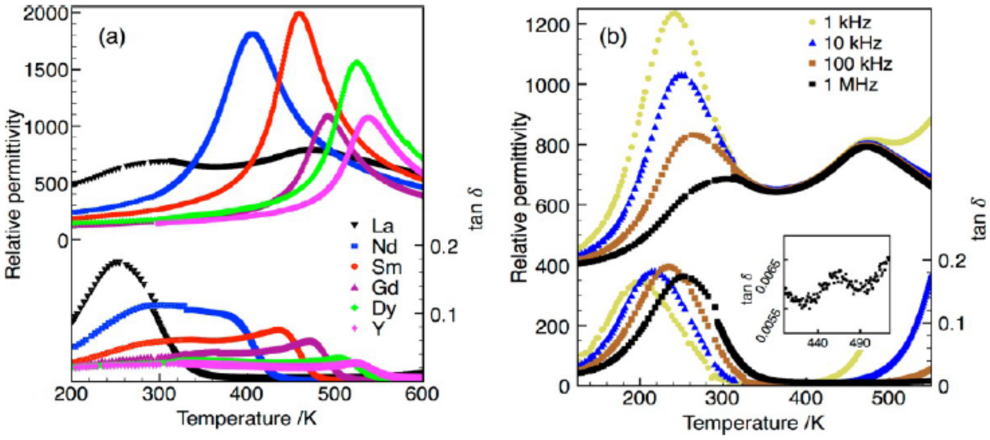

Figure 2.2: Relative permittivity and loss $(tan\delta)$ at 1 MHz versus temperature plot for (a) $Ba_4RE_{(0.67)}\square_{(1.33)}Nb_{10}O_{30}$, RE = La, Nd, Sm, Gd, Dy, Y) ceramics, and (b) frequency dependent data for $Ba_4La_{0.67}\square_{(1.33)}Nb_{10}O_{30}$, according to Gardner and Morrison [83].

## 2.9 The Role of Dopants/Substitutes

Doped tungsten bronze ferroelectric crystals show outstanding potential for photorefractive applications. To date, it has been achieved an improvement of two orders of magnitude in speed while maintaining high coupling in the desired spectral range. Using these improved bronze crystals, several new device concepts based on phase conjugation, image processing and laser beam manipulation are being explored in various laboratories in the U.S.

## 2.10 Calcium magnesium silicate (CMS) phosphor:

Calcium magnesium silicate (CMS) phosphor, with chemical formula $Ca_2MgSi_2O_7$, has recently drawn too much interest due to its unique structure features with an extraordinary physical and chemical stability. It has been also extensively discussed in biological and medical areas of application [44]. Silicate with akermanite structure is becoming a possible and attractive bio-ceramics for tissue engineering applications [45, 95]. For instance akermanite calcium magnesium silicate has an extraordinary biocompatibity and excellent bioactivity properties. By now it is becoming a promising bio-ceramic bone tissue engineering materials in medical applications or a probable bone material [48, 96].

## 2.11 Synthesis

Generally bulk materials are considered into two categories i.e. single crystal and ceramics. Single crystal: is solid in which entire sample in form of crystal lattice and uninterrupted at the edges without grain boundaries. These single crystals are fabricated by hydrothermal synthesis, sublimation or Czochralski process depending on physical characteristics of the crystal [97]. Polycrystalline (ceramic): materials are generally synthesized by double step processing method by using oxides and carbonates as starting material. In these process two steps is involved (1) Calcination (2) Sintering. In calcination process sample formed with desired phase composition and phase formation in sintering process includes dense microstructure having high enactment of electrical properties.

**Solid state synthesis**, as the name implies, uses solid state materials such as metal oxide powders. The synthesis is governed by diffusion of ions across grain boundaries in order to synthesize the desired product. This requires grinding of the reagents in a ball mill over long periods of time $(> 24hrs)$ [98] and use of a high temperature sintering step in order to increase diffusion of ions. However, repeated grinding and firing is sometimes required before the product is obtained at high purity [98]. Fine grain powders of reactive reagents are desirable in order to increase the surface area. Occasionally, organic solvents are used in the reaction to create slurry [98, 99]; this can help decompose a certain species, or aid diffusion of ions. The resulting slurry (if organic solvents are used) is then dried in a vacuum oven and then the powder is pressed into a pellet. Pelletizing the powder is done to have the grain boundaries as close as physically possible [100] before heating or applying high pressure while heating. Pelletizing will aid in diffusion of ions as well. Depending on the temperature needed for the synthesis and the reagents used, different heating vessels can be used. Typically, a material with a high melting temperature and low reactivity is used such as $Pt, Al_2O_3, ZrO_2, or Y_2O_3$ [101]. This will ensure that you do not get any reaction with the boat as high temperatures can increase reactivity. The atmosphere in which the heating takes place is crucial as well. Some synthesis require no special atmosphere and can take place in an unspecialized furnace; however, some require an $H_2/Ar$ atmosphere to prevent oxidation of certain species and require a tube furnace. Because of the use of such high temperatures, the product that is formed is the most thermodynamically stable product. This can be a hinderance depending on what the desired product is.

**Sol-gel Symthesis Methods**: The sol-gel process may be described as: ”Formation of an oxide network through polycondensation reactions of a molecular precursor in a liquid.” A sol is a stable dispersion of colloidal particles or polymers in a solvent. The particles may be amorphous or crystalline. An aerosol is particles in a gas phase, while a sol is particles in a liquid, A gel consists of a three dimensional continuous network, which encloses a liquid phase, In a colloidal gel, the network is built from agglomeration of colloidal particles. In a polymer gel the particles have a polymeric sub-structure made by aggregates of sub-colloidal particles. Generally, the sol particles may interact by van der Waals forces or hydrogen bonds.

A gel may also be formed from linking polymer chains. In most gel systems used for materials synthesis, the interactions are of a covalent nature and the gel process is irreversible. The gelation process may be reversible if other interactions are involved.

**1. Synthesis and Characterization Flow chart:(Solid State Reaction)**

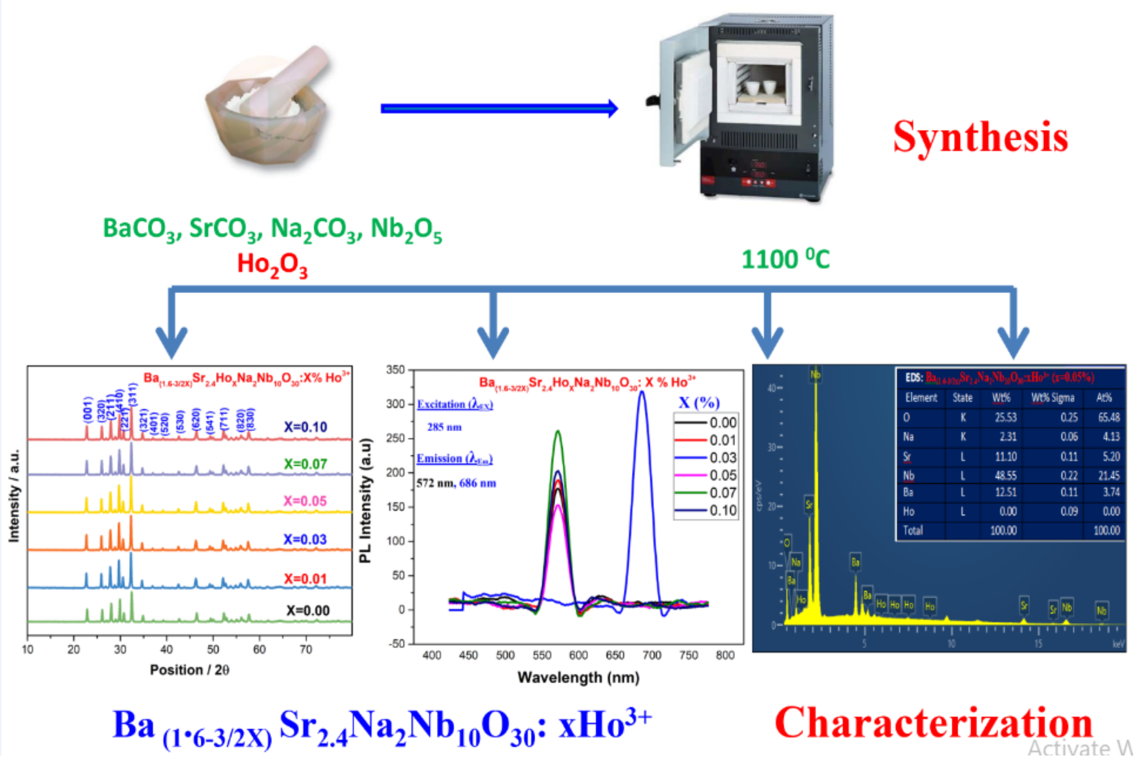

EDS: $Ba_{(1.6-3/2x)}Sr_{2.4}Na_2Nb_{10}O_{30}$:$xHo^{3+}$ (x=0.05%)

| Element | State | Wt% | Wt% Sigma | At% |
|---|---|---|---|---|
| O | K | 25.53 | 0.25 | 65.48 |
| Na | K | 2.31 | 0.06 | 4.13 |
| Sr | L | 11.10 | 0.11 | 5.20 |
| Nb | L | 48.55 | 0.22 | 21.45 |
| Ba | L | 12.51 | 0.11 | 3.74 |
| Ho | L | 0.00 | 0.09 | 0.00 |
| Total |  | 100.00 |  | 100.00 |

Figure 2.3: Synthesis and Characterization Flow chart:(Solid State Reaction

## 2. Synthesis and Characterization Flow chart:(Sol-gel Process)

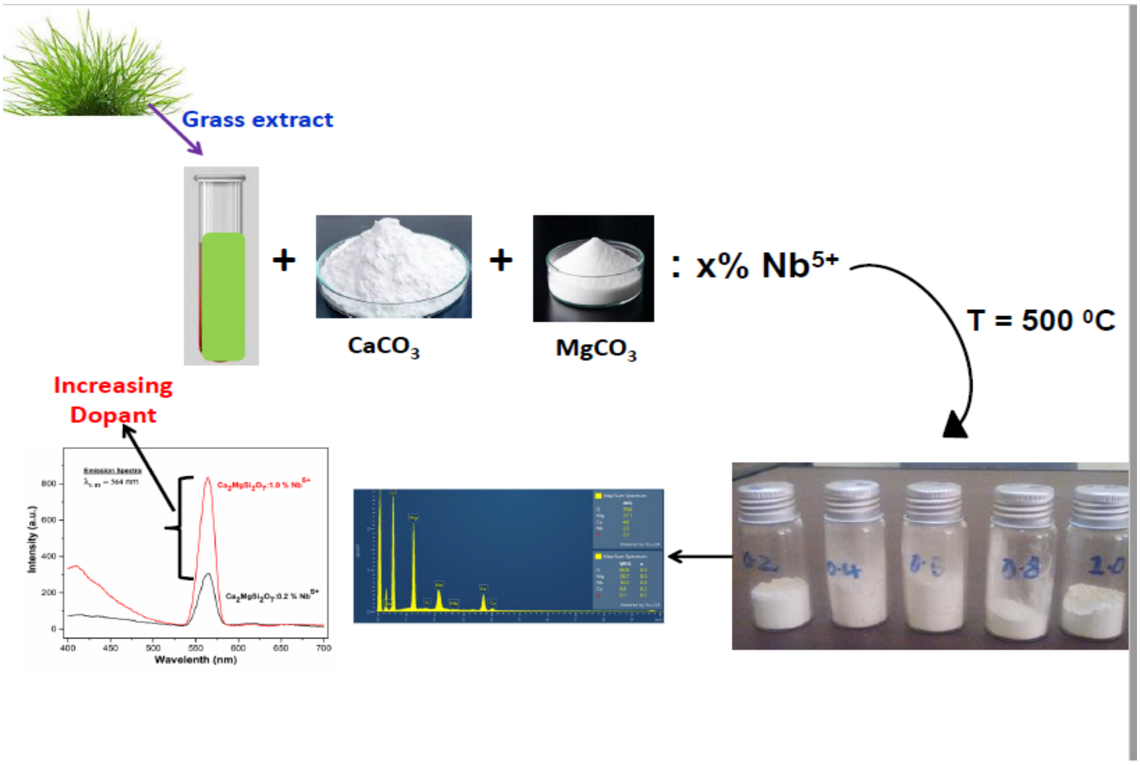

Figure 2.4: Synthesis and Characterization Flow chart:(Sol-gel Process

**X-Ray diffraction (XRD)**

X-Ray diffraction is an incredibly useful technique for determining the crystalline structure of a material. Provided you have a powder sample, sample preparation is very simple as well. X-Ray light, typically from a $Cuk_\alpha$ source of $\lambda = 1.5405\mathring{A}$, is used to interact with the periodically spaced atoms within a crystalline lattice. The X-Rays are generated upon impact by electrons on a copper target. The use of X-Ray light is important as it has a small enough wavelength to interact and diffract off of the crystalline lattices which are on the same size scale. The X-Ray light interacts with an electron cloud of an atom, via the electromagnetic force. This interaction is more intense with higher electron density, which is why X-Ray images only show the bone density and not the flesh of a human because Calcium has many more electrons than Carbon and Hydrogen. X-Rays interact with atoms with a higher atomic number, Z, than they do with those of lower atomic number: this means that refinement of parameters relating to atoms of low atomic number-such

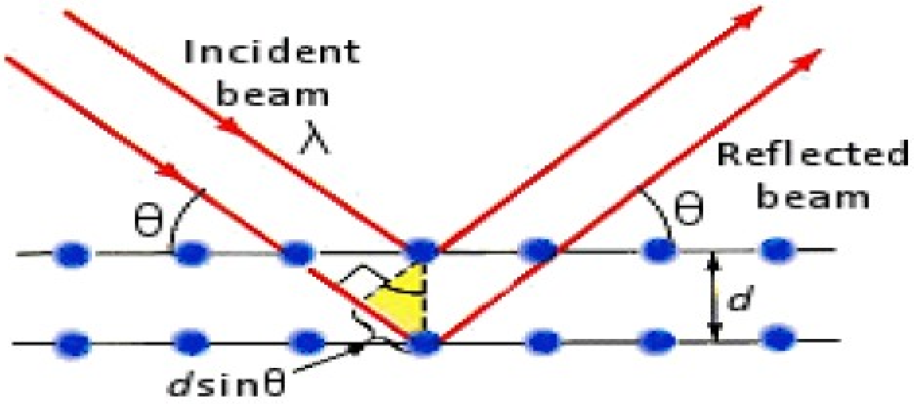

Figure 2.5: Bragg diffraction from two parallel planes [103].

as $O^{2-}$ is necessary.

It is well-known that X-ray is one kind of electromagnetic radiation with a wavelength of $1\mathring{A}$, which is in the region between gamma-rays and ultraviolet. X-ray diffraction is one of the most popular non-destructive experimental techniques for probing the crystalline structure at the atomic level.

A crystal lattice is a regular three-dimensional distribution of atoms in space. These are arranged to form a series of parallel planes separated by a distance d, which varies according to the structural and physical information of the material. Figure 2.4 illustrates the schematic diagram of Bragg diffraction from two parallel planes. When a monochromatic X-ray with the wavelength of $\lambda$ interacts with a crystal sample at an angle, $\theta$ the diffraction from parallel planes of atoms occurs according to Bragg's law [92] [102].

Ideally, the sample analyzed with XRD should contain a large number of small crystals which are randomly oriented. The X-rays are therefore diffracted from different (hkl)- planes simultaneously according to Bragg's law as shown below [104].

In this study, samples prepared by solid state reaction methods were characterized by powder X-ray diffraction using a Phillips XPERT-PRO diffractometer (Figure 2.5) fitted with $CuK_{\alpha}$ radiation between $2\theta$ = $10^{0}$ and $80^{0}$. For the cubic structure, the unit cell lattice parameters (a) were calculated by the least square fitting method from the d-spacing and the Miller indices, hkl values using [104]. Moreover, the crystallite size (L) of all samples were estimated using the conventional Scherer equation described below [105],

$$L = \frac{0.9\lambda}{\beta \cos\theta} \tag{2.4}$$

Where $\lambda$ is the x-ray wavelength, $\beta$ is the area value of the full width at half maxima (FWHM) of the peak, and $\theta$ is the angle corresponding to the peak [103].
The XRD patterns include peak position and intensity of the diffracted beam, which provides a variety of information about the films. Angles are used to calculate the interplanar atomic spacing. Until now, over 80,000 materials have been enrolled in the International Powder Diffraction File (PDF) database as the Joint Committee for Powder Diffraction Standards (JCPDS) [106, 107]. Once the XRD patterns are provided and compared with the standard data, the results of the crystal, phase composition, grain size, and lattice strain can be easily calculated. All in all, X-ray diffraction is a powerful tool and indispensable to materials science. The raw powders should weigh in stoichiometric amounts and mixed in an agate mortar for 30 minutes. This powder may calcine in air at $1300^0C$ for 6 hours. The obtained powder could ground and mixed with polyvinyl alcohol (PVA) as a binder. Then, cylindrical pellet could be obtained by pressing at 20 kN (12 mm diameter, 2 mm thickness). For Example the identification of the crystalline structure of the $Ba_5CaTi_{(1.94)}Zn_{(0.06)}Nb_8O_{30}$ powder was performed by X-ray diffraction (XRD) using a $\theta/2\theta$ diffractometer fitted with a fast detector (Bruker $D8$, $CuK_{\alpha 1}$, Link eye detector) at room temperature $(293K, 0.0150$ step, $10 - 120^0$ $2\theta$ range, scanning speed of $1^0$ $min^{-1})$. The lattice parameters, atomic positions, occupation rate, and thermal agitation factor were refined by the rietveld method using the Jana 2006 software [108].

So barium strontium sodium niobates ferroelectrics tungsten bronze structured powders were characterized by X-ray powder diffraction (XRD). By XRD analysis, we can also determine; lattice parameters of ceramics.

**Scanning Electron Microscope (SEM)**

The scanning electron microscope (SEM) is a type of electron microscope that

Figure 2.6: Phillips XPERT-PRO diffractometer.

capable of producing high resolution image of sample surface. When the electron beam is focused on the sample surface, the surface is scanned which leads to certain phenomena. When beam of electrons strikes the surface of the sample and interacts with the atom of the sample, signals in the form of secondary electrons, back scattered electrons and characteristic X-rays are generated that contains information about the samples surface topography, composition, etc [105]. Electron backs scattering penetrate to the sample and interact with neighbor atom. This cause secondary electron emission from the atom in the sample and X-ray irradiation [109, 110], penetration depth of the electron beam depends on the acceleration voltage of incoming electron and the surface sensitivity of the method. In addition to the above secondary electron emission, some of the electron can remain in the sample while other electrons are released to the field and they can be caught by detector and image on screen. The electrons with the atoms that make up the sample producing signals that contain information about the samples surface topography. The degree of topographical information depends on location of the detector relative to the surface of the sample. SEM was used to examine the surface morphology of the samples. In general, electrons generated in an emitter impacts are accelerated by

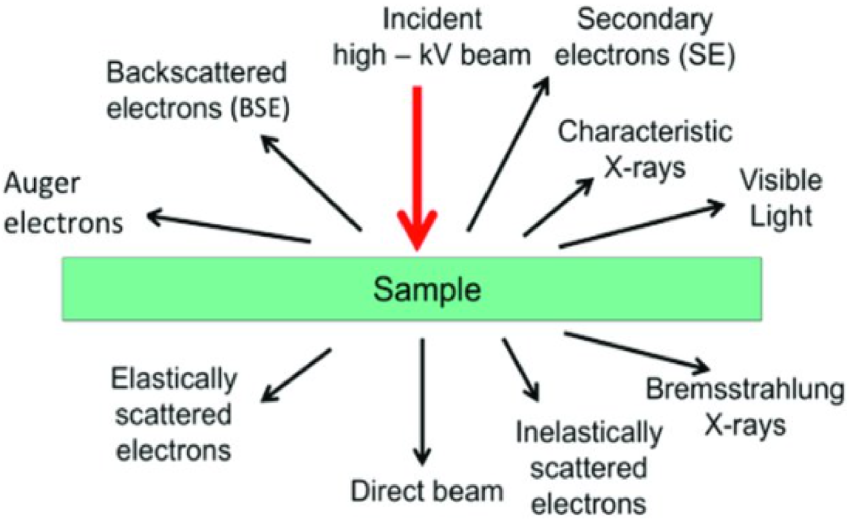

Figure 2.7: The electron interaction with the sample [111].

electromagnetic field and impact the sample emitting various types of electrons depending on the penetration depth (R), which can be expressed by equation:

$$R = \frac{27.6A(E_0)^{1.67}}{\rho z^{0.889}} \tag{2.5}$$

where, $A$ is mass number $(gmole^{-1})$, $E_0$ is energy of accelerated electrons that impacts the sample $(keV)$, $\rho$ is density of the material $(gcm^{-3})$, and $Z$ is atomic number. EDX was used to provide information of elemental composition, atomic distribution (mapping), and semi-quantitative analysis. In EDS energy dispersion spectra these lines correspond to the peak energy positions usually within the range of 1 keV to 20 keV. Area under the peak can give information about amount of the element in a sample.

The SEM can produce very high-resolution images of a sample in its primary detection mode, which is secondary electron imaging. Characteristic X-rays are emitted as the electron beam removes an inner shell electron from the sample, causing a higher energy electron to fill the shell and release energy. These X-rays can be used

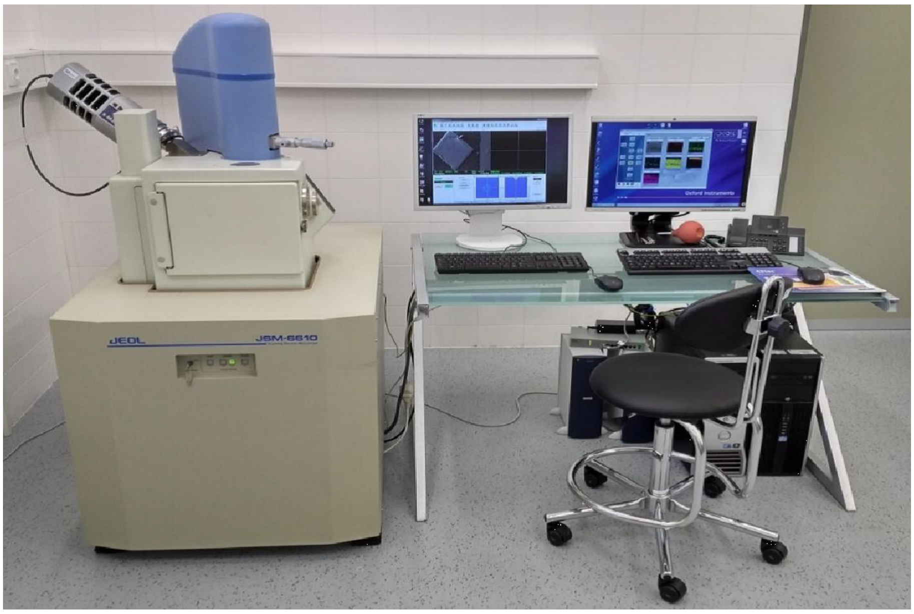

Figure 2.8: JEOL JSM-6610 Scanning electron microscope.

to identify and quantitatively determinate the elements in samples by a technique known as energy dispersive X-ray spectroscopy. Back scattering electrons are produced by elastic interactions of beam electrons with nuclei of atoms in the specimen [105, 112]. Since heavy atoms with a high atomic number are stronger scatterers than light ones, images with back scattering electrons contain compositional information thus the distribution of different elements in the sample can be get from back scattering electrons images. SEM characterization method has some advantage as easy and fast preparation as well as operation of the instrument. The main disadvantage of this method is the sample should be conducting, the resolution is limited to the micro range and the analysis of the sample can be provided only for the surface of material not for the bulk. In the present study, SEM techniques employed using JSM-6610 instrument, the measurement performed to identify the morphology of all samples in the form of powder. Before taking measurements, both samples are coated with platinum in Magnetron Sputter Coater.

**Fourier Transform Infrared Spectroscopy (FTIR)**

The Fourier-transform infrared (FTIR) spectroscopy spectrum has been widely used for the identification of organic and inorganic compounds. (FTIR) is also an essential characterization technique to identify the compositional elements of the material and to analyze the chemical bonding and functional groups present in the material. Fourier transform infrared (FT-IR) spectroscopy is a simple and non-destructive powerful tool for the identification of types of chemical bonds in the compounds by producing infrared absorption spectra [113, 114]. It is also used for identification of the structure of samples as well as identification of unknown materials using the frequencies of the vibration modes. In FT-IR analysis, absorption of IR radiation occurs when a photon transfers to a molecule and excites it to a higher energy state. The excited states result in the vibrations of molecular bonds, i.e., stretching, bending, twisting, rocking, wagging, and out-of-plane deformation, occurring at varying wavenumbers (or frequencies) in the IR region of the light spectrum [115]. Energies of bond vibrations between atoms are recorded. Different vibration modes and bond types give rise to different energies. The wavenumber of each IR absorbance peak is determined by the intrinsic physical and chemical properties of the corresponding molecule in its particular functional group. In this work, FT-IR spectroscopy measurements are accomplished using transmittance method with potassium Bromide (KBr) as IR window in the wave number region of 400 - 4000 cm-1. A small amount of powder sample is mixed with KBr and ground in a mortar with a pestle for 5minutes. The mixture is then pressed in a standard hydraulic press to form a transparent pellet through which the beam of the spectrometer can pass. Before each measurement, the instrument Shimadzu IR Prestige-21 spectrometers arranged to run with a pellet of pure KBr only (no sample is added) kept in pellet holder to establish the background, which is then automatically subtracted from the sample spectrum. This technique is helped to eliminate the instrument influence during measurements.

### Transmission Electron Microscope (TEM)

Transmission electron microscopy (TEM) is used for more detailed characterizations with resolutions down to the atomic level, thus assisting in revealing the crystal structure, crystal orientation, and structural defects. TEM apparatus requires

Figure 2.9: Shimadzu IR Prestige-21 FT-IR spectrometer.

electron source, condenser system, specimen, and imaging system. In TEM, an electron beam is generated by the source and is focused toward the specimen using condenser lenses, aperture, and objective lenses, whereas projective lenses are used to guide the transmitted beam through a thin sample slice onto a fluorescent screen (Figure 2.9).

The acceleration voltages of electrons should be in the order of a few hundred kV, and the sample thickness should be $< 100$ nm to ensure that the electron beam can be transmitted through the specimen. Therefore, sample preparation for TEM measurements is a critical task that is carried out by focused ion beam (FIB) in SEM. TEM resolution can be improved down to the atomic level when functioning in the high-resolution mode (HRTEM). In this mode, image contrast is created through the interference between the transmitted and diffracted electron waves. Therefore, the HRTEM image can be considered as an interference pattern of diffracted and incident electron waves in the image plane, providing information on local variations in the crystal structure, lattice defects such as stacking faults and dislocations, and growth directions [116]. One of the advantages of SEM and TEM is that these imaging techniques produce a wide range of signals from specimens, as shown in

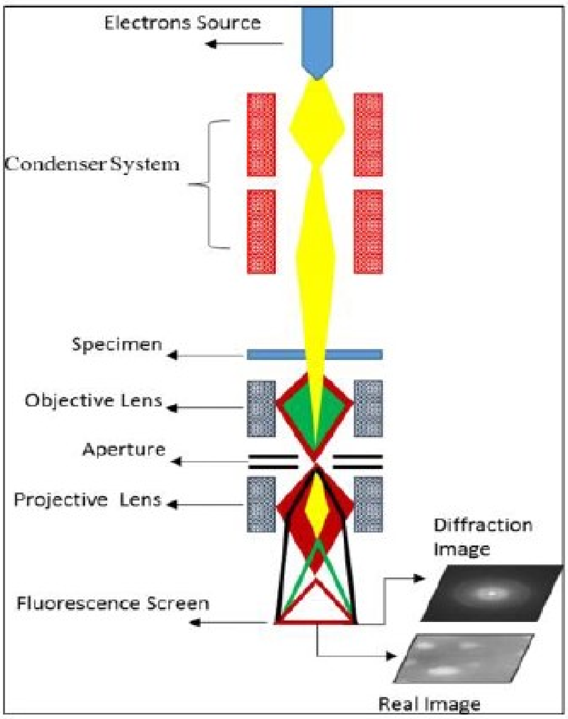

Figure 2.10: Schematic of the TEM setup.

Figure 2.10. Some of these signals, such as characteristic X-rays, are used to provide chemical information and details about specimen composition. The characteristic X-rays or Auger electrons are generated when the incident electrons transfer some of their energy to an atom in the specimen and one of its electrons is ejected leaving a hole in the inner shell. This hole is recombined by an electron from an outer shell, whereby the atom returns to the ground state. The energy produced as a result of this process can be released as a characteristic X-ray (Figure 2.10), or can be transferred to an electron in an outer shell, which is subsequently ejected as an Auger electron. Chemical compositions of a specimen can be determined using these characteristic X-rays. This characterization technique is called energy dispersed X-ray spectroscopy (EDS).

In addition, electron energy losses during inner and outer shell transitions are useful for detecting the elemental compositions of the specimen. Therefore, electron energy loss spectroscopy (EELS) is used as a complementary technique to EDS for

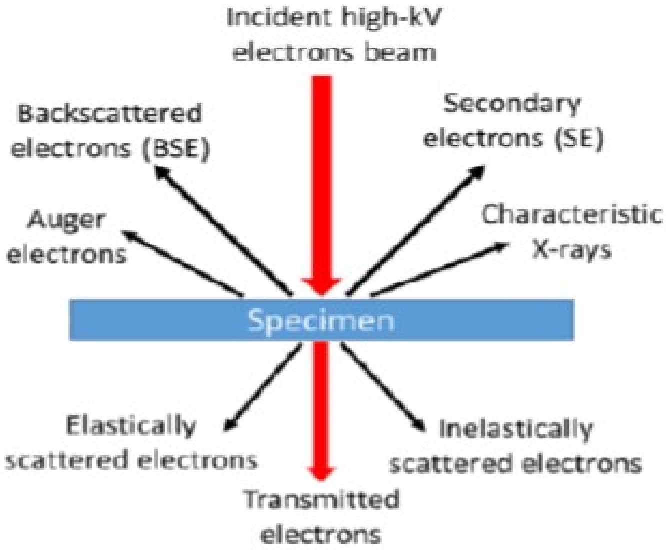

Figure 2.11: The interaction mechanisms of an electron beam with a specimen [116].

identifying chemical compositions [116].

**Thermogravimetric analysis (TGA)**:

Thermogravimetric analysis is one of the members of the family of thermal analysis techniques used to characterize a wide variety of materials. TGA is a technique used for measuring changes in the mass of a sample as a function of temperature or time that occur in response to programmed temperature changes [104] estimation of product lifetimes. The changes in the mass can be caused by a variety processes such as decomposition, sublimation, vaporization, adsorption, desorption, oxidation, and reduction. The resulting curve is called thermogram. The thermogram provides information about the thermal stability and composition of the original sample, the composition astability of intermediates and the waste composition. Each material has its corresponding thermo-gram allowing identification [104].

TGA characterization was performed in order to identify the change in the sample weight loss as a function of temperature. The thermal analysis of samples can be performed using DTG-60H instrument Figure 2.12 below by heating them from room temperature to designed value with a heating and cooling rate of $15^0C$ per

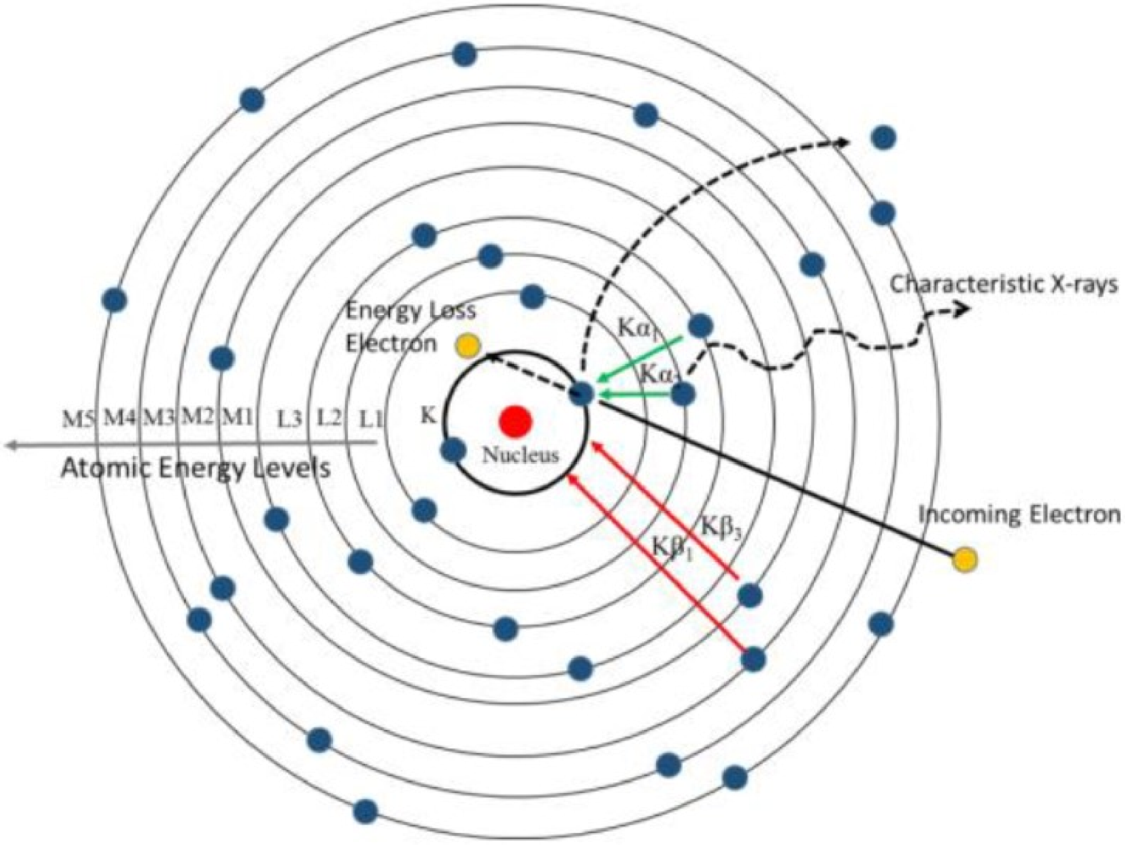

Figure 2.12: Characteristic X rays.

Figure 2.13: DTG-60H, TG/DTA Simultaneous Measuring Instrument.

minute in air or oxygen/Hydrogen/Argon atmosphere depending up on nature of samples interactions.

**UV-Vis Spectroscopy**

In order to investigate optical absorption properties of the samples within the range of 350 - 700 nm, the Shimadzu UV-3600 spectrometer equipped with an integration sphere will be used. Optical transmission spectra measurements of samples were performed using an Ultraviolet-Visible-Infrared (UV-Vis-IR) spectrophotometer (U-4100, Hitachi Corp.). It is possible to construct a non-destructive system that satisfies various analyses. The measurement region permits measurement from 175 up to 2600 nm. The spectrophotometer is useful to characterize the absorption, transmission, and reflectivity of all kinds of technologically important materials. The application, such as pigments, coatings, windows, and filters, usually requires recording at least a portion of the optical spectrum for evaluation of the optical or electronic properties of materials. Transmission spectroscopy is mainly interrelated to absorption spectroscopy. Here, light passes through the sample such as solid, liquid, and gas sampling and compared to the light that has not. The output result depends on the path length or sample thickness, the absorption coefficient of the

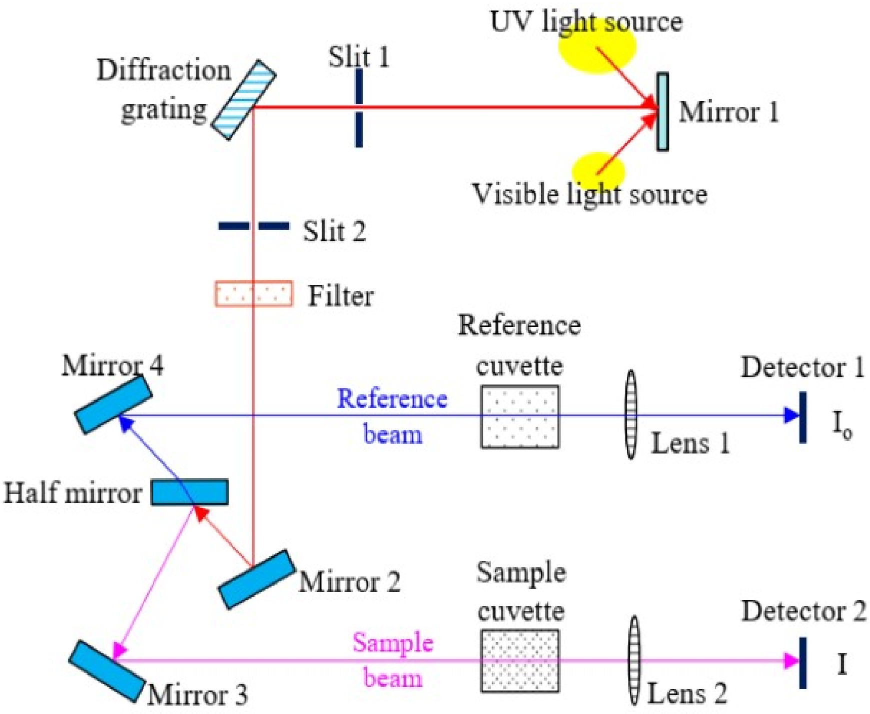

Figure 2.14: Optical system of U-4100 UV-Vis-IR spectrophotometer.

sample, the reflectivity of the sample, the angle of incidence, the polarization of the incident radiation, and, for particulate s matter, on particle size and orientation.
Figure 2.13 shows the optical system of the U-4100 UV-Vis-IR spectrophotometer [116].
An incident light beam from a tungsten lamp (UV, visible, and IR) and deuterium lamp (deep UV) is split into a monochromatic and then reaches a sample, part of the beam is reflected and part of the beam is transmitted through the medium which is measured by the photomultiplier and recorded by the computer, and the rest of the beam will be absorbed. Absorption of photons arises due to the transition of the electrons from the lower to the higher energy levels. The absorption coefficient decides the absorption ability of matter. The absorption coefficient $\alpha$ for a uniform medium can be defined in terms of the intensity change of a monochromatic light beam in the unit distance that the beam traveled in the medium.

**Photoluminescence (PL)**

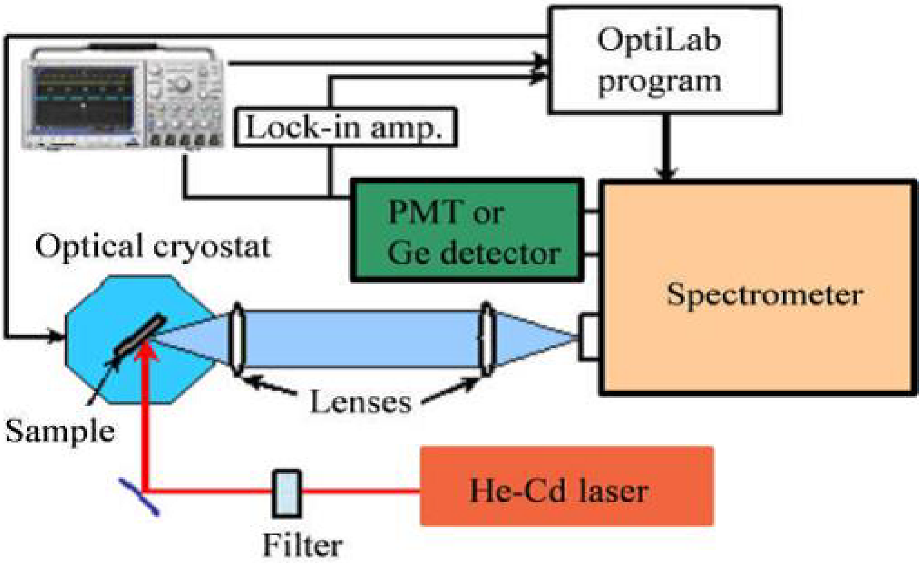

Figure 2.15: PL spectroscopy experimental set-up.

The different luminescent characteristics of as-deposited nanostructures after the annealing process were measured by photoluminescence (PL) measurement, which was performed with an iHR320 Micro-PL/Raman spectroscope (Horiba Ltd.). A He-Cd laser with a wavelength of 325 nm at a power of 20 mW can be used as an excitation light source. The basic scheme of PL spectroscopy experimental set-up is illustrated in Figure 14 [117].

Photoluminescence is an important technique for measuring the purity and crystalline quality of semiconductors. Several variations of photoluminescence exist, including photoluminescence excitation (PLE). Time-resolved photoluminescence (TRPL) is a method where the sample is excited with a light pulse and then the decay in photoluminescence concerning time is measured [118]. This technique is useful in measuring the minority carrier lifetime of semiconductors. A variety of material properties can be obtained by PL measurement, which will be listed as follows:

(1) Band-gap determination;

(2) Impurity levels and defect detection;

(3) Recombination mechanisms;

(4) Material optical quality.

The results of the PL spectrum covering the whole visible region varied from 300 to 1000 nm. The PL spectrum has exhibited a sharp peak of ultraviolet (UV) emission and a broad peak of deep-level emission (DLE), respectively. The UV emission is related to the crystalline quality, which corresponds to the exciton emission from the near conduction band to the valence band. However, the DLEs in the visible region are due to intrinsic defects in the crystal structure.

# 3

# Materials and Methods

This chapter is specific for the **experiment** of the work, which describes the **chemicals** that were used, **instrument** and the **procedures** for the synthesis and analysis of the work. Materials were synthesized by **solid state reactions** and **Sol-Gel** synthesis method.

## 3.1 List of chemicals

The raw materials (chemicals) that are used in the study are listed in the following table.

Table 3.1: Reactants expected to use in the synthesis of materials

| S.N | **Reactants** | **Supplier and Grade** | **Drying Temperature** | **Source** |
|---|---|---|---|---|
| 1 | $BaCO_3$ | NICE, $>$ 99.99% | $450^0C$ | $Ba^{2+}$ ion |
| 2 | $SrCO_3$ | NICE, $>$ 99.99% | $450^0C$ | $Sr^{2+}$ ion |
| 3 | $Na_2CO_3$ | NICE,$>$ 99.99% | $450^0C$ | $Na^{1+}$ ion |
| 4 | $Nb_2O_3$ | SIGMA-ALDRICH, $>$ 99.99% | $550^0C$ | $Nb^{5+}$ ion |
| 5 | $Ho_2O_3$ | SIGMA-ALDRICH, $>$ 99.99% | $550^0C$ | $Nb^{5+}$ ion |
| 6 | $CaCO_3$ | NICE, $>$ 99.99% | $450^0C$ | $Ca^{2+}$ ion |
| 7 | $MgCO_3$ | NICE, $>$ 99.99% | $450^0C$ | $Mg^{2+}$ ion |

### 3.1.1 Apparatus

- **Furnace**: - (Programable up to 1100 $^0C$ with the heating rate of $5^0C/min.$)

- **Crucibles**:- (Platinium coated crucibles withstand up to 2200 $^0C$)
- **A gray-black Agate mortar and pestle**:- (a 6-inch in diameter mortar)
- **Magnetic Stirrer** (For stirring the solution of CMS Phosphor)
- **Oven** (For drying the CMS during stirring)
- **Filter Paper**(For filtering of the grass extract solution)

### 3.1.2 Advanced Instruments

- **XRD**:- (Phillips XPERT-PRO Model): by making use of $CuK_\alpha$ radiation ($\lambda = 1.5406\mathring{A}$) at 40.0 KV, 30 mA) over ($2\theta$ = 10 to $80^0$) range
- **SEM/EDS**:-((OXFORD INSTRUMENTS;( The Business of Science) model SS230862, ZEISS)
- **UV-Vis. Spectroscopy**:- (the powder in solution form using de-ionized water solvent)
- **FTIR**:- (Shimadzu IR Prestige-21 FTIR Spectrometer)
- **PL**:- (Cary Eclipse serial number My1849002 model fluorescence spectrophotometer)

## 3.2 Synthesis

All of the materials were prepared by conventional high temperature solid-state reaction synthesis methods using carbonates and oxide powders listed in Table 3.1 as precursors. Standard Solid state reactions from the normal stoichiometric mixtures of $BaCO_3$, $SrCO_3$, $Na_2CO_3$, $Ho_2O_3$, and $Nb_2O_5$ ($>$ 99.99%) purity from NICE and Sigma-Aldrich Campoanies were used.

**Stochiometric Equations**:

1. $[1.6-(3X/2)]BaCO_3 + 2.4SrCO_3 + Na_2CO_3 + (X/2)Ho_2O_3 + 5Nb_2O_5 = Ba_{[1.6-(3X/2)]}$

$Sr_{2.4}Ho_XNa_2Nb_{10}O_{30}$ + $[5-(3X/2)]CO_2$

2. $8CaCO_3 + 4MgCO_3 + 8SiO_2 * H_2O + 2Nb_2O_54Ca_{(2-x)}MgNbxSi_2O_7 + 12CO_2(\uparrow) + 8H_2O(\uparrow) + 5O_2(\uparrow)$

The solid state reaction occurs at high temperature $(1100^0C)$ and all $CO_2$ burned out. The desired product with normal stoichiometric equation obtained at the end of this process. The diffusion of ions also occurred during the grinding and solid state reaction process (equation 1). But the sol-Gel process occurred at $600^0$ with magnetic stirring and filtered with fiter paper (equation 2)

## 3.3 Characterization methods

The structure and phase formation of $Ba_{(1.6-3/2X)}Sr_{2.4}Ho_xNa_2Nb_{10}O_{30}$ nanocomposites were identified by using XRD Phillips XPERT-PRO Model: X-ray powder diffractometer using $CuK_\alpha$ radiation ($\lambda = 1.5406\mathring{A}$) at 40.0 KV, 30 mA) and the data were collected over the range ($2\theta$ = 10 to $80^0$). SEM/EDS results were obtained from (OXFORD INSTRUMENTS ;( The Business of Science) model SS230862, ZEISS. The images obtained from scanning electron microscopy (SEM) showed morphology and microstructure clearly with high quality images. The elemental composition and mapping of the powder samples were measured using energy dispersive x-ray spectroscopy (EDS). EDS spectroscopy was used as complementary and a standard procedures for determining and quantifying elemental composition of sample area as small as a few nanometers to micrometers. Chemical bonds present in $Ba_{(1.6-3/2X)}Sr_{2.4}Ho_xNa_2Nb_{10}O_{30}$ were identified by FTIR spectra analysis with the help of Shimadzu IR Prestige-21 FT-IR Spectrometer. We use FTIR transmittance spectroscopy for investigating the functional group (4000 to 400 $cm^{-1}$) of the $Ba_{(1.6-3/2X)}Sr_{2.4}Ho_xNa_2Nb_{10}O_{30}$ ferroelectric nanomaterial samples by direct use of as- prepared powder sample. Ultra Violet-Visible Spectroscopy (the powder in solution form using de-ionized water solvent) was used to measure the absorption. The solution of 100 ppm was centrifuge and used for UV-Vis spectroscopy analysis. Photoluminescence emission spectra of the samples (in solution form) were measured by Cary Eclipse serial number My1849002 model fluorescence spectrophotometer with slits of emission and excitation lights of 10 nm and 600 nm per minute scanning rates.

# 4

# Synthesis and Characterization of $(Ba_{(1.6-3/2X)}Sr_{2.4}Na_2Nb_{10}O_{30} : xHo^{3+})$ Ferroelectric nanomaterials by Solid state reaction routes for Device Applications

## 4.1 Introduction

The recent history of the world of condensed matter and material physics has shown that it is entering a new era. Extraordinary advances in instrumentation allow access to the world of atoms and molecules on an unprecedented scale. Powerful new experimental tools, from atomic probe microscopes to spectroscopies, are opening new windows for imaging and manipulating materials at the atomic scale. Applications range from the nanofabrication of electronic devices to exploring the mysteries of superconductivity. These changes are far-reaching. Many previously inaccessible research areas have yielded to new and unexpected advances in atomic-scale synthesis, characterization, imaging and visualization [119, 120]. In the last three decades, the production of nanostructured materials has attracted much attention due to their great diversity, excellent, interesting and unique properties and various possible applications [121-124]. Holmium oxide $(Ho_2O_3)$ is one of the most attractive rare earth oxides due to its special, excellent and unique optical and electrical properties, as well as several applications in wavelength calibration devices and pyrolysis catalysts, as well as improved optical properties for transition temperature control of ferroelectric nanomaterials when used as an additive [125-

126].

A ferroelectric material is a material that has a spontaneous polarization in the absence of an electric field that can be reversed by applying an electric field. Ferroelectric materials have unique dielectric, pyroelectric, piezoelectric and electro-optical properties [127]. These properties have several applications in capacitors, dielectric resonators, sensors, transducers, actuators, and ferroelectric nonvolatile memories, dielectric memories, optical waveguides, displays, microelectromechanical systems (MEMS), miniature mechanical and electromechanical elements [64-67, 128, 129]. Based on their special properties, ferroelectric materials have been used to produce active elements of various devices [68, 69].

The structure of Tetragonal Tungsten Bronze (TTB) consists of corner-sharing octahedra that are joined to form triangle, square and pentagonal areas. A structure is called a filled TTB if all square and pentagonal sites are filled; a classic example of this is $Ba_2NaNb_5O_{15}$ (BNN), where the octahedra are filled with Nb, the square sites with Na, and the pentagonal sites with Ba [70, 130, 131]. Ferroelectric tetragonal tungsten bronzes (TTB) are the second largest group of ferroelectric oxides after perovskites [5]. The crystal structure of TTB is similar to the perovskite structure in that it consists of corner-sharing $BO_6$ octahedra; however, the unit cell of the prototype TTB is approximately 10 times larger than the perovskite cell [127]. In a filled TTB, the triangular channels are empty, while the square and pentagonal channels are fully occupied, and the general formula can be written as$A2_4A1_2B_{10}O_{30}$.[132]

**TUNGSTEN BRONZE OXIDES** form the largest family of dielectrics next to perovskites. Tungsten-bronze compounds were considered as best candidates to replace lead-based compounds. It is not particularly surprising that crystals with a tungsten-bronze structure are ferroelectric. Filled tungsten bronze materials such as $K_3Li_2Nb_5O_{15}$ have attracted much attention in nonlinear optical applications,[15, 16] while unfilled tungsten bronzes have been well studied for their unique ferroelectric and piezoelectric properties [17, 18]. Recently, ceramics filled with tungsten bronze structure $M_4R_2Ti_4M'_6O_{30}$ and $M_5RTi_3M'_7O_{30}$ (M = Ba and Sr, R = Bi, La, Nd and Sm..., $M'$ = Ta and Nb) have attracted much scientific attention due to their interesting dielectric and ferroelectric properties [23-26]. At room temperature, the filled tungsten bronze tantanates are usually paraelectric, whereas the filled tungsten bronze niobates are all ferroelectrics. Some materials with tungsten bronze (TB) structure have been found more favourable for high dielectric constant [37], electro optic [38], pyroelectric [39], piezoelectric [40], nonlinear optic [5], acousto-optic [41], photo-refractive [42] etc. devices. Most of the TB structure belongs to tetragonal or orthorhombic structure with small distortion of multiple perovskites. Some tungsten bronze ferroelectric ceramics are found to be stable at room temperature with diffuse phase transition and relaxor behavior. Also, structural flexibility and chemical versatility of these materials make them more suitable for device applications.

The tetragonal tungsten bronze structure has been discussed by Magneli and Blomberg [133, 134] Wadsley [135], Francombe [86] and by Jamieson et al.[70]. The structural flexibility of tungsten bronze oxides offers more opportunities for exploiting new Pb-free ferroelectric materials. The tetragonal tungsten bronze structure is composed of ten distorted octahedral sharing corners in such a way that three different interstices (2 tetragonal A1, 4 pentagonal A2, and 4 triangle C) are available for cations in the general formula $(A1)_2(A2)_4(C)_4(B1)_2(B2)_8O_{30}$ [70].

One of the most effective ways in the synthesis of composite materials composed of ferroelectric material and ferromagnetic phases that allow a wide range of ferroelectric/piezoelectric and magnetic properties are that the material pairs with both good ferroelectric and good ferromagnetic properties [136-140]. Such a crystal structure with a large number of cationic and anionic sites allow synthesis of various compounds and doping, resulting in excellent control and great progress functional properties of the synthesized material [77, 141-143].

Again, the high toxicity of lead-based chemical compounds and the high pressure level of the process, which causes serious environmental problems, direct the attention of researchers to lead-free material. A promising way to solve this problem is to develop lead-free electro-ceramics to reduce lead contamination. Tungsten bronze compound is one of them. Recently, due to increasing demand, several studies have focused on the availability of high-quality lead-free materials [144, 145]

The nobility of our work is that we use a new design in addition to rare earth ions addition to set and control the transition temperature of our system close to operating or room temperature. As recently reported work showed by adding impurities such as La, Nd, Sm, Dy, and Y ions,[83] showed the possibility to control the transition temperature of ferroelectric materials. However, $Ho^{+3}$-doped nanomaterials had unique properties, for instance, ferroelectric measurements show that the ferroelectric Curie temperature $T_C$ increases with decreasing ionic radius (R) size, thus showing a direct relationship between $T_C$ and the tetragonality/ionic radius of R [146]. For smaller rare earth ions, the $T_C$ is above ambient and the noncentric space group P4bm is appropriate.

In the synthesis of rare earth ion $(Ho^{3+})$ additive tungsten bronze structured ferroelectric nanomaterials via conventional high temperature solid state reactions methods, we used carbonates and oxides as precursors. All raw materials were mixed by normal stoichiometric equation ratios. Digital electronic balance was used to measure the mass of each powder samples with the desired significant digits. Then the powder was grinded using Grey Black Agate Mortar and pestle, size 6 inch in diameter for 3 hr. before furnace. The grinded samples were placed in a high standard platinum crucible and subsequently fired at 1100 $^0C$ for 4 hour at the heating rate of 5 $^0C$ per minute. Finally this sufficient time of grinding results complete interactions and diffusion process which have an outcome of fine powder taken to furnace. To make it very confined and refined powder with miniaturized nanosize, we had also grinded the powder after furnace for additional 2 hrs. Then pure white powders obtained become ready for characterization.

In this thesis, we reported the synthesis and characterization of Holmium ion additive Barium Strontium Sodium Niobate via solid state reaction route. The structural analysis was studied using X-ray diffractometer (XRD). The surface morphology and microstructure was examined by SEM. The elemental composition identification and mapping have done by EDS. The absorption properties were analyzed by UV-Vis spectroscopy near UV. The different stretching modes were also analyzed using Fourier transform infrared spectroscopy (FTIR).

## 4.2 Experimental Techniques

### 4.2.1 Synthesis

Rare earth metal Holmium $(Ho3^{+)}$ ion doped Barium Strontium Sodium Niobate tungsten bronze structured ferroelectrics $(Ba_{(1.6-3/2X)}Sr_{2.4}Na_2Nb_{10}O_{30} : xHo^{3+})$ powder nanomaterials which was synthesized via high temperature solid state reaction route using calcium carbonate $(CaCO_3)$ 99.90%, Strontium carbonate $(SrCO_3)$ 99.99%, Sodium oxide $(Na_2O)$ 99.99%, Holmium Oxide $(Ho_2O_3)$ 99.99% and Niobium Oxide $(Nb_2O_5)$ 99.99% taking as a starting materials were successfully synthesized and characterized according to their stoichiometric ratio for various values of dopants concentration (x), (x= 0.00, 0.01, 0.03, 0.05, 0.07, 0.10, % $Ho^{3+}$). Then the powder was milled thoroughly for 3 hour using Grey Black Agate Mortar and pestle, size 6 inch in diameter. Then all the grinded samples were placed in a platinum crucible and subsequently fired at 1100 $^0C$ for 4 hour at the heating rate of 5 $^0C$ per minute. Finally, pure white powders were obtained after cooling down the programmable furnace.

**The chemical reaction process is given as follows:**

$$[1.6\text{-}(3X/2)]BaCO_3 + 2.4SrCO_3 + Na_2CO_3 + (X/2)Ho_2O_3 + 5Nb_2O_5 = Ba_{[1.6-(3X/2)]}Sr_{2.4}Ho_XNa_2Nb_{10}O_{30} + [5 - (3X/2)]CO_2 \tag{4.1}$$

The solid state reaction occurs at high temperature $(1100^0C)$ and all $CO_2$ burned out. The desired product with normal stoichiometric equation obtained at the end of this process. The diffusion of ions also occurred during the grinding and solid state reaction process.

### 4.2.2 Characterization

The structure and phase formation of $(Ba_{(1.6-3/2X)}Sr_{2.4}Na_2Nb_{10}O_{30} : xHo^{3+})$ nanocomposites were identified by using XRD Phillips XPERT-PRO Model: X-ray powder diffractometer using $CuK_\alpha$ radiation ($\lambda$=1.5406 Å) at 40.0 KV, 30 mA) and the data were collected over the range ($2\theta$ = 10 to $80^0$). SEM/EDS results were obtained from (OXFORD INSTRUMENTS ;( The Business of Science) model SS230862, ZEISS. The images obtained from scanning electron microscopy (SEM) showed morphology and microstructure clearly with high quality images. The elemental composition and mapping of the powder samples were measured using energy dispersive x-ray spectroscopy (EDS). EDS spectroscopy was used as complementary and a standard procedures for determining and quantifying elemental composition of sample area as small as a few nanometers to micrometers. Chemical bonds present in $(Ba_{(1.6-3/2X)}Sr_{2.4}Na_2Nb_{10}O_{30} : xHo^{3+})$ were identified by FTIR spectra analysis with the help of Shimadzu IR Prestige-21 FT-IR Spectrometer. We use FTIR transmittance spectroscopy for investigating the functional group (4000 to 400 $cm^{-1)}$ of the $(Ba_{(1.6-3/2X)}Sr_{2.4}Na_2Nb_{10}O_{30} : xHo^{3+})$ ferroelectric nanomaterial samples by direct use of as- prepared powder sample.

## 4.3 Results and discussion

### 4.3.1 XRD analysis

The XRD of $(Ba_{(1.6-3/2X)}Sr_{2.4}Na_2Nb_{10}O_{30} : xHo^{3+})$ nanomaterials were identified by using XRD Phillips XPERT-PRO Model: X-ray powder diffractometer using $CuK\alpha$ radiation ($\lambda$=1.5406 Å) at 40.0 KV, 30 mA) with Bragg's angle $(2\theta)$ range from $10^o$-$80^o$ with scanning rate of 0.033 $^oC$ per second as shown in figure 4.1. The smooth and sharp peaks can confirm the crystalline nature of the samples in the XRD pattern, and all the samples are pure tetragonal tungsten bronze structures ferroelec-

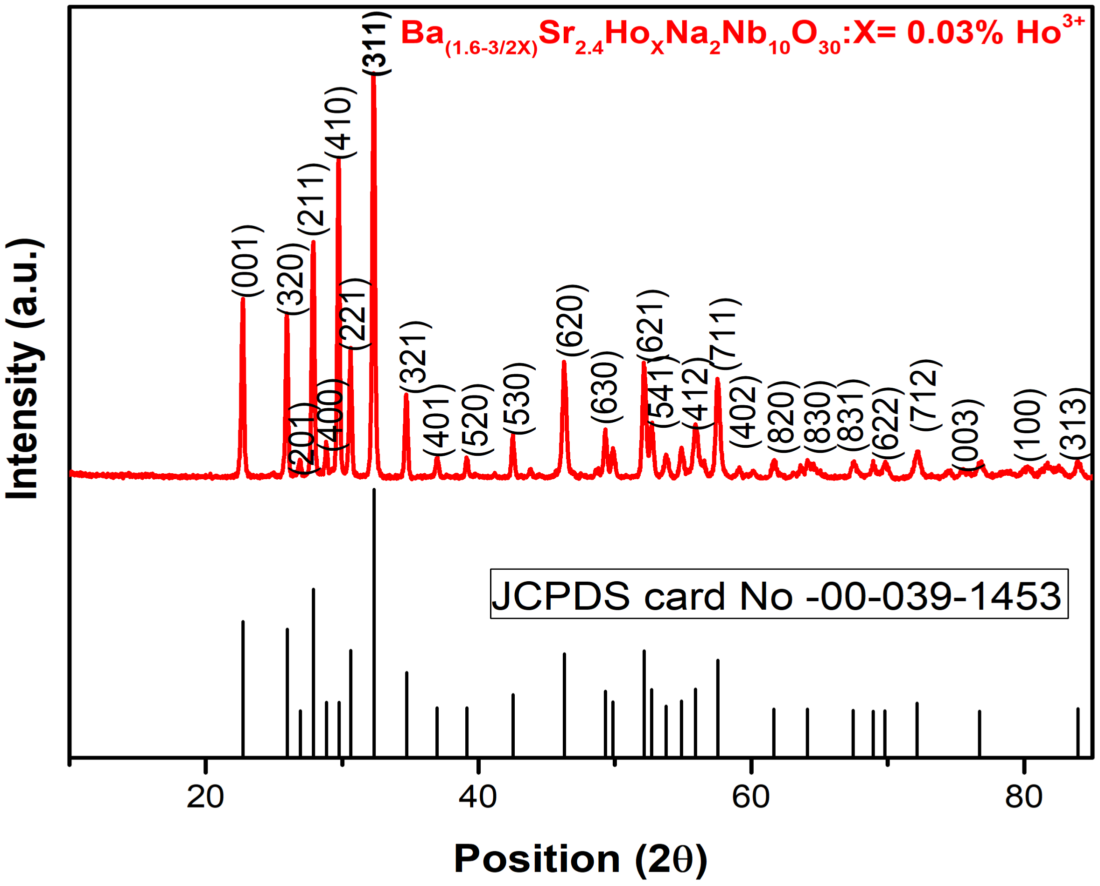

Figure 4.1: XRD pattern of Holmium ion doped Barium Strontium Sodium Niobate Tungsten Bronze Structured Ferroelectrics nanomaterials for (x= 0.03 % $Ho^{3+}$) with JCPDS card match.

tric nanomaterials.

The typical XRD patterns of $(Ba_{(1.6-3/2X)}Sr_{2.4}Na_2Nb_{10}O_{30} : xHo^{3+})$, tungsten bronze structured ferroelectric nanomaterial is shown in Figure 4.1 [147]. The respective plane's diffraction lines were compared with the standard JCPDS card number 00-039-1453 [148] for confirmation. Using the sharp peak (311) in Bragg's formula gives the values of inter-planar spacing [149, 150]. The value of the lattice parameters is calculated using [146, 151]. $a = d_{(hkl)}\sqrt{(h^2+k^2+l^2)}$. Where $d_{hkl}$ is the inter-planar spaciong of hkl planes and is calculated by Bragg's law, here the highest is obtained in (311). The calculated values of our TTBs structured crystal lattice parameters are, $a = b = 12.33\mathring{A}$ and $c = 3.93\mathring{A}$, having Group space of $P4bm$.

The significant effect of the dopants was also clearly observed from the XRD pattern. The experimental results showed the highest intensity (1845 a.u.) of the XRD pattern optimum value obtained for x=0.05 % $Ho^{3+}$ ion concentration without phase change (TTBs). The results were in good agreement with recent reports of rare earth ions doped system [133] . Smooth and sharp XRD pattern peaks were also obtained for all different amounts of dopants concentrations consistently without phase change. It was consistent for entire x=0.01-0.10 % $Ho^{3+}$ ions variation in concentrations. The prominent peak with maximum intensity (1845 a.u.) was found for x=0.05 % $Ho^{3+}$ ions concentration at angle ($2\theta$=32.3342$^o$) (as seen in Figure 4.1.). As Magneli and Blomberg [133] reported similar results that were obtained and checked with JCPDS standard card number for tetragonal tungsten bronze structure phase. The result obtained from our sample was also in good agreement with others recently reported works and standard card number (JCPDS 00-039-1453) that was confirmed from the XRD patterns match.

There is slight shift of peaks to lower angle from the benchmark (x=0.00) to dopants having concentrations of 0.01, 0.03 and 0.05 % $Ho^{3+}$. Then again it slightly shifts to higher angle for the increment of concentrations ranges of x= 0.07 to x=0.10. This is due to ionic radius difference of Holmium ion which substitute some amount of the Barium ion which have different ionic radius ($Ho^{3+}$: 1.02 and $Ba^{2+}$: 1.42 see Table 4.1) that in turn expected to improve the ferroelectrics property of the system since it depends on the ionic radii difference of A1 and A2 site atoms. In addition to distortion of ions, the difference between ionic radii has also a positive impact on the polarization process of the materials at nanolevel (See Figure 4.2. b and d and Table 4.1). The significant effect of the dopants was also clearly observed from the XRD pattern.

For prominent peak (311), using Debye-Scherer formula, the average crystallite size (D) of the $(Ba_{(1.6-3/2X)}Sr_{2.4}Na_2Nb_{10}O_{30} : xHo^{3+})$ ferroelectrics tungsten bronze structured crystal is calculated as (122.154) nm. Debye-Scherer formula is repre-

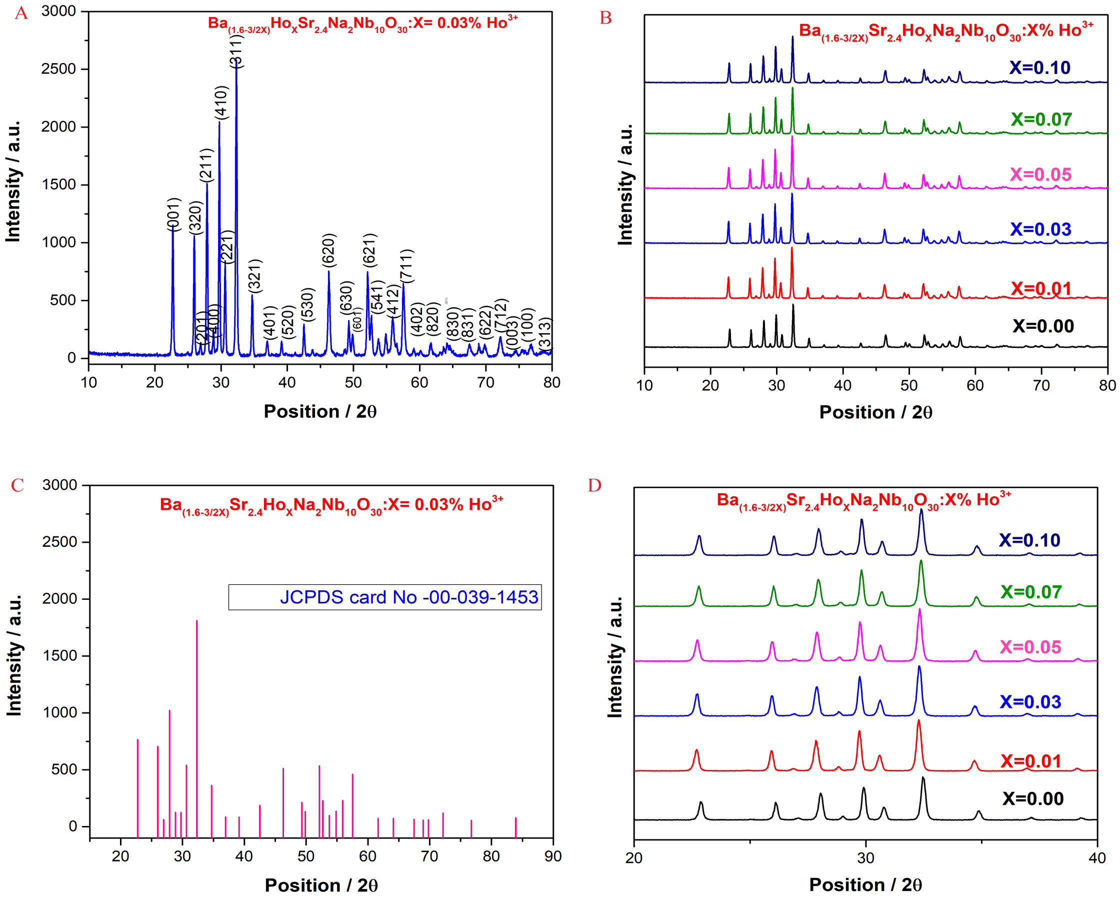

Figure 4.2: XRD pattern of Holmium ion doped Barium Strontium Sodium Niobate Tungsten Bronze Structured Ferroelectrics nanomaterials for a) x=0.03 % $Ho^{3+}$ XRD pattern with miller indices, b) XRD pattern of $(Ba_{(1.6-3/2X)}Sr_{2.4}Na_2Nb_{10}O_{30} : xHo^{3+})$ for x= 0.00- 0.10 %) c) XRD pattern with JCPDS card match, d) XRD pattern of $(Ba_{(1.6-3/2X)}Sr_{2.4}Na_2Nb_{10}O_{30} : xHo^{3+})$ zoomed (b).

sented as follows:

$$D = \frac{\kappa\lambda}{\beta cos\theta} \tag{4.2}$$

Table 4.1: Ionic Radius of elements: (CN=8, Alkali, Rare Earth and Transition) metals.( Source: Shannon Radii)

| | **Atomic Number** | **Name** | **Symbol** | **Ionic Radius Å** |
|---|---|---|---|---|
| | 56 | Barium, | Ba | $Ba^{2+}$: 1.42 |
| | 38 | Strontium, | Sr | $Sr^{2+}$: 1.26 |
| | 11 | Sodium, | Na | $Na^{1+}$: 1.26 |
| | 39 | Yttrium, | Y | $Y^{3+}$: 1.019 |
| | 67 | Holmium, | Ho | $Ho^{3+}$: 1.02 |
| | 57 | Lanthanum, | La | $La^{3+}$: 1.16 |
| | 60 | Neodymium, | Nd | $Nd^{3+}$: 1.109 |
| | 62 | Samarium, | Sm | $Sm^{3+}$: 1.079 |
| | 63 | Europium, | Eu | $Eu^{3+}$: 1.25 |
| | 66 | Dysprosium, | Dy | $Dy^{3+}$: 1.027 |
| | 41 | Niobium, | Nb | $Nb^{5+}$: 0.74 |

It has been shown that morphology and particle size have a great impact on the properties of nanostructured materials [152, 153]. The analysis of concentration of Holmium ion versus crystallite size showed that an increment of dopants concentration from 0.00 to 0.03% reduces the crystalline size of the system. However, the crystallite size increases for an increment of dopant concentration from 0.03 to 0.07% and remains constant for an increment of dopant concentration from 0.07 to 0.10%. The smallest crystallite size was obtained at Holmium ion concentration value of 0.03% and its value 60.13 nm. XRD pattern (Figure 4.2. c) of the powder calcined at a temperature of 1100 $^0C$ showed also the presence of tetragonal tungsten bronze structured $(Ba_{(1.6-3/2X)}Sr_{2.4}Na_2Nb_{10}O_{30} : xHo^{3+})$ ferroelectrics phase, that

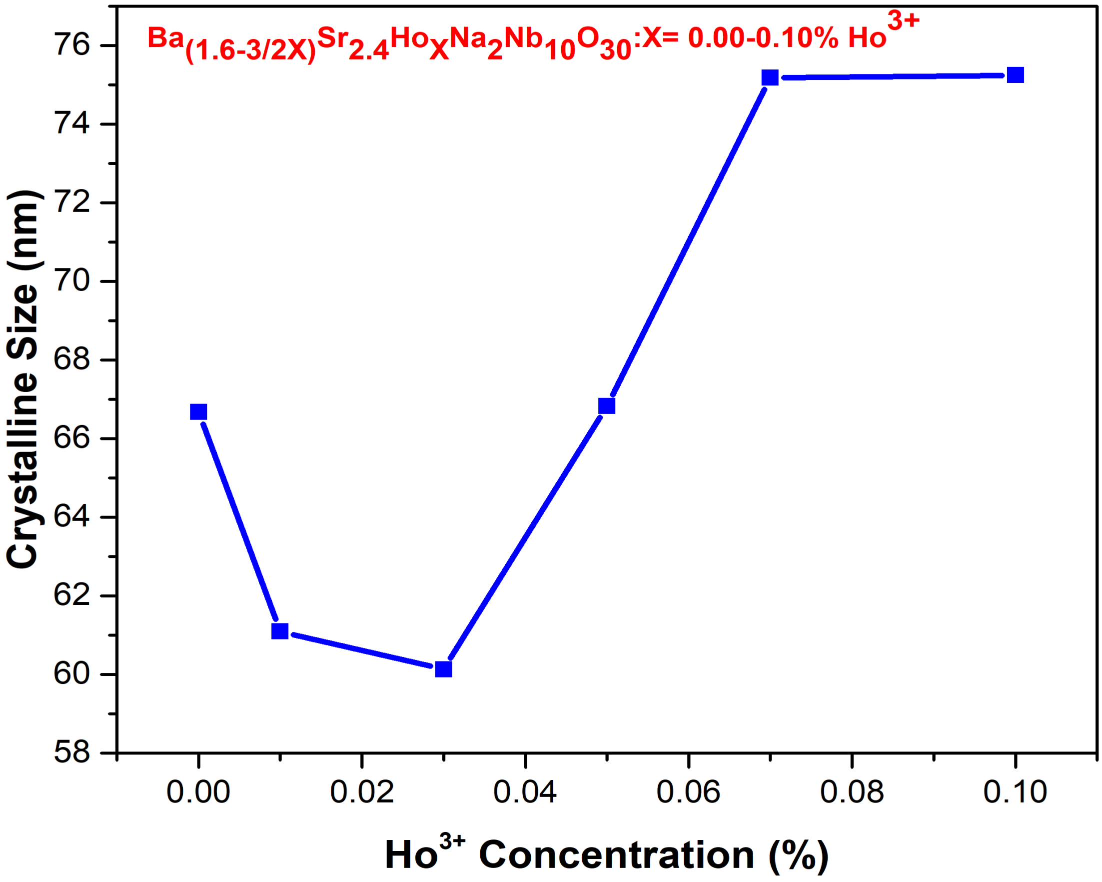

Figure 4.3: (Crystalline Size vs Concentration) of Holmium ion doped Barium Strontium Sodium Niobate Tungsten Bronze structured ferroelectrics nanomaterials for (x=0.00 - 0.10 % $Ho^{3+}$).

was in good agreement with JCPDS card number, (JCPDS 00-039-1453) [60].

Figure 4.4 Showed that by varying the concentration of Holmium ions, the position, distance, full width at half maximum and intensity of the XRD patterns changes for top three prominent peaks. On increasing the concentration, the position and distance do not vary significantly, they are stable. For the first three prominent peaks the average position is on $2\theta$ = 32, 29, 27 degree for peak1, peak2, peak3 respectively. Except at the beginning from 0.00 to 0.01, 0.03, 0.05, 0.07 and 0.10; where we observed slight decrease for all the three peaks, they attain the same value for all amounts of concentrations. The distance attains also stable values for the three

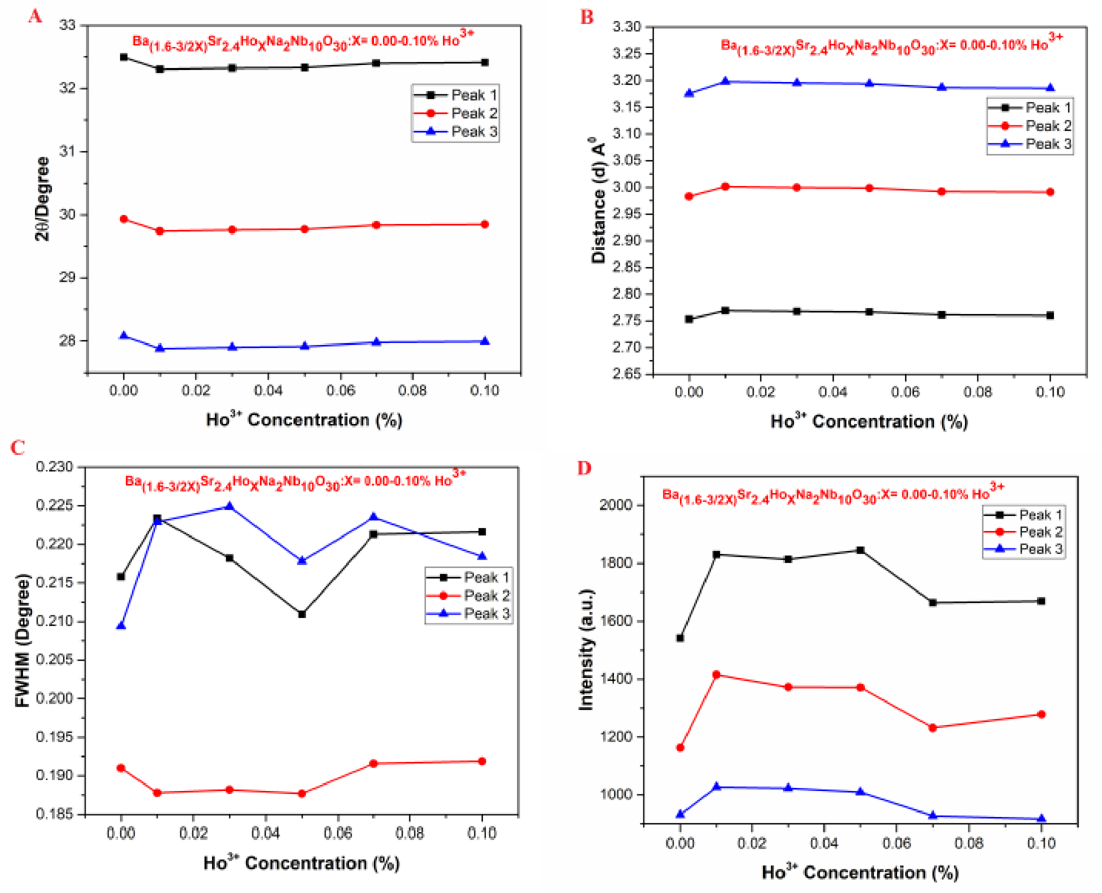

Figure 4.4: Holmium ion doped Barium Strontium Sodium Niobate Tungsten Bronze structured ferroelectrics nanomaterials.

peaks for increasing concentrations except at the beginning where we observe slight increase. For the case of FWHM as we increase concentration non uniform variation was observed. For the intensity, we obtained the optimum value for the concentration of 0.05% $Ho^{3+}$ and fluctuating values for others.

The TTB structure has general formula $(A1)_2(A2)_4(B1)_2(B2)_8(C)_4(X)_{30}$ (where X = fluorine or more commonly oxygen and A, B, C are metal cations) and consists of square A1-site, perovskite-like, units linked by B1-site $BO_6$ units, which together demarcate a large pentagonal tunnel, the A2-site (see Figure 4.5). A1- and A2-sites are crystallo-graphically distinct but both are occupied by larger cations [80]. Figure 5 showed the crystal structure of tetragonal tungsten bronze compound with formula

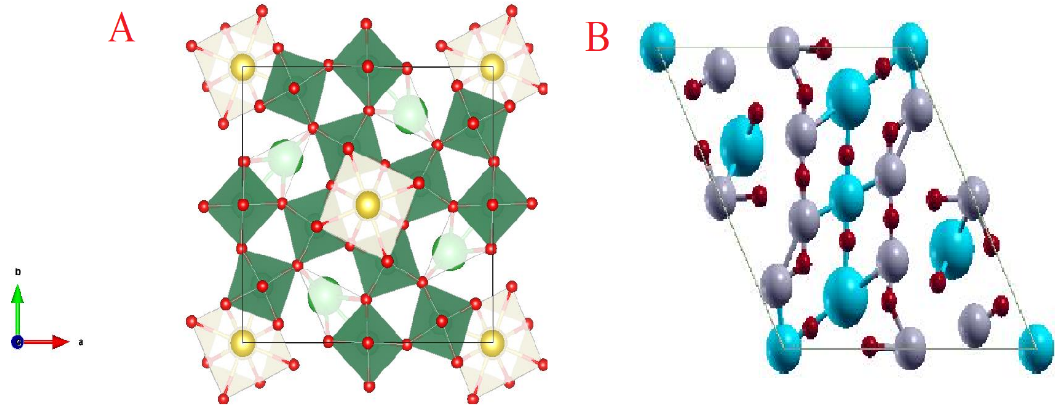

Figure 4.5: Crystal Structure of Tetragonal Tungsten Bronze Structure using VESTA (A) and XCRYSDEN (B).

$(A1)_2(A2)_4(B1)_2(B2)_8(C)_4(X)_{30}$ (where X = oxygen and A, B, C are metal cations) constructed by using the XCRYSDEN and VESTA (visualization for electronic structural analysis) software's respectively.

Table 4.2: XRD pattern data with different dopant concentration of $(Ba_{(1.6-3/2X)}Sr_{2.4}Na_2Nb_{10}O_{30} : xHo^{3+})$: tungsten bronze structured nanomaterials (For the three strongest peaks).

| S.N | **Quantity** | **0.00** | **0.01** | **0.03** | **0.05** | **0.07** | **0.10** |
|---|---|---|---|---|---|---|---|
| 1 | Crystallite Size (D) nm | 66.68 | 61.09 | 60.13 | 66.82 | 75.18 | 75.24 |
| 2 | Interplanar Dis. (d) $\mathring{A}$ | 2.75313<br>2.9829<br>3.17526 | 2.76898<br>3.00148<br>3.19776 | 2.76729<br>2.99962<br>3.19519 | 2.76649<br>2.99866<br>3.19519 | 2.76104<br>2.99217<br>3.18652 | 2.76002<br>2.99111<br>3.18523 |
| 3 | $2\theta$ (Degree) | 32.4954<br>29.9309<br>28.0794 | 32.3043<br>29.7416<br>27.8778 | 32.3246<br>29.7604<br>27.9007 | 32.3342<br>29.7702<br>27.9130 | 32.3998<br>29.8363<br>27.9782 | 32.4121<br>29.8471<br>27.9897 |
| 4 | Intensity (Counts) | 1541<br>1162<br>931 | 1830<br>1415<br>1027 | 1813<br>1372<br>1023 | 1845<br>1371<br>1009 | 1664<br>1251<br>927 | 1669<br>1278<br>917 |
| 5 | FWHM | 0.21580<br>0.19100<br>0.20940 | 0.22340<br>0.18780<br>0.22290 | 0.21820<br>0.18820<br>0.22490 | 0.21090<br>0.18770<br>0.21780 | 0.22130<br>0.19160<br>0.22350 | 0.22350<br>0.19190<br>0.21840 |

**Note** :

- Average Lattice Parameter: a= 12.33 $\mathring{A}$ , b=12.33 $\mathring{A}$ and c=3.93 $\mathring{A}$
- Average Volume of the unit cell: = 597.47$\mathring{A}^3$
- Average Density = 5.16
- Space Group = $P4bm$

### 4.3.2 Scanning electron microscopy (SEM)

The images obtained from scanning electron microscopy (SEM) showed morphology and microstructures as shown in Figure 4.6 & Figure 4.7. We used SEM to examine the morphology of samples, since the luminescence characteristics of nanoparticles depend on the morphology of the particles such as size, shape, size

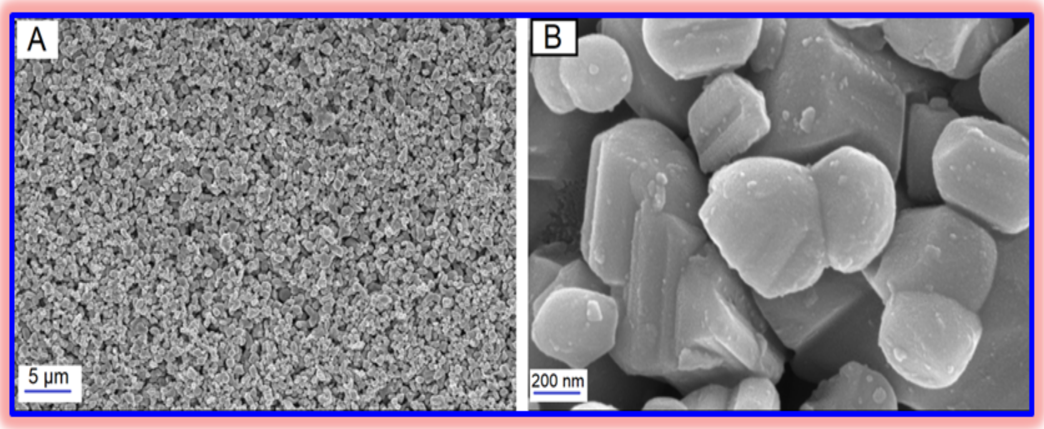

Figure 4.6: SEM image of $(Ba_{(1.6-3/2X)}Sr_{2.4}Na_2Nb_{10}O_{30} : xHo^{3+})$: x=0.00 %$Ho^{3+}$ for (A=5 $\mu$m, B=200 nm) dimension.

distribution, and defects so on. The scanning of SEM was performed in the ranges of (5 $\mu$ m to 200 nm) dimension and 1000 to 50,000 times magnifications to see all aspects that demonstrate the clear morphology of $(Ba_{(1.6-3/2X)}Sr_{2.4}Na_2Nb_{10}O_{30} : xHo^{3+})$ TTBs (See Figure 4.6 & 4.7). From the SEM image result, it was observed that the surface morphology of the particles distributions were nearly non-uniform and random for large dimensions and separate particles with different shape, size and size distributions are observed in nanometer dimensions. And they were aggregated tightly with each other. It was also clearly observed that the surface is less porous with different size and shape. It looks suitable and promising for different optical properties like a good absorption having more charge carriers available on the dense surface.

The surface morphology of two different dimensions (5 $\mu$m,and 200 nm) were presented in figure 4.6 A,B. The first image has uniform distribution of the homogeneous particles of the compound where as the second image clearly showed that separate particles with different shape, size and distributions.

Therefore we expect it will be promising surface structure for enhanced optical properties since all particles are distributed uniformly on the surface and there

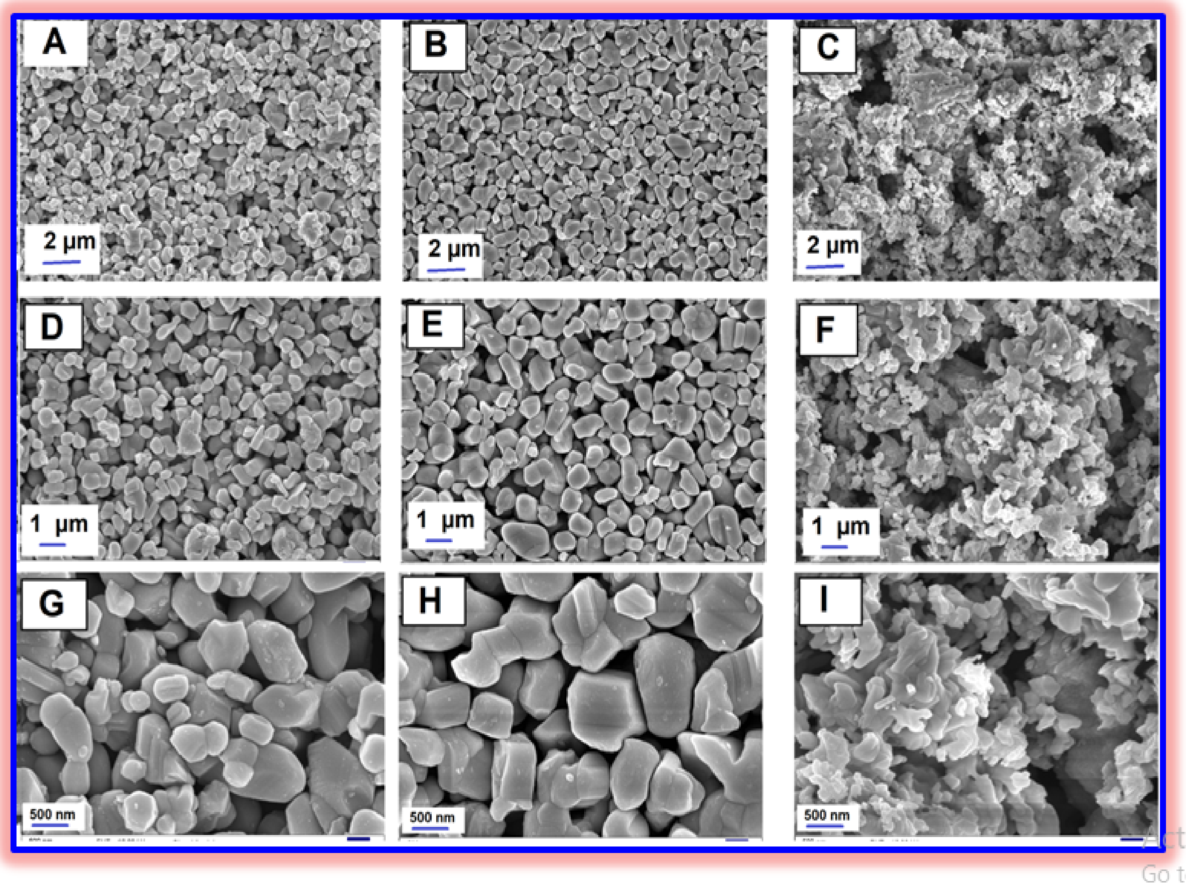

Figure 4.7: SEM image of $(Ba_{(1.6-3/2X)}Sr_{2.4}Na_2Nb_{10}O_{30} : xHo^{3+})$: A, D. G, x=0.00 % $Ho^{3+}$ . B ,E, H x=0.05 % $Ho^{3+}$ and C, F, I x=0.10 % $Ho^{3+}$ for 2$\mu m$, 1 $\mu m$ & 500 nm top down respectively.

were less porosity on the surface. The second zoomed image confirmed that, it's possibility of forming nanoparticles from the $(Ba_{(1.6-3/2X)}Sr_{2.4}Na_2Nb_{10}O_{30} : xHo^{3+})$ system with separate particles (200nm & 500nm, (see Figure 4.6 & 4.7).

Figure 4.7 with different dimensions and magnifications showed the possible types of the surface morphology of our system with and without dopants in comparison (x=0.00 %, 0.05 % and 0.10 %). Figure 4.7 also showed the clear difference in surface morphology having the same dimension and maginification but with and without dopants; signifying the effects of dopants with different concentrations. For instance Figure 4.7 C,F,I with excess concentration (0.10%) showed different surface morphology with more porosity that may not be promising to have better surface particles distribution.

### 4.3.3 Energy dispersive x-ray spectroscopy (EDS)

The EDS spectra confirms the standard stoichiometric combination of nanocomposite system of $(Ba_{(1.6-3/2X)}Sr_{2.4}Na_2Nb_{10}O_{30} : xHo^{3+})$ as shown in Figure 4.8 and Table 4.3. The elemental composition and mapping of the powder samples were measured using energy dispersive x-ray spectroscopy (EDS). Since EDS spectroscopy is complementary and standard procedures for determining and quantifying elemental composition of sample area as small as a few nanometers to micrometers; we have used it to identify all constitute elements of the as-prepared samples. The existence of Holmium $(Ho^{3+})$ ion in the corresponding EDS mapping was clearly observed especially when we add more dopants (0.10 %). As we expected apart from Barium (Ba), Strontium (Sr), Sodium (Na), Niobium (Nb) and oxygen (O) in $(Ba_{(1.6-3/2X)}Sr_{2.4}Na_2Nb_{10}O_{30} : xHo^{3+})$, there were no other emission observed in the EDS mapping of the Barium Strontium Sodium Niobate doped with Holmium ion (see Figure 4.8). The existence of Ba, Sr, Na, Nb, O and Ho, intense peaks are present which preliminarily indicates the formation of $(Ba_{(1.6-3/2X)}Sr_{2.4}Na_2Nb_{10}O_{30} : xHo^{3+})$ Tetragonal Tungsten Bronze Structured nanomaterial as shown in (Figure 4.8).

Figure 4.8 revealed and confirmed that all the constitute elements are available within expected range of proportion in accordance with our standard stoichiometric equation (see Figure 4.8 & table 4.3). Moreover, it further confirmed that there were no impurities added during our samples preparation. The EDS Layered image confirmed also that all the components (barium, strontium, sodium, oxygen and niobium and dopant holmium) of the TTBs are available in the nanocomposite materials. This also another way of confirming the quality synthesis procedures was used with uniform distribution of nanoparticles within the system of our samples.

Figure 4.9 is the Energy Dispersive X-ray Spectroscopy (EDS) result of the as prepared $(Ba_{(1.6-3/2X)}Sr_{2.4}Na_2Nb_{10}O_{30} : xHo^{3+})$ nanocomposite. The results further revealed that the experimental values of each constitute elements percentage molecular weight (Wt%) and atomic (At%) are in good agreement with the theoretically calculated values from the standard stochiometric equations (See Figure 4.9 & Table 4.3). Again this showed our advanced measutring instruments i.e. both EDS and digital electronic balace are well calibrated. The coincided experimental and theoretical molecular and atomic percentage values again confirmed that during the experiment all carbonates and oxides of our samples burned out well at 1100 $^0C$ temperature for 4 hrs duration in the furnace.

Figure 4.10 showed comparative analysis of our samples with and without dopants. Figure 4.10 A left sides color and black is the composite nanomaterial without dopants while the right sides are the separate constitute all five elements (Barium Strontium Sodium Niobium and Oxygen) only with different colors. Again it confirmed that only the expected elements were found without any additional impurities. Figure 4.10 B showed the same but in this case the dopant element availability was indicated clearly both in the left and right side images. This is another way of confirming we successfully added the dopant Holmium ion in our system in good proportion as also indicated with detail numerical figure in table 4.3 below.

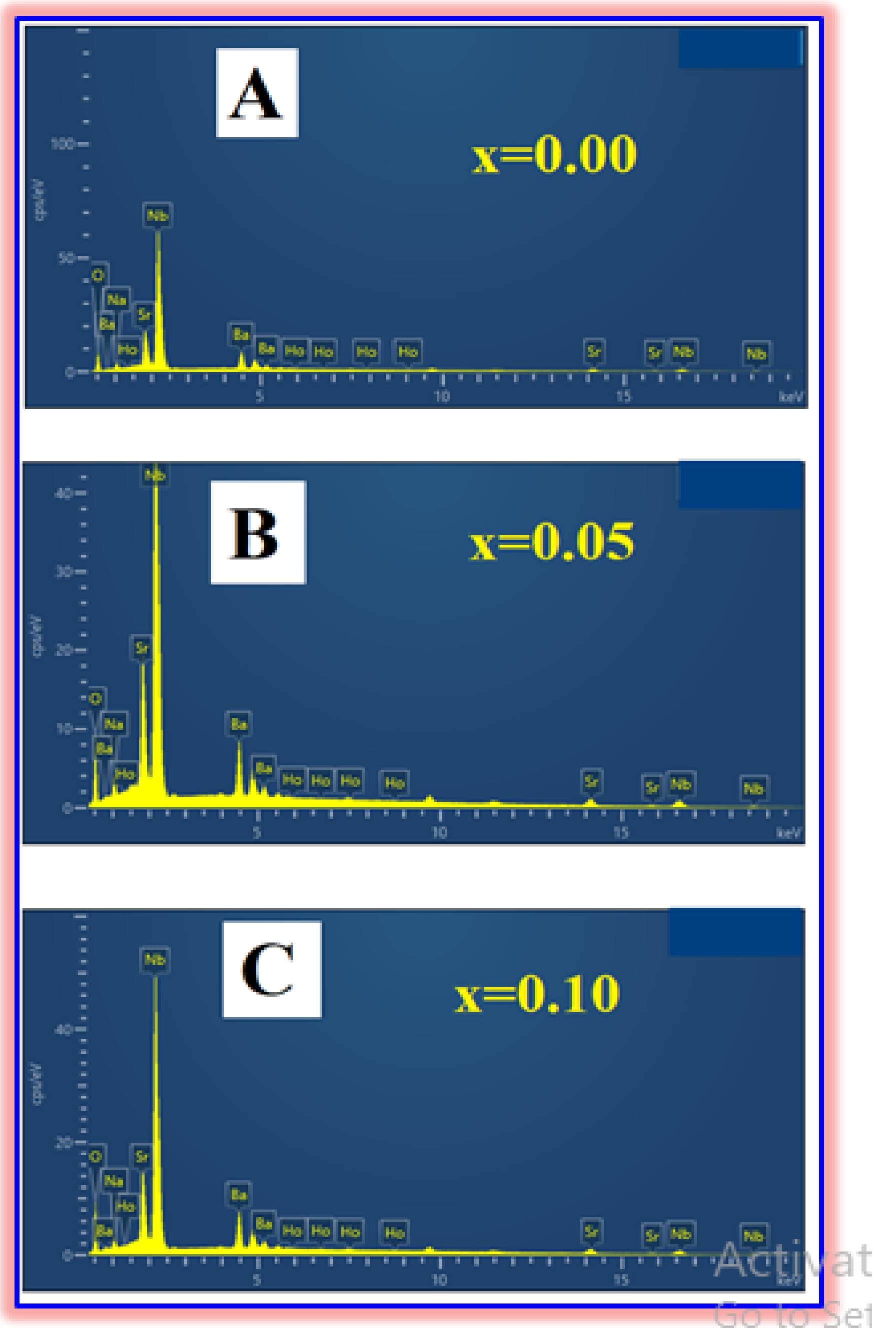

Figure 4.8: EDS Spectrum of $(Ba_{(1.6-3/2X)}Sr_{2.4}Na_2Nb_{10}O_{30} \ : \ xHo^{3+})$: A) x= 0.00 % $Ho^{3+}$ B) x= 0.05 % $Ho^{3+}$ & C) x= 0.00 % $Ho^{3+}$.

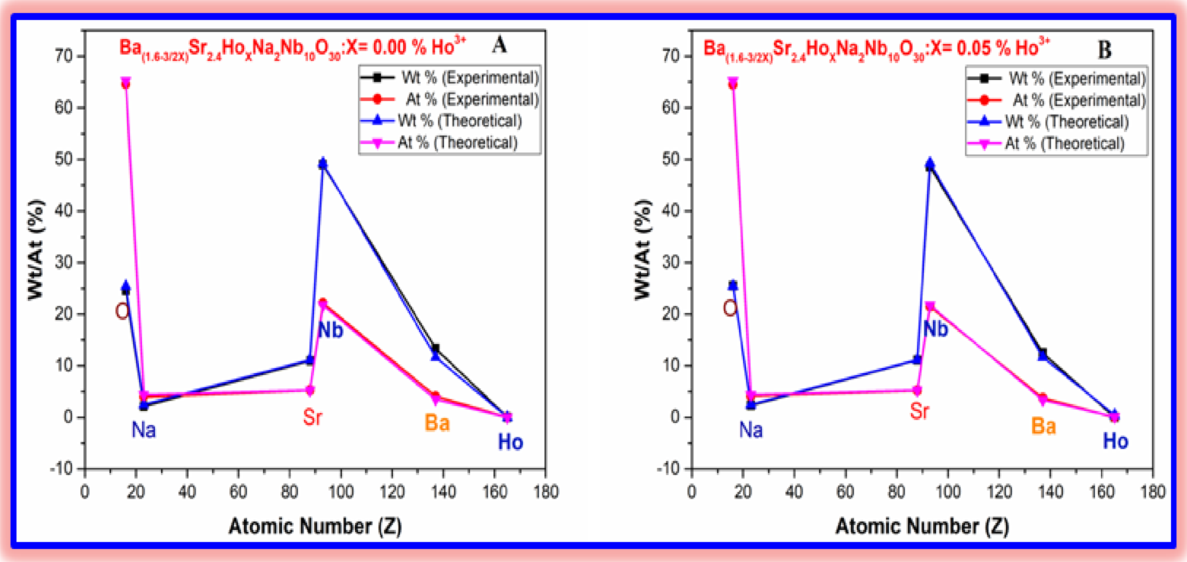

Figure 4.9: EDS Elemental Composition in Wt %/ At % for $(Ba_{(1.6-3/2X)}Sr_{2.4}Na_2Nb_{10}O_{30} \quad : \quad xHo^{3+})$ for comparison of Experimental and Theoretical Values:- A) x= 0.00 % $Ho^{3+}$ & B) x= 0.05 % $Ho^{3+}$.

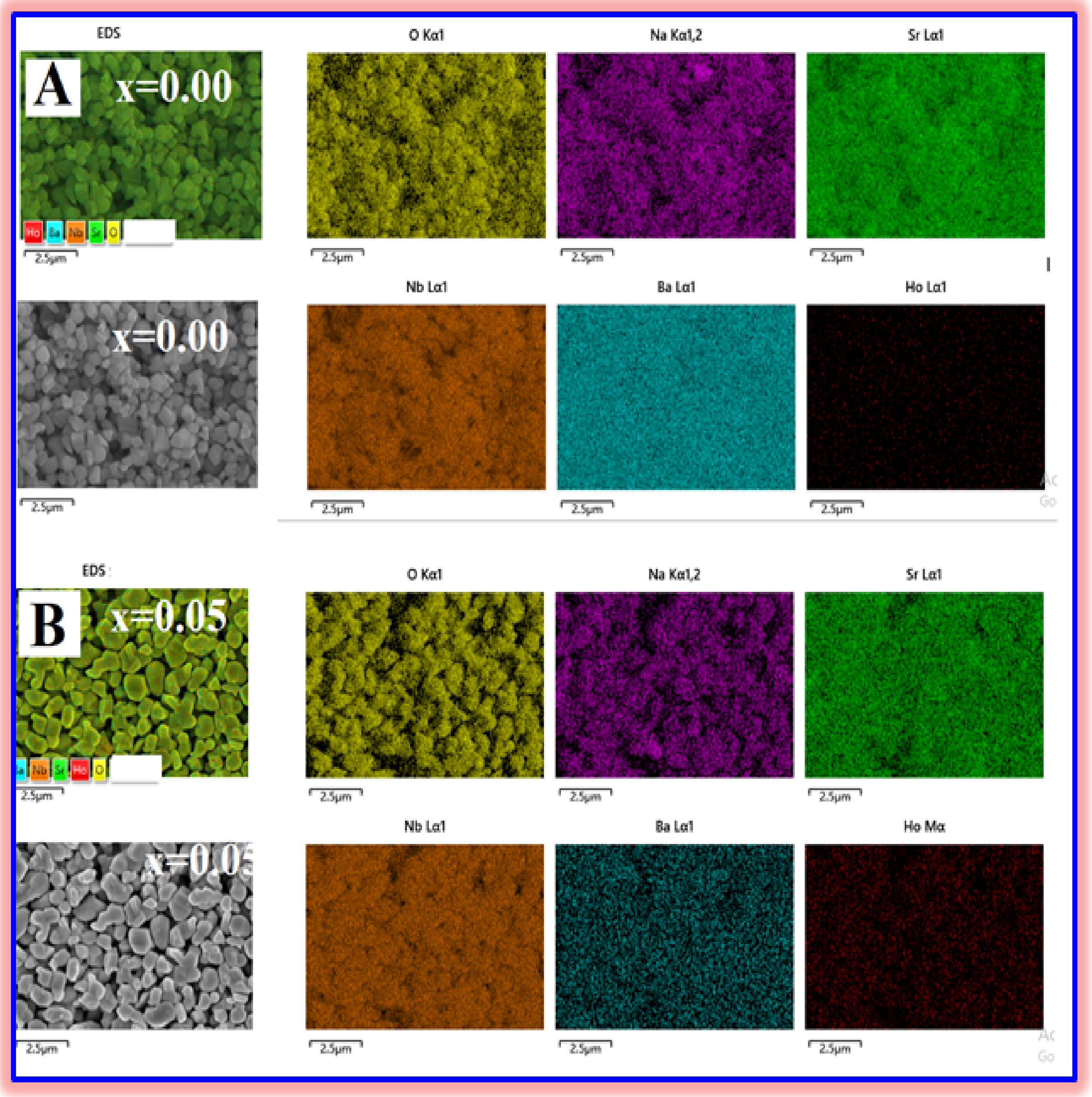

Figure 4.10: EDS Mapping of Barium Strontium Sodium Niobium Oxygen & Holmium $(Ba_{(1.6-3/2X)}Sr_{2.4}Na_2Nb_{10}O_{30} \ : \ xHo^{3+})$ : A) x= 0.00 % $Ho^{3+}$ , B) x= 0.05 % $Ho^{3+}$ (Map sum Spectrum).

Table 4.3: Constitute Elements Composing from EDS.

| | **Conc.(%)** | **Elnts** | **wt%**(Exp') | **At%**(Exp') | **wt%**(Theo.) | **At%**(Theo.) |
|---|---|---|---|---|---|---|
| | **x = 0.00** | **O** | 24.59 | 64.61 | 25.46 | 65.22 |
| | | **Na** | 2.13 | 3.96 | 2.44 | 4.35 |
| | | **Sr** | 10.96 | 5.26 | 11.16 | 5.22 |
| | | **Nb** | 48.98 | 22.16 | 49.29 | 21.74 |
| | | **Ba** | 13.34 | 4.08 | 11.66 | 3.48 |
| | | **Ho** | 0 | 0 | 0 | 0 |
| | | **TOTAL** | **100** | **100** | **100** | **100** |
| | **x = 0.05** | **O** | 25.53 | 64.48 | 25.46 | 65.22 |
| | | **Na** | 2.31 | 4.13 | 2.44 | 4.35 |
| | | **Sr** | 11.1 | 5.2 | 11.16 | 5.22 |
| | | **Nb** | 48.55 | 21.45 | 49.29 | 21.74 |
| | | **Ba** | 12.51 | 3.74 | 11.66 | 3.37 |
| | | **Ho** | 0 | 0 | 0.44 | 0.107 |
| | | **TOTAL** | **100** | **100** | **100** | **100** |
| | **x = 0.10** | **O** | 28.75 | 69.46 | 25.46 | 65.12 |
| | | **Na** | 2.02 | 3.39 | 2.44 | 4.35 |
| | | **Sr** | 10.52 | 4.64 | 11.16 | 5.22 |
| | | **Nb** | 44.6 | 18.56 | 49.29 | 21.74 |
| | | **Ba** | 13.72 | 13.86 | 11.29 | 3.26 |
| | | **Ho** | 0.38 | 0.09 | 0.88 | 0.22 |
| | | **TOTAL** | **100** | **100** | **100** | **100** |

In figure 4.11 we clearly observed that the color morphology of the system was changed as we added more and more concentrations of dopants with fixed interval ratios. The right side last images clearly indicated by red color showed more Holmium ions were present in the system relative to pure (0.00%) and 0.05 % $Ho^{3+}$ doped as presented in figure 4.10.

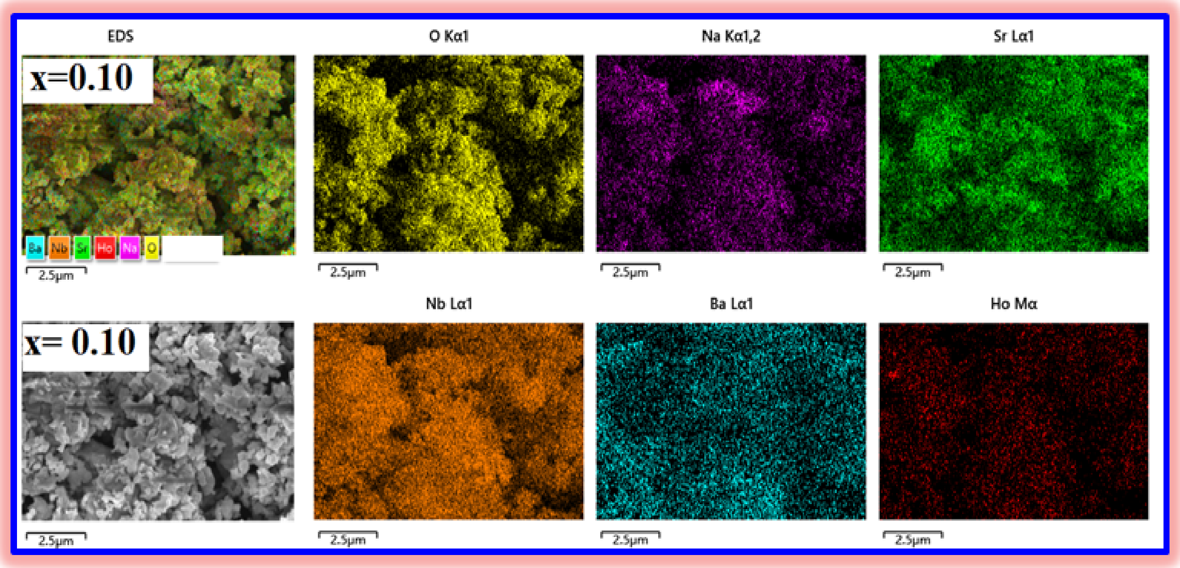

Figure 4.11: EDS Maping of Barium Strontium Sodium Niobium Oxygen & Holmium $(Ba_{(1.6-3/2X)}Sr_{2.4}Na_2Nb_{10}O_{30}\ :\ xHo^{3+})$: For x= 0.10 % $Ho^{3+}$ (Map sum Specrum).

### 4.3.4 Fourier transforms infrared spectroscopy (FTIR)

The Fourier transform infra-red spectroscopy (FTIR) spectrum has been widely used for the identification of organic and inorganic compounds. The FTIR spectra were recorded in the range of (4000 cm-1 to 400 cm-1) to obtain the figure print results. (FTIR) is also an essential characterization technique to identify the compositional elements of the material and to analyze the chemical bonding and functional groups present in the material.

FTIR spectra (Figure 4.12 A, B) of our samples calcined at $1100^0C$ showed collective metal - oxygen band vibration modes at 540.60 $cm^{-1}$ for (x= 0.00% $Ho^{3+}$) without dopant or pure host nanocomposite. But we observe additional band vibration modes at 429.92 for (x= 0.05% $Ho^{3+}$) $cm^{-1}$ with slight variation in wavenumber that may be due to ionic radius difference of the Barium, other metal ions and Barium substituted Holmium ions, having an additional peaks which indicates the

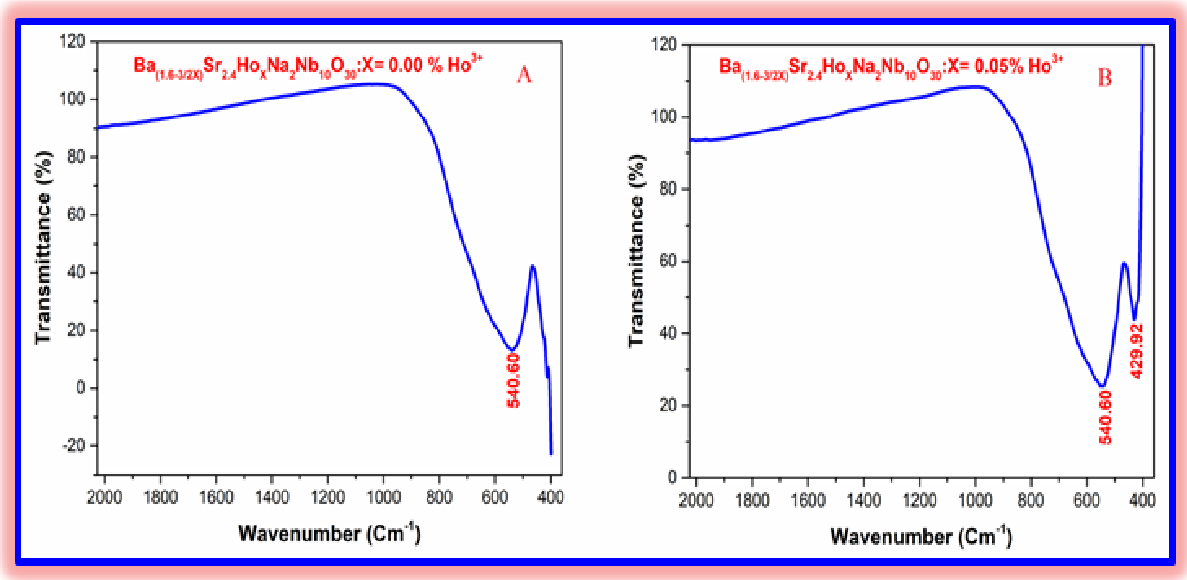

Figure 4.12: FTIR Spectra of $(Ba_{(1.6-3/2X)}Sr_{2.4}Na_2Nb_{10}O_{30} : xHo^{3+})$: A) x=0.00 % $Ho^{3+})$ , B) x=0.05 %$Ho^{3+})$.

existence of Ho - O, stretching band vibration modes since it was observed when we add the dopant ion only.

The FTIR results on Figure 4.12.B and Figure 4.13 indicated that in terms of two frequencies vibrations and stretching $\nu_1$ at (500-600 $cm^{-1}$), $\nu_2$ at (400-450) cm-1. We observed also as concentrations of dopants vary from 0.05 % to 1.0% we obtained more intense peaks with slight shift of the position to lower wavenumber position, except this we observed similar results for all dopants concentrations values consistently. The FTIR results also confirmed that our samples spectrum of holmium ion doped barium strontium sodium niobate powders calcined at 1100 $^0C$ in (Figure 4.12 B and Figure 4.13) absence of external impurities, which is also in a good agreement with literature values that in turn confirming our nanocomposite samples are pure i.e. without any impurities or defects [125].

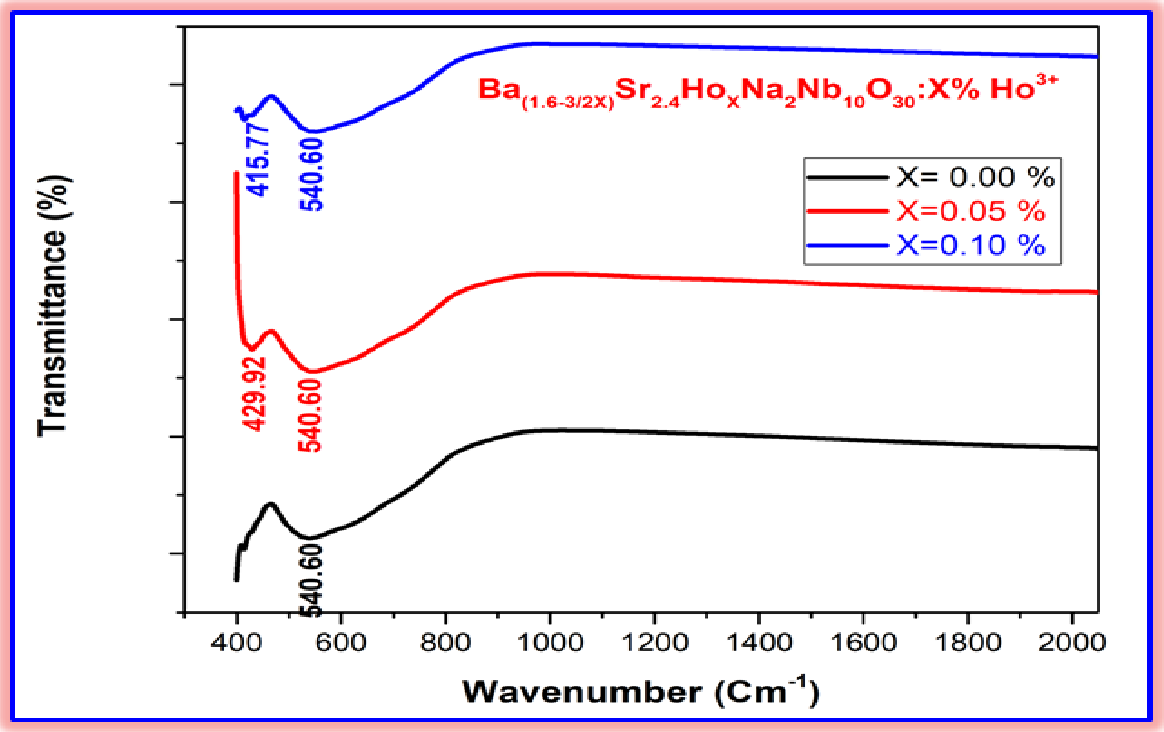

Figure 4.13: FTIR Spectra of $(Ba_{(1.6-3/2X)}Sr_{2.4}Na_2Nb_{10}O_{30} : xHo^{3+})$: x=0.00 % $Ho^{3+})$ , x=0.05 %$Ho^{3+})$ and x=0.10 % $Ho^{3+})$.

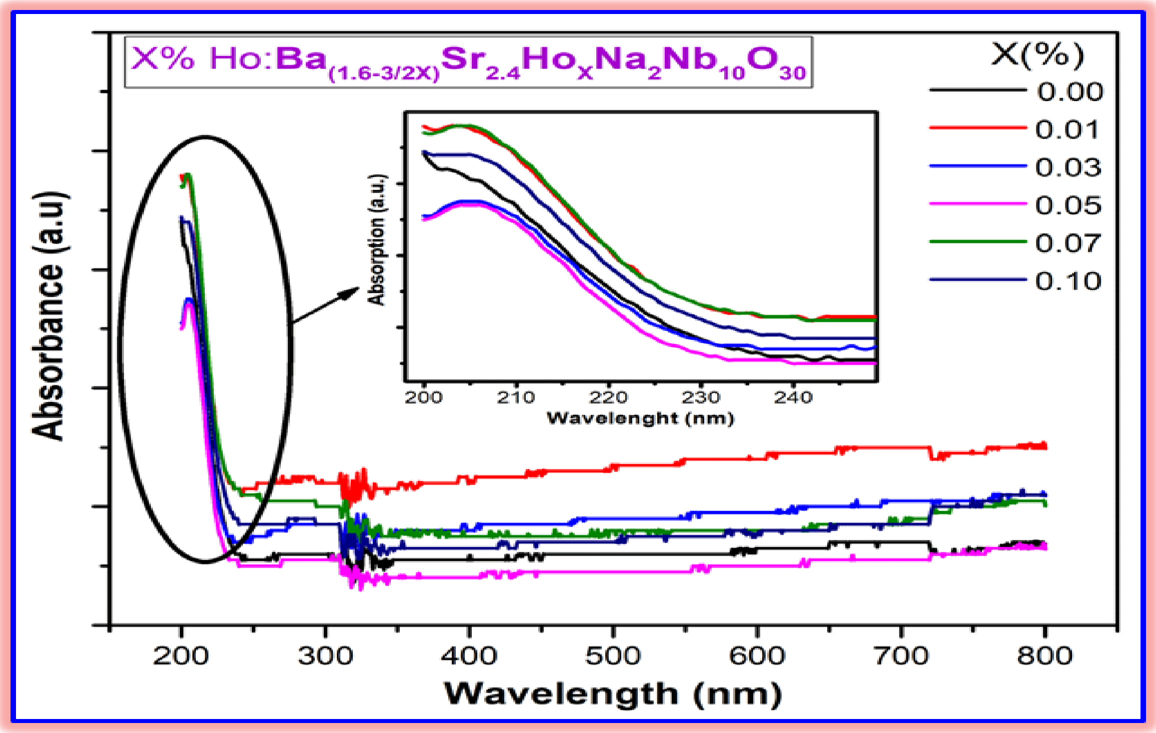

Figure 4.14: UV-Vis absorption spectra of $(Ba_{(1.6-3/2X)}Sr_{2.4}Na_2Nb_{10}O_{30} : xHo^{3+})$ ferroelectric materials.

### 4.3.5 UV-Vis Spectroscopy

Figure: 4.14. Showed the typical UV-Vis spectra of $(Ba_{(1.6-3/2X)}Sr_{2.4}Na_2Nb_{10}O_{30} : xHo^{3+})$ ferroelectric nanomaterial near UV. Figure 4.14 also displays that the absorption edges of all kinds of $(Ba_{(1.6-3/2X)}Sr_{2.4}Na_2Nb_{10}O_{30} : xHo^{3+})$ ferroelectric nanomaterial are at the same wavelength region of approximately 205 nm. From this we observed that $Ho^{3+}$ doping has significant effects on the peaks (intensity): when we vary the dopants concentration from 0.00% to 0.10% the absorption intensity become increasing with increasing concentration from 0.00-0.03% $Ho^{3+}$ ions, and then it tends to decrease when we keep on increasing from 0.05-0.10 % $Ho^{3+}$ ions concentration. Moreover, we observed the optimum absorption intensity obtained at x=0.03 % $Ho^{3+}$ ions concentration and no peaks at two extremes (0.00 & 0.10 % $Ho^{3+}$) ions concentrations.

The band-gap energy (E) can be calculated by the following equation [155]

$$E = \frac{1240}{\lambda} \tag{4.3}$$

where $\lambda$ is the wavelength in nanometers [156]. The calculated band-gap energy (E) corresponding to the 205 nm light wave is $\simeq$ 6.05 eV.

Doping and coating nanostructured materials with rare earths can be an effective way to enhance many interesting properties. Because rare earths act as good luminescence centers due to their narrow and intense emission lines arising from 4f internal transitions [157] , moreover, rare earths are very reactive and tend to form oxides very easily [158]. Among the rare earths, Holmium was selected as a promising element because it fluoresces in the visible and near-infrared regions and is promising for communication window and solid-state lasers [159].

The effects of Holmium ion doping revealed in our experiments are: i) from the XRD analysis the highest intensity was obtained at 0.05% $Ho^{3+}$ with (1845 a.u). The crystallinity of the system was also confirmed by the lattice parameters a= 12.33 $\AA$, b=12.33 $\AA$ and c=3.93 $\AA$. The average density = 5.16, average Volume of the unit ce11 = 597.47 $\AA^3$ , the average dislocation density = 2.19 x $10^{-4}/nm^2$ and space group = P4bm that confirmed Tetragonal Tungsten Bronze structured nanomaterials [146]. The SEM result further confirmed that by excess concentration (0.10 % $Ho^{3+}$) the surface morphology changed to non-uniform and more porous (see Figure 7: C, F & I). The FTIR results revealed also the dopant enhance the absorption in near Infrared region with 0.05% $Ho^{3+}$. The UV-Vis showed also optimum value obtained at wavelength of 205 nm with concentration of 0.03 % $Ho^{3+}$ that in turn signified the effect of Holmium dopant where no absorption peaks were observed at two extreme concentrations (0.00 & 0.10 %$Ho^{3+}$).

Table 4.4: Comparative Analysis of Currently reported work VS Previously reported related work.

| S.N | **Current Work** | **Previously reported Work** |
|---|---|---|
| 1 | Successful Synthesis of $Ba_{(1.6-3/2X)}$ $Sr_{2.4}Na_2Nb_{10}O_{30} : xHo^{3+}$ | More emphasis given for computational |
| 2 | Addition of rare earth ion $Ho^{3+}$ without affecting the crystal Structure phase | Doping La, Sm, $Dy^{+3}$, $Y^{+3}$ reported[71, 83] |
| 3 | Identified crystallite phase with TTBs Successfully with the unit cell average size 67.52 nm | Rarely reported the experimental results [160]. |
| 4 | Producing suitable and less porous and nearly uniformly distributed particles obtained from SEM images. | With different quality and porosity and Particle distributions |
| 5 | All constituent components elements demonstrated in EDS mapping,demonstrated in EDS mapping, with best match of Experimental results and theoretical calculated values | With different quality and porosity and Particle distributions Experimentally it was rare to avoid impurities and defects |
| 6 | Promising absorption properties near UV region observed at wavelength of 205 nm (0.03 % Ho3+) having optimum value. | Rare earth ion doped had similar result with sufficient ionic radius difference on A1 and A2 site ions.[83] |

## 4.4 CONCLUSION

XRD analysis of Holmium doped Barium Strontium Sodium Niobate ferroelectrics nanomaterials revealed Tetragonal Tungsten Bronze structured nanomaterial successfully synthesized through conventional high temperature synthesis route. The identified crystal phase has an average crystallite size of 67.52 nm, having space group of p4bm and lattice parameters of a= 12.33$\mathring{A}$ , b=12.33 $\mathring{A}$ and c=3.93 $\mathring{A}$. The XRD pattern obtained showed also a best match with JCPDS card number-00-039-1453. Further analysis of XRD result indicated the highest intensity value (1845 a.u.) was obtained for the concentration of 0.05 % $Ho^{3+}$ ions. SEM and EDS analysis of surface morphology and elemental compositions of Holmium doped Barium

Strontium Sodium Niobate ferroelectrics Tetragonal Tungsten Bronze structured nanomaterial showed clear and best quality surface morphology, microstructure and elemental mapping. The SEM images have also shown separate nanoparticles with different shapes, size and size distributions with random distributions. Moreover the micro level dimension showed relatively uniform distribution of particles and less porosity of the surface. The surface morphology is promising for enhancing optical properties of the system because of its homogeneous surface microstructure having dense nanoparticles distributions. The EDS results confirmed that all the constitute elements are found in correct proportion to the standard stoichiometric ratios. In addition it confirmed that there were no impurities added during the synthesis and characterization which in turn confirming high quality synthesis procedures were employed. The experimental and theoretical molecular weight and atomic percentage coincidence also indicating that the composites made in best quality and proportion synthesis approach. The FTIR analysis result indicated also the collective metal oxide single peak for the bond vibration at wave number of 540.60 $cm^{-1}$ as expected since in the finger print of FTIR values of metal oxides were commonly found 400 - 600 cm-1 and the Holmium oxygen bond vibration modes at (0.05% $Ho^{3+}$), 415.77 (0.10 % $Ho^{3+}$) 429.92 $cm^{-1}$ which was not seen for the system without dopant.

# 5

# Investigation of Barium Strontium Sodium Niobate Ferroelectric nano-material with Holmium ion additive for Optoelectronic Application

## 5.1 Introduction

Due to their unique ferroelectric properties associated with morphologies, ferroelectric nanostructures have been the subject of much research recently. Specific property variations in phase transition or Curie temperature $(T_C)$, dielectric constants, coercive fields, spontaneous polarization levels, and piezoelectric response levels are endowed with characteristic low dimension ferroelectric materials. Furthermore, reductions in dimensions and size can promote the creation of single domain structures, which can dramatically enhance ferroelectric properties. Consequently, there is a lot of promise for ferroelectric nanostructure in non-volatile memory, sensors, microelectromechanical systems, FE-PV devices, non-linear optics, and nanogenerators. While there are still obstacles standing in the way of the actual use of nanodevices, significant advancements have been made in the research of nanostructured ferroelectrics in recent years (including synthesis, characteristics, and applications), although barriers to the practical application of nanodevices remain. Therefore, it is essential to provide experimental results of this promising novel nanostructure form [161, 162]. The Tetragonal Tungsten Bronze (TTB) structures recently received considerable attention because of their compositional flexibility and largely due to the structural freedom for modification and tailoring of their physical properties [5, 163]. The chemical formulae $(A1)_2(A2)_4C_4B_{10}O_{30}$ and $(A1)_2(A2)_4B_{10}O_{30}$ where A1, A2, C and B were 15, 12, 9 and 6-fold oxygen-coordinated points in the crystal, which were correlated to $K_xWO_3$, $Na_xWO_3$ compounds are called tungsten bronze structure (TBs) compounds. The first one represents a filled bronze structure, where all sites A, B and C is occupied (e.g., $K_6Li_4Nb_{10}O_{30}$). The 2nd formula represents bronze that is either filled (all A sites occupied, e.g., $Ba_4Na_2Nb_{10}O_{(30)}$) or partially filled (5/6 of the A sites occupied, e.g., $Pb_5Nb_{10}O_{(30)}$) [134, 160]. TB materials exhibit either tetragonal or orthorhombic symmetry. The quadrangular TBs was explained by Magneli and Blomberg [133, 134], Wadsley [135], Francombe [86] and by Jamieson et al.[70]. TTBs consists of ten distorted octahedral common angles, so that 3 various spaces (two Tetragonal A1, four Pentagonal A2, and four Triangular C) are available for cations of the general formula $(A1)_2(A2)_4(C)_4(B1)_2(B2)_8O_{30}$ [70]. The flexibility of the structure of TB-oxides opens new rooms for non-lead based ferroelectric nanomaterials. In a look for lead-free novel materials for the development of new nanomaterials, TTBs are among attractive candidates. The various positive ion sites in the TTB structure permit for a wide range of chemical compositions, compositional flexibility and consequently opening the possibility of controlling the main characteristics features of TTBs [50-53]. High toxicity of lead containing compounds and high process pressures, which cause serious environmental contaminations, have focused and attracted the attention of many researchers on Pb-free electro-ceramics that reduce lead pollution. Among them the tungsten bronzes are the frontier candidates. Due to the increasing interest and demand, many studies have recently focused on the production of good quality lead-free ferroelectrics nanomaterials [144, 145].

To improve many interesting properties in nanostructured materials, recently doping them with rare earths ion is considered as an effective way. As a matter of fact the rare earths act as excellent luminescence centers because of their narrow and intense emission line due to internal 4f transitions [157], and they are also very reactive and tend to form oxides very easily [158]. They were chosen as a promising elements because of their fluoresce in the visible and near-infrared regions. They are also highly promising for communication window and solid-state lasers applications [159]. Among them one is holmium ions $Ho^{3+}$. Taking into account the preliminary research outputs reported so far, the current studies revolve across the potential application of nanomaterials for imparting photoluminescence (PL) in materials [54, 55]. In addition, rare earth based crystals which follow the guest-host phenomenon to independently optimize the luminescence and crystal properties of the system has given due attention. It was also considered and focused as a central point in the system [56]. Rare earth oxides under the wide energy bandgap semiconductor have also drawn special attention due to their tunable electronic and optical characteristics features [57]. As a result of these remarkable features, the prepared ferroelectric nanomaterials and their characteristic photoluminescence response with various concentrations at different excitation wavelengths are in need of clear explanation. Again, the detailed mechanisms that tune the luminescence of nanomaterials of ferroelectrics types are not yet fully understood.

Demonstrating aforementioned gaps, this article presented the study analysis of UV-Vis and PL properties of $Ho^{3+}$ doped barium strontium sodium niobate ferroelectrics prepared using solid state reaction methods for optoelectronic applications. Structural Phase identification was studied using XRD diffractometer. Absorption spectra were investigated by Ultraviolet-Visible spectroscopy, the emission and excitation spectra were analyzed by PL, the different non-centrosymmetric bond vibration was studied by FT- IR.

## 5.2 Experiment

### 5.2.1 Synthesis

Ferroelectric nanomaterials with a tungsten bronze structure $(Ba_{(1.6-3/2X)}Sr_{2.4}Na_2Nb_{10}O_{30} : xHo^{3+})$ or (BSNN: xH) via a conventional solid state high temperature reaction methods using carbonates (99.99%) and Oxides (99.99%) from Sigma-Aldrich companies as precursors according to their normal stoichiometric ratio (X =0.00 - 0.10 % $Ho^{3+}$) was successfully synthesized. Mass of each sample was measured using digital electronic balance. A gray-black Agate mortar and pestle of a six-inch in diameter mortar was used to ground the powder for 3 hours before being placed in a furnace. Then the ground powder was added in platinum coated crucibles and heated at 1100 $^0C$ for 4 h at a heating rate of 5 $^0C$ per minute using programmable furnace. Meanwhile to realize a complete reactions and diffusion processes to takes place, considerably sufficient time was given for further grinding. Again to make it a very refined and miniaturized (nano-sized) powder, the powder was ground for another 2 hours after the furnace. The resulting pure white powders were then made to be ready for characterization and further analysis.

Table 5.1: The stoichiometric equation of the nanocomposite

| **Quant.** | **Raw matr.** | | | | | **Product** |
|---|---|---|---|---|---|---|
| | $BaCO_3$ | $SrCO_3$ | $Na_2CO_3$ | $Ho_2O_3$ | $Nb_2O_5$ | $BSNN : xHO$ |
| **x=0.01** | 312.77439 | 354.3048 | 105.98654 | 1.889185 | 1329.0388 | 1884.48428 |
| Req.Qnt | 4.1493367 | 4.70028861 | 1.40604171 | 0.02506236 | 17.631333 | 75.3793712 |
| **x=0.03** | 306.85437 | 354.3048 | 105.98654 | 5.667555 | 1329.039 | 1883.79242 |
| Req.Qnt | 4.0722954 | 4.70201489 | 1.406558107 | 0.0752147 | 17.637809 | 75.3516968 |
| **x=0.05** | 300.93435 | 354.3048 | 105.98654 | 9.445925 | 1329.0388 | 1882.32322 |
| Req.Qnt | 3.9968474 | 4.70568492 | 1.40765596 | 0.12545567 | 17.651575 | 75.2929288 |
| **x=0.07** | 295.01433 | 354.3048 | 105.98654 | 13.224295 | 1329.0388 | 1882.1496 |
| Req.Qnt | 3.9185824 | 4.706119 | 1.40778581 | 0.17565414 | 17.653204 | 75.285984 |
| **x=0.10** | 286.1343 | 354.3048 | 105.98654 | 18.89185 | 1329.0388 | 1880.91749 |
| Req.Qnt | 3.8031214 | 4.70920178 | 1.408707992 | 0.25109887 | 17.664767 | 75.2366996 |
| **Total** | **19.94018** | **23.523309** | **7.0367496** | **0.6524857** | **88.23869** | |

### 5.2.2 Characterization

The x-ray diffraction pattern was obtained from x-ray powder diffractometer (Phillips XPERT-PRO Model): by making use of Cu-$K\alpha$ radiation ($\lambda$=1.5406 $\mathring{A}$) at 40.0 KV, 30 mA) over (2$\theta$ = 10 to 80 $^{0}$) range. Ultra Violet-Visible Spectroscopy (the powder in solution form using de-ionized water solvent) was used to measure the absorption. The solution of 100 ppm was centrifuge and used for UV-Vis spectroscopy analysis. Photoluminescence emission spectra of the samples (in solution form) were measured by Cary Eclipse serial number My1849002 model fluorescence spectrophotometer with slits of emission and excitation lights of 10 nm and 600 nm per minute scanning rates. Shimadzu IR Prestige-21 FTIR Spectrometer were used to record the FT-IR spectra of the as synthesized sample powders for investigating finger print functional groups.

## 5.3 Results and Discussions

### 5.3.1 XRD Analysis

In order to determine the phase structure, powder XRD analysis has been carried out. The smooth and sharp peaks can confirm the crystalline nature of the samples in the XRD pattern, and all the samples are pure tetragonal tungsten bronze structures ferroelectric nanomaterials (Fig.5.1).

Powder X-ray Diffraction analysis has been used in order to determine phase structure of as prepared powder samples. The typical XRD patterns of BSNN: xH, TBs ferroelectric nanomaterial is shown in Figure 5.2. A.

Smooth, sharp and uniform peaks in the XRD pattern were obtained for all types of dopant concentration and without dopant. It was also consistent with all concentration values of x = 0.01 - 0.10 $Ho^{3+}$. The peak having maximum intensity of (1845.00 a.u.) which is obtained for a concentration of 0.05%Ho3+ at the position of ($2\theta$ = 32.33 Degree) (see Table 5.1). A positive impact of the additive holmium cation and its vital role were also observed in the XRD pattern results. As reported by Mag-

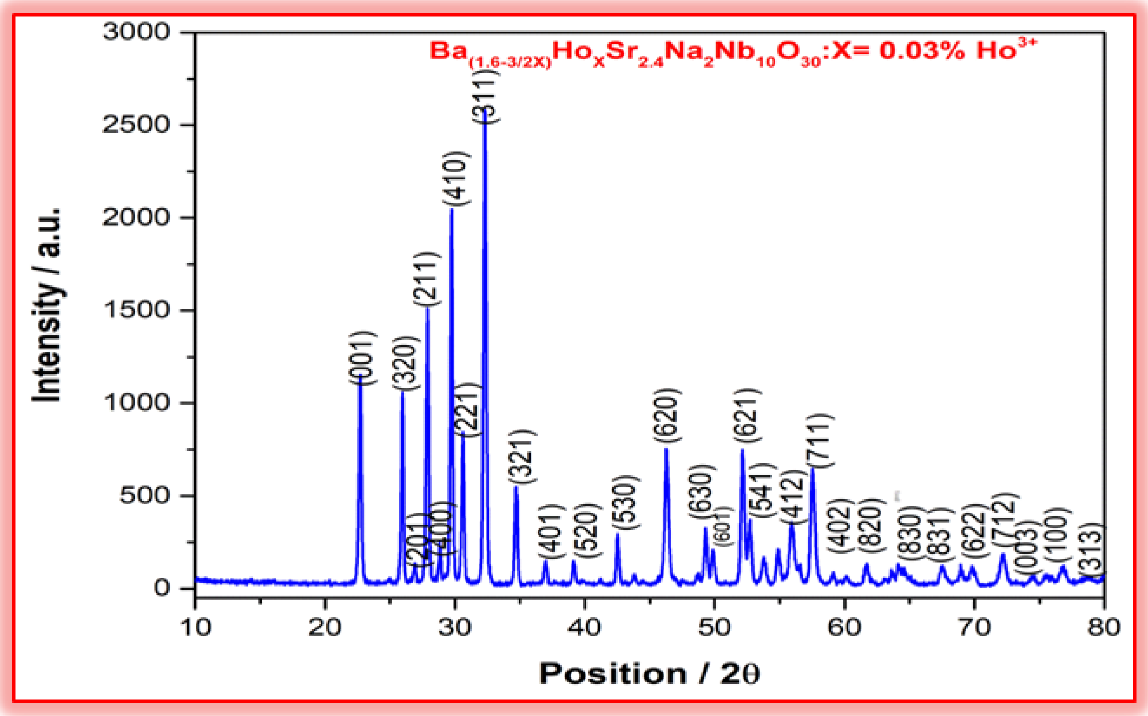

Figure 5.1: XRD pattern of Holmium ion doped Barium Strontium Sodium Niobate: Tungsten Bronze Structured Ferroelectrics nanomaterials for (x= 0.03 % $Ho^{3+}$).

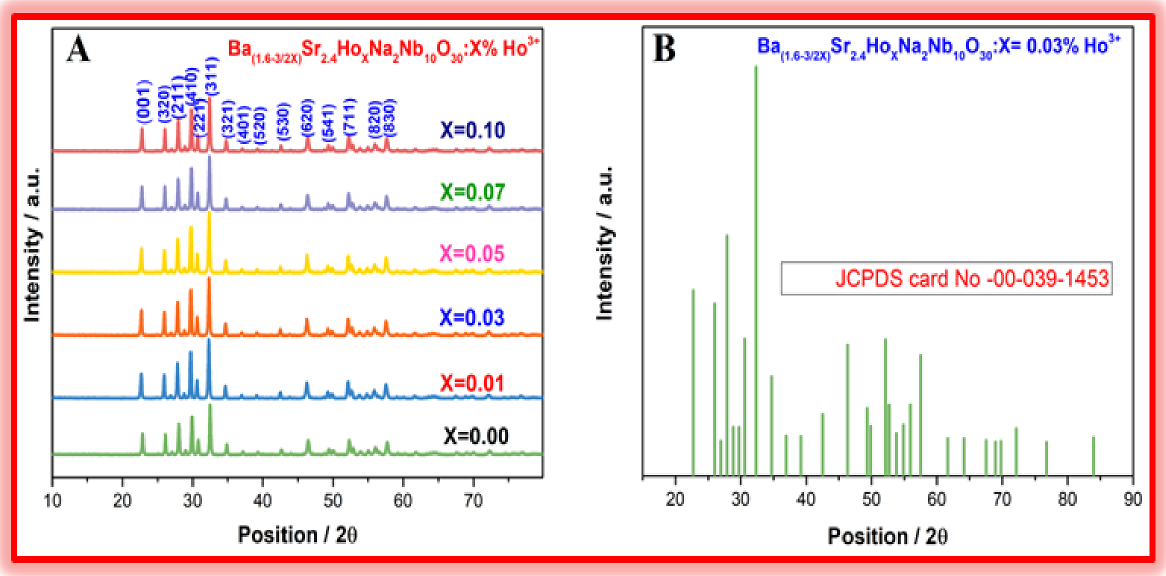

Figure 5.2: XRD pattern of BSNN: xH for A) x= 0.00-0.10 % $Ho^{3+}$ with miller indices, B) JCPDS Card Match.

neli and Blomberg [133], the same outcomes were obtained and verified against the JCPDS of the TTB structural phase. Recently reported XRD pattern matching that has a direct match and nice agreement with the JCPDS 00-039-1453 card number has also a good match with the obtained results.

The mean crystallite size (D) of the crystal is determined to be (67.5) nm for the strongest peak (311), using the Debye-Scherer formula for the BSNN: xH ferroelectric nanomaterial, The Debye-Scherer formula is also given by:

$$D = \frac{\kappa\lambda}{\beta cos\theta} \tag{5.1}$$

where $\lambda$ is the wavelength of the incident x-ray beam ($\lambda$ = 1.5406 $\mathring{A}$), $\kappa$ is Scherer's constant with a value of 0.94, $\theta$ = the corresponding Braggs diffraction angle and, $\beta$ = FWHM (full width half maximum) of the peaks [152].

It was well known that particle size and morphology have a huge influence on the behaviors of nanocomposite materials [122, 154]. In determination of holmium ion concentration as a function of crystallite size, it was indicated that increasing the impurity concentration from the reference (0.00 - 0.03) decreases the size of BSNN: xH. Meanwhile, size of crystallite increased as the impurity content increases from 0.03 - 0.07. The least crystallite size obtained for concentration of the prominent peak having 0.03% $Ho^{3+}$ is 60.10nm. The XRD pattern (Figure 5.2. B) from the analysis of the calcined powder also showed a tetragonal tungsten bronze structure ferroelectric phase, that was in nice agreement with the card number (JCPDS 00-039-1453) was obtained [70].

### 5.3.2 UV-Vis.Spectroscopy

Figure 5.3 Displayed typical UV-Vis spectra of BSNN: xH ferroelectric nanomaterial near Ultra violet. It further shows that all BSNN: xH ferroelectric nanomaterials have absorption edges in the same wavelength range around 205 nm. Again, $Ho^{3+}$ doping results in having a significant effect on the peaks intensity. As doping concentrations vary from 0.00 - 0.03% the absorption increased with increasing

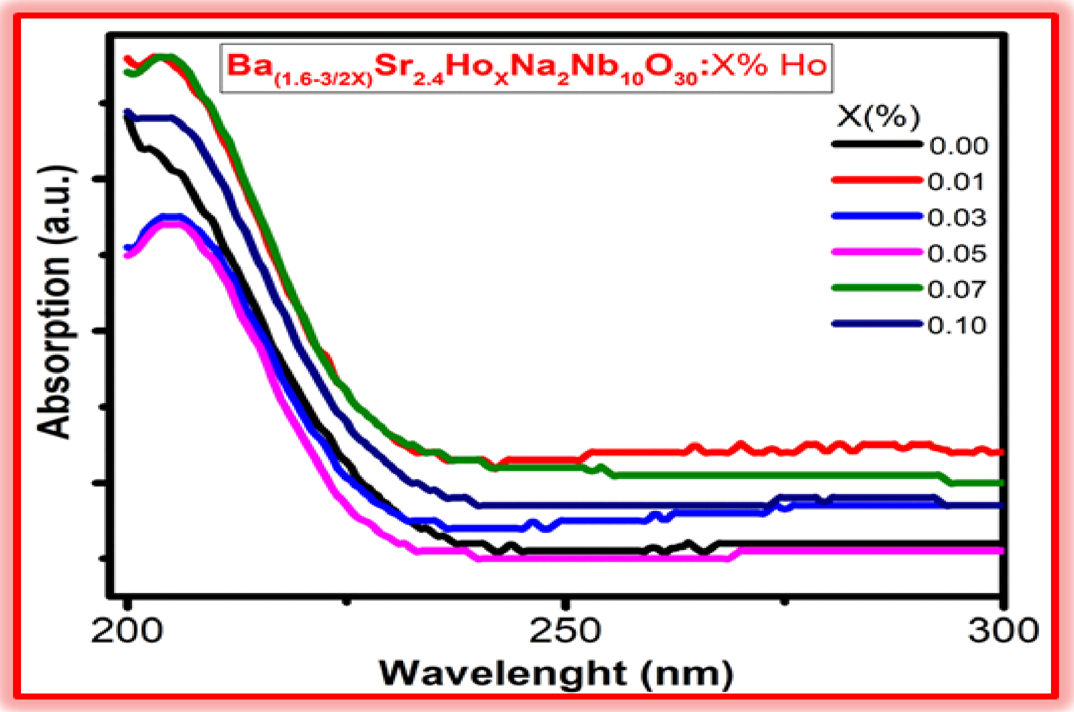

Figure 5.3: Spectra of UV-Vis absorption for BSNN: xH ferroelectric nanomaterials.

concentration. Then it became decreasing as we continue to increase the concentration of $Ho^{3+}$ from 0.05 to 0.10%. (See Figure 5. 3)

Moreover, the experimental result also revealed that the optimum absorption obtained for the value x = 0.03 % $Ho^{3+}$ concentration. Meanwhile at the two extreme x values (for x=0.00 & x=0.10 %) there were no observable absorption peaks.(See figure 5. 4)

The mathematical formula used to calculate the band gap $(E)$ was given by a formula [155]:

$$D = \frac{1240}{\lambda} \tag{5.2}$$

where $\lambda$ is the wavelength [156]. For the approximately determined band-gap $(E)$ corresponding to a 205 nm is $\approx$ 6.05 eV.

As shown in Figure 5.5, the UV-Vis result obtained for x = 0.03% ions concentra-

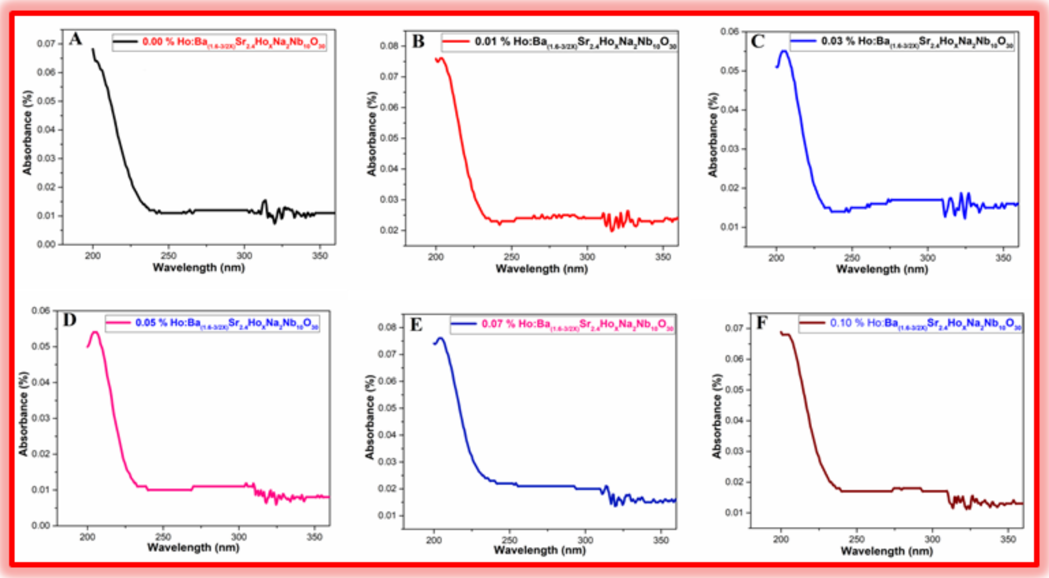

Figure 5.4: Spectra of UV-Vis absorption of BSNN: xH (for x = A) 0.00, B) 0.01, C) 0.03, D) 0.05, E) 0.07 & F) 0.10 % $Ho^{3+}$.

tion with different solvent to solute ratio has different absorption intensity values. We prepare 50 ppm and 100 ppm solutions and test the intensity of the absorption. Even though the absorption occurred at the same wavelength of around 205 nm there was a significant difference for the two different solutes to solvent ratios. The more concentrated showed intense absorption spectra (see Figure 5. 5)

### 5.3.3 Scaning Electron Microscpe (SEM)

SEM is implemented to analyze the surface micro-structure of the synthesized sample powders: size, shape, and size-distribution, because the luminescent properties of nanoparticles are based on the morphology of the particles. The images obtained by scanning electron microscope (SEM) show the morphology and microstructures as shown in Figure 5.6 and 5.7. We used SEM to study the morphology of the samples because the luminescent properties of nanoparticles 97.83 nm (SEM image, ImageJ software) depend on the morphology of the particles; such as size, shape, size distribution.

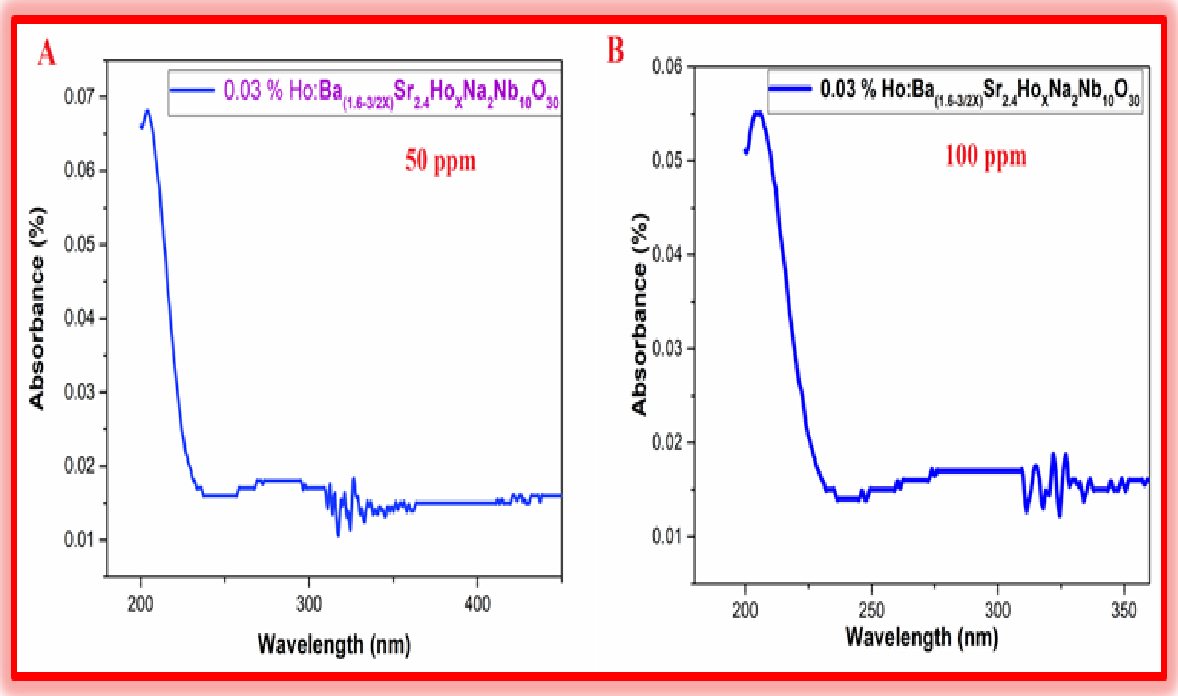

Figure 5.5: Spectra of UV-Vis absorption of BSNN: xH A) for 50 ppm, B) for 100 ppm.

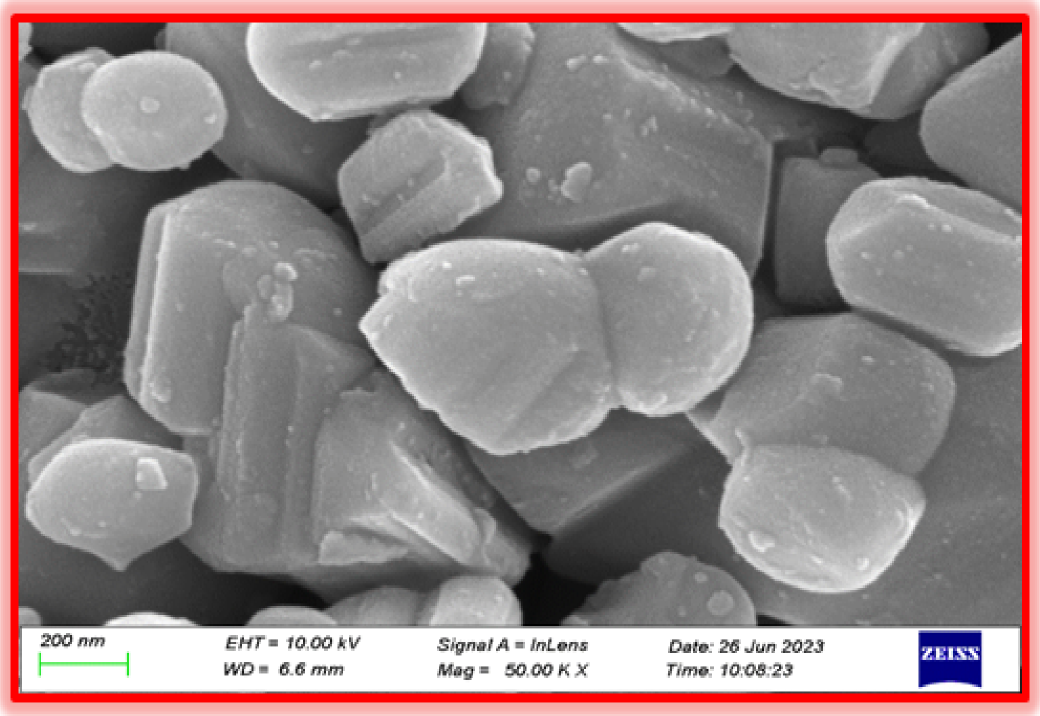

Figure 5.6: SEM image of (BSNN:xH): for x= 0.00 % $Ho^{3+}$ of (2oo nm) dimension.

Moreover, SEM images obtained show the detail morphology and microstructures of the samples (figure 5.6). SEM scanning was also performed from 5 $\mu$m to 500 nm at 2000 to 20,000x magnification to see all detail surfaces microstructures showing the different morphologies. An obtained SEM image result again showed that the surface morphology of the particle distributions was random but with nearly homogeneous size-distributions with different particles size and agglomerate. With large dimensions in zoomed images, we saw more clearly various shapes, sizes & sizes distribution of the particles. Again it was observed that the surface is less porous as proved by SEM images. In other side these confirmed that it is an ideal and promising for various optoelectronic properties such as better absorption as a result of more charge carriers being densely distributed on the surface (see figure 5. 7).

The top-to-bottom arranged surface microstructures of three different dimensions (2$\mu$m, 1 $\mu$m and 500 nm) for x=0.00 at left and for x=0.05 at the right are shown in Figure 5.7. The images display nearly homogeneous distribution of agglomerate particles in the composite, where the zoomed image clearly indicated that the particles only have difference in shape, size and size distribution.

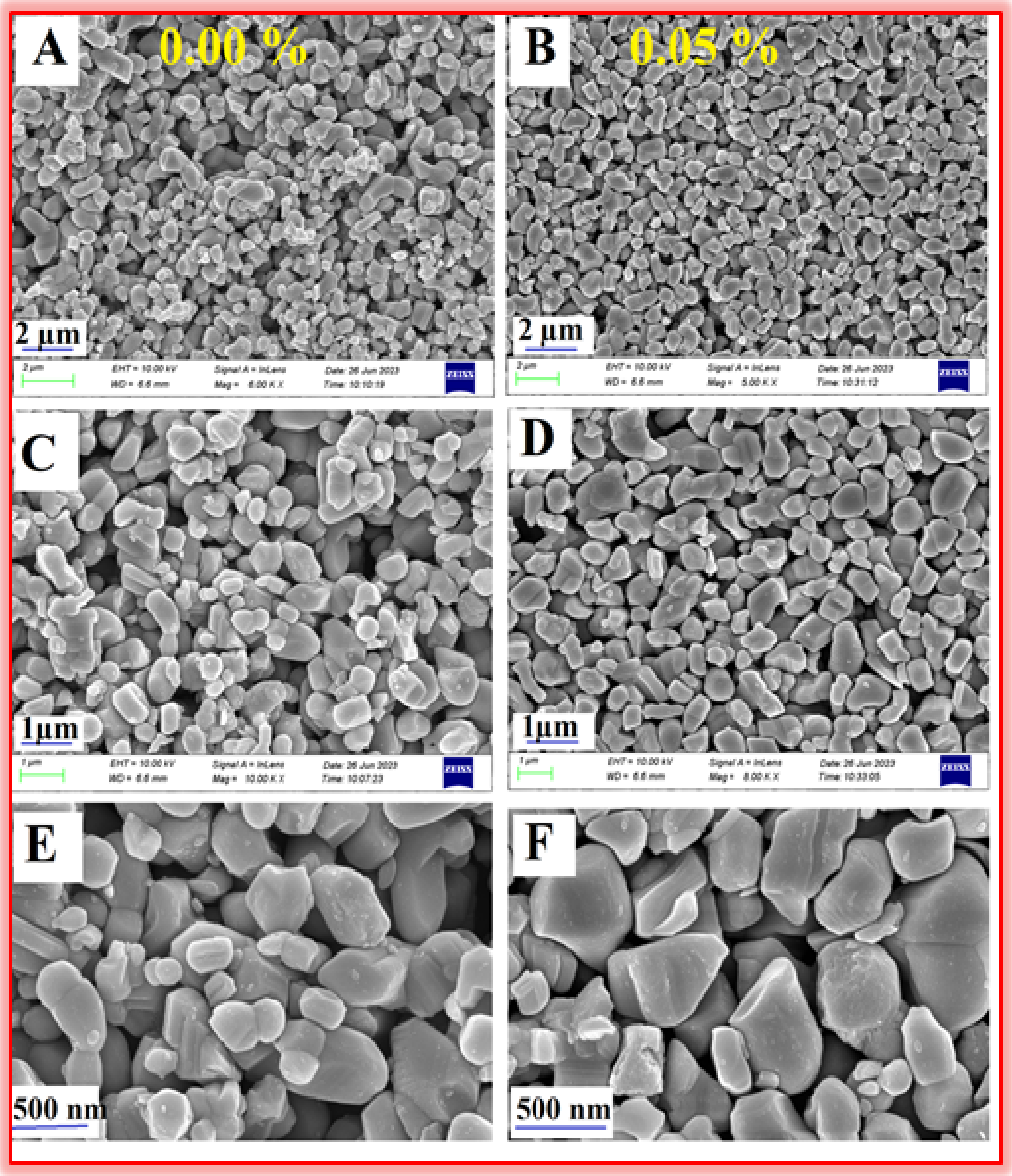

Figure 5.7: SEM Image of BSNN: xH ; A, C and E for x = 0.00 % $Ho^{3+}$ in the left and B ,D and F for x = 0.05 % $Ho^{3+}$ in the right for 2$\mu$m, 1$\mu$ m and 500nm dimensions top down respectively.

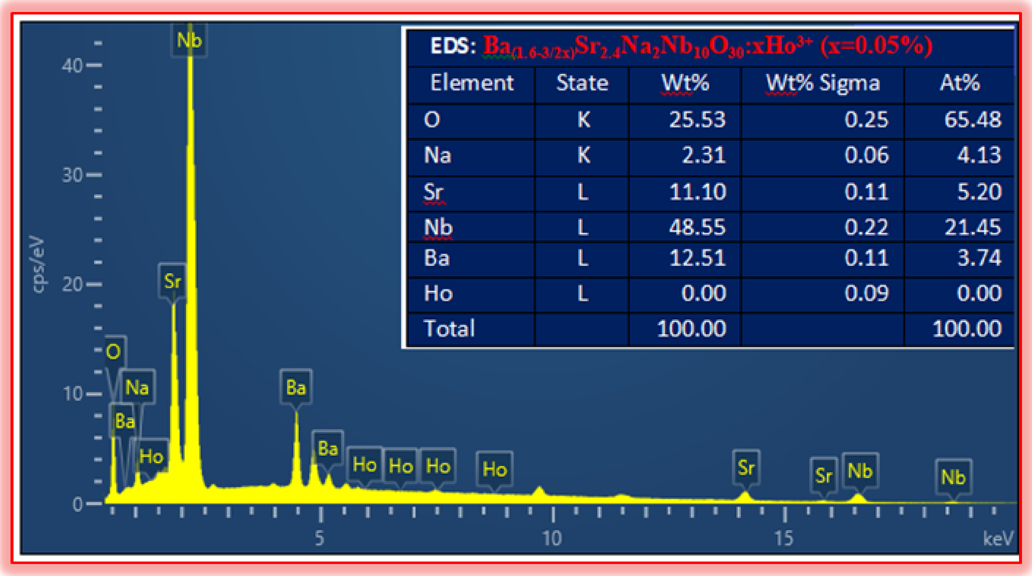

EDS: $Ba_{(1.6-3/2x)}Sr_{2.4}Na_2Nb_{10}O_{30}:xHo^{3+}$ (x=0.05%)

| Element | State | Wt% | Wt% Sigma | At% |
|---|---|---|---|---|
| O | K | 25.53 | 0.25 | 65.48 |
| Na | K | 2.31 | 0.06 | 4.13 |
| Sr | L | 11.10 | 0.11 | 5.20 |
| Nb | L | 48.55 | 0.22 | 21.45 |
| Ba | L | 12.51 | 0.11 | 3.74 |
| Ho | L | 0.00 | 0.09 | 0.00 |
| Total | | 100.00 | | 100.00 |

Figure 5.8: EDX Maping of BSNN: xH: For x= 0.05 % $Ho^{3+}$.

### 5.3.4 Energy Dispersive X-Ray Spectroscopy (EDX)

(EDX) was implemented to measure composition and mapping of as prepared powder samples elements. It is known that the EDX is a complementary and high standard method to determine and quantify the elemental constitutes of a sample surface ranging a few nanometers to micrometers. It was also applied to differentiate all the constituents and quantified them. EDX spectra also confirm the standard stoichiometric composition of the BSNN: xH nanocomposite system which was used in the analysis as shown in Figure 5.8 in set.

The presence of additive ions ($Ho^{3+}$) in EDX spectrum was clearly observed and has been significantly quantified by numerical values. As we expected, no emissions other than Barium, Strontium, Sodium, Niobium and Oxygen were observed in BSNN: xH nanocomposite (figure 5.8). The presence of these Ba, Sr, Na, Nb, O and Ho, strong patterns peaks, which in turn assure BSNN: xH tetragonal tungsten bronze structure nanomaterial was formed and it was consistent with XRD results.

Figure 5.9 also shows and confirms that all components are found in the desired amounts accordingly with the normal stoichiometric equation. Besides, it was as-

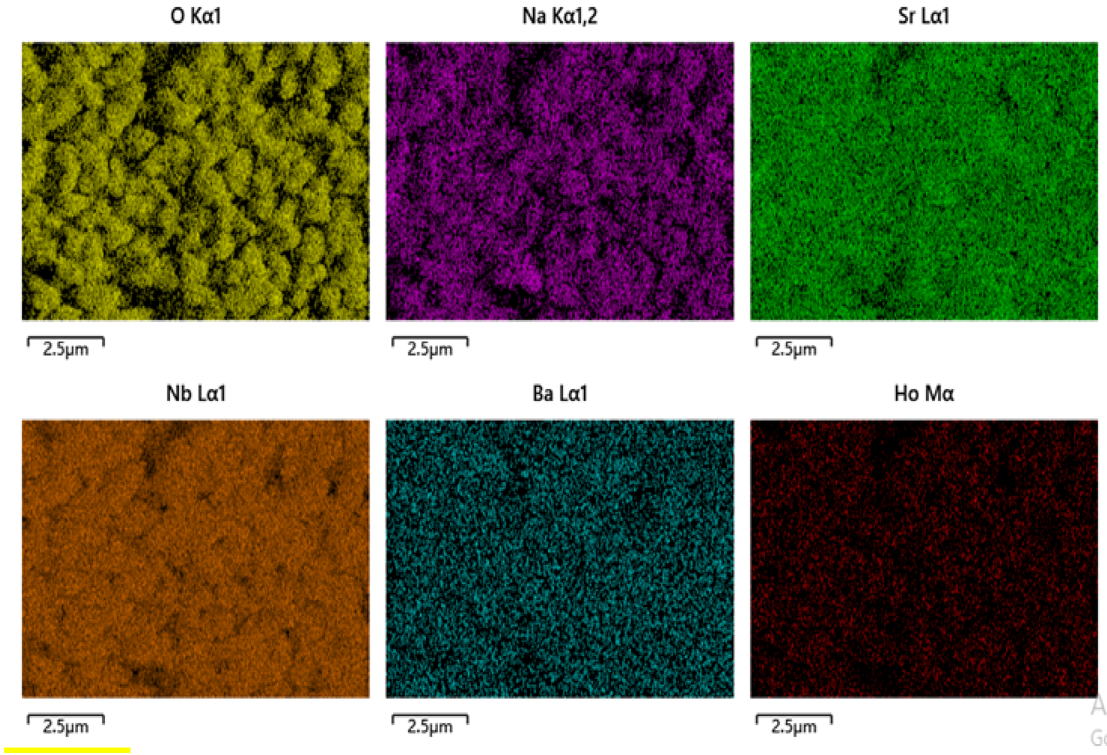

Figure 5.9: EDX Maping of (BSNN: xH): X = 0.05 % $Ho^{3+}$ (Map sum Specrum).

sured that no additional impurities included in the process of sample preparation. EDX layered image has confirmed that the nanocomposite materials contain all components. The proportional distribution of particles in the sample containing only the designed quantity showed also another way of validating the quality of synthesis methods. Figure 5.10 is the (EDX) result of the prepared BSNN: xH nanocomposite for 0.05 % $Ho^{3+}$ including molecular and atomic weight percentage. The outcomes still confirmed that the experimental results of (Wt %) and (At %) of each element were consistent with the calculated ones which was obtained using the standard stoichiometric equations (see Figure 5.10). This again proved that advanced measuring equipment; the EDX and the electronic scale (digital) were used after fine calibration. The experimental results confirmed also in performing an experiment carbonates and oxides burned out completely in a furnace at 1100 $^0$C during the 4 hours solid state reaction process.

Figure 5.10 also shows the comparative analysis of the experimentally obtained

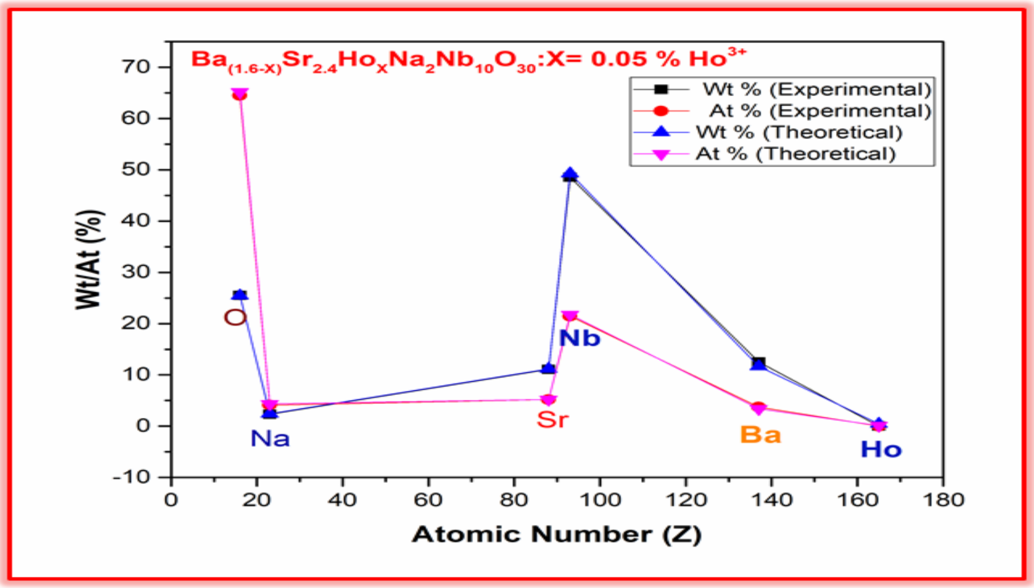

Figure 5.10: EDS Maping of Barium Strontium Sodium Niobium Oxygen and Holmium (BSNN: xH): For x= 0.05 % $Ho^{3+}$ Wt/At % , (Map sum Specrum).

results of the samples with the theoretically calculated results. On the other side, all five elements and additive ion are separately identified by various colors. Moreover, it was checked and assured the required and desired elements obtained without any inclusion of defects. This is another way to ensure that we have added an optimum and selective amount of holmium ion to the system.

### 5.3.5 Fourier Transfor Infrared Spectroscopy (FTIR)

For detection of organic to inorganic substances FT-IR has been widely used. (FT-IR) is also an important characteristic technique for identifying the components of a material and analyzing the existing bonds and functional groups of the nanomaterial. Figure 5.11 presentation of the comparative analysis of the FT-IR results of the as prepared samples. It clearly showed the effect of defects which has a significant impact on the nanocomposite materials. It has also displayed the existence of expected frequencies range for the pure or doped barium-strontium sodium niobate without and with impurity respectively. FT-IR spectra of the samples calcined at 1,100 $^0$C (Figure 5.11) indicated all metal - oxygen vibrational

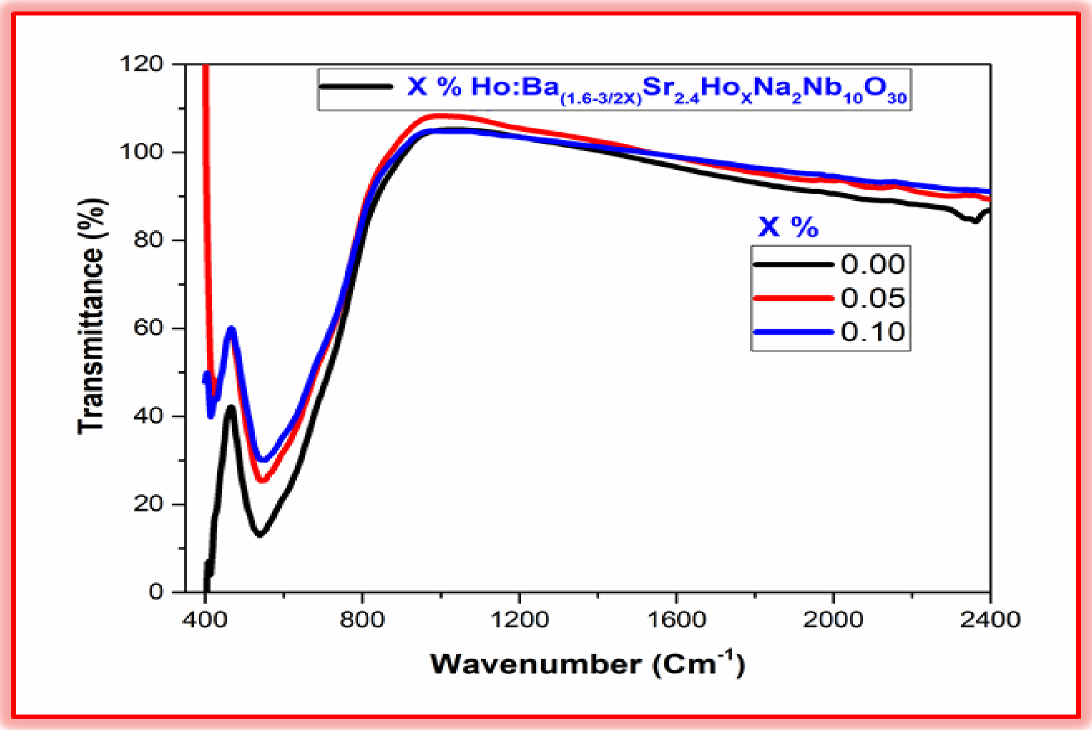

Figure 5.11: FT-IR Spectra of BSNN: xH: A=0.00 , B=0.05 % $Ho^{3+}$. C=0.10 % $Ho^{3+}$.

mode at a wave number 540.60 cm$^{-1}$ with no impurities. But at 429.92 for (0.05) and 415.77 for (0.10) cm$^{-1}$ there were new wavenumber that varies slightly with ions concentration, t his may be due to the variation in ionic radii of barium to barium-substituted holmium ions since they have additional peaks indicating presence of Ho-O, vibrational modes of the band. At x = 0.00, the FT-IR result shows only one metal-oxygen bond vibrational stretching peak, and at x = 0.05, 0.10%, it showed additional intense peaks with increasing impurity concentration at different (A1, A2) sites.

The scanned FT-IR results ensure that the pure (x= 0.00) Spectra of BSNN: xH without additive at 1,100$^0$C and powders doped with holmium ions, as seen in (Figure 5.9), are in nice agreement with the literature values [125] i.e., FT-IR result in Fig. 8 also showed that the two-frequency vibration and stretching $\upsilon 1$ (500-600 cm$^{-1}$), $\upsilon 2$ (400-450) cm$^{-1}$ for A1 and A2 sites ions. All samples with different doping concentrations showed consistent FT-IR results, except that strong peaks occurred at larger amount of doping. Figure 5.9 analyses of all the synthesized samples without and with additives ions for comparison using single plot to show the difference clearly. The image showed that the necessary components of the elements containing the metal-oxygen bond vibration at two frequencies were identified as expected. Addition of a significant and varying amount of additives slightly altered bond elongation.

### 5.3.6 Photoluminescence (PL)

When the single ion doped BSNN: xH TTBs ferroelectric nanomaterials admitted to excite at 285 nm, the spectra of emission was obtained at 572 nm wavelength due to the radiative emission transition from F orbital to the various H orbitals. Particularly the emission peaks at 572 nm (yellow) is ascribed to $4F_{9/2} \rightarrow 6H_{13/2}$ transitions. This is also ascribed to the electric dipole transitions [164, 165].

The second prominent emission band at 531 nm excited at 265 nm and matching to bright green arising from $5D_4 \rightarrow 7F_5$ transitions confirming the high probability of electric dipole transition. The other most prominent emission band at 686 nm (red) excited at 285 nm is also ascribed to $4f \rightarrow 4f$ transitions from $5D_4 \rightarrow 7F_3$. (Fig.11) [125].

Comparative emission spectra for $Ho^{3+}$ doped intensities of 0.00% and 0.03% are displayed in Figure 5.12. These intensities were stimulated at 265 nm and 285 nm and 305 nm and 325 nm. In both instances, the intensities are measured at the same wavelength for 0.00% and 0.03% without shift. These studies also showed that when the dopant concentration changes from 0.00% to 0.03%, the intensities for two pair wavelengths of excitation double. Dopants have a major impact on system intensities that can be adjusted. The maximum intensity (322.8 a.u.) was noted at 285 nm when 0.03% $Ho^{3+}$ was used as the excitation wavelength. This optimal photoluminescence property intensity, in turn, is a sign of a prospective polarization that would improve the system's ferroelectric property. Selecting the appropriate excitation wavelength is essential for examining the luminescence characteristics of rare earth ion amalgamated oxide. The spectra shown in Figure 12 exhibit emis-

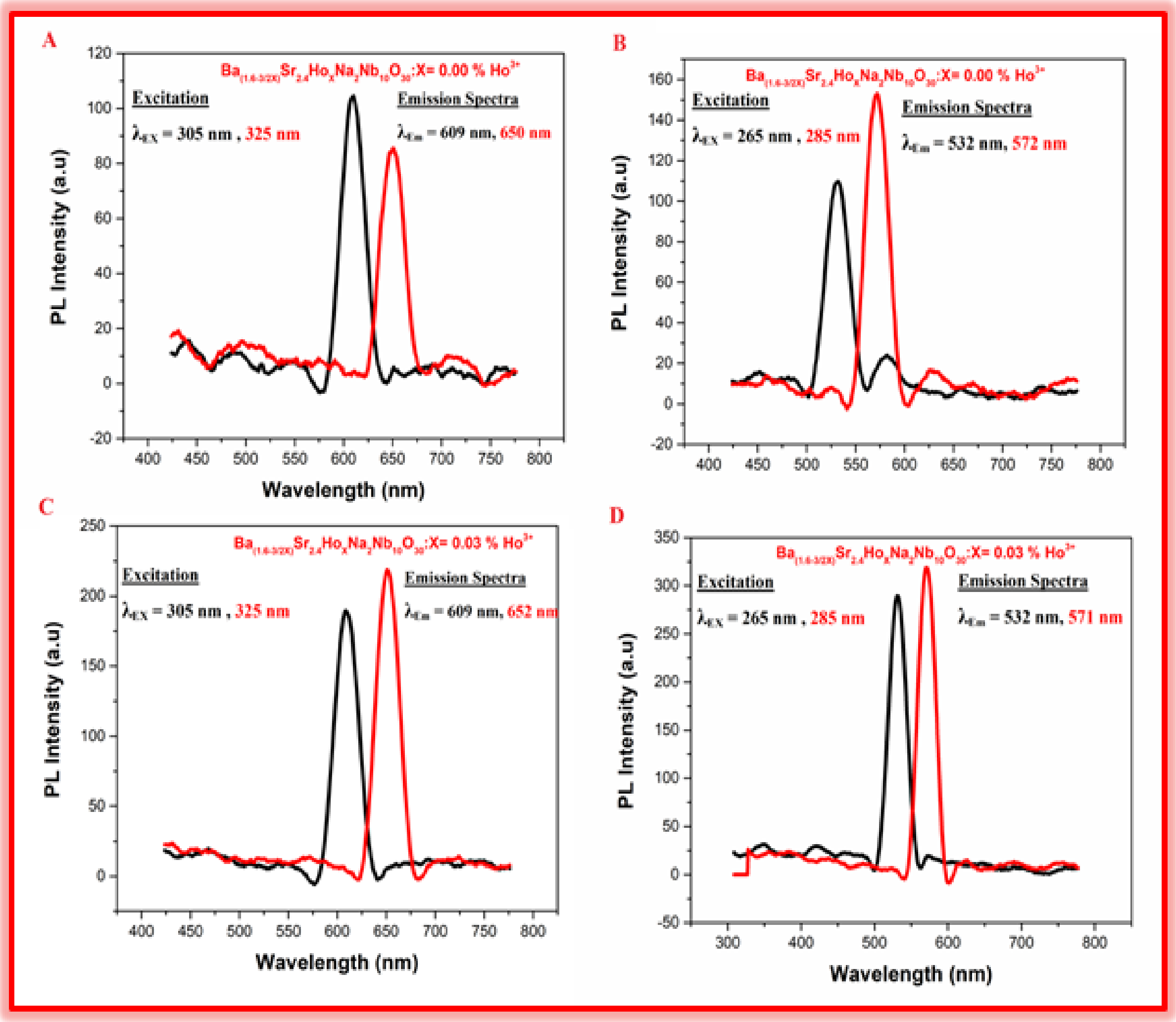

Figure 5.12: Photoluminescence spectra of 0.03 % $Ho^{3+}$ doped BSNN: xH excited from 265 nm to 325 nm wavelength ranges.

sion, with the highest intensity at x=0.03% $Ho^{3+}$ content with a sharp red shift, culminating at 572 nm attributed to the $4F_{9/2} \rightarrow 6H_{13/2}$ (yellow) transition and at 652 nm accounted to the $4F_{9/2} \rightarrow 6H_{11/2}$ (red) transition. According to the $\Delta L = 2$, $\Delta J = 2$ golden rules, the yellow emission, attributed to the $4F_{9/2} \rightarrow 6H_{13/2}$ transition, is a forced electric dipole (ED) transition. It was discovered that this transition is hypersensitive and that the immediate environment typically influences it [166, 167]. Additionally, the discussion included the relationship between the $Ho^{3+}$ doping content and emission hierarchy. The intensity of the light emission appears to increase as the fraction of $Ho^{3+}$ ions increases up to 0.3 mol % and diminishes at 0.5 mol %. The observed decrement is ascribed to the quenching with dopant contents via resonant energy transfer (RET) between $Ho^{3+}$ - $Ho^{3+}$ ions, thus clarifying self-quenching phenomenon and cross relaxation mechanism [168]. The strong green emission band at 531 nm, which originates from $5D_4 \rightarrow 7F_5$ transitions, is the second conspicuous emission band that is excited at 265 nm, suggesting a high likelihood of an electric dipole transition. There is also an explanation for the other most noticeable emission band at 686 nm (red) stimulated at 285 nm: $4f \rightarrow 4f$ transitions from $5D_4 \rightarrow 7F_3$. (Figure 5.13) [169].

The pure (or undoped) ferroelectrics nanomaterials have shown also a good photoluminescence property. Meanwhile by adding dopants the emission spectra has been enhanced in intensity and also make a shift towards red, particularly for the concentration of 0.03 which was excited at 285 nm wavelength clearly observed as shown in (figure 5. 13).

The excitation at (285nm) given in Figure 5.13 has maximum emission intensity (322.8 a.u) for the sample which has 0.03 % $Ho^{3+}$ concentration. In relative comparison the emission spectrum that was excited at 305 nm wavelength has the least intensity (190 a.u).

The effects of the holmium ion concentrations were also clearly observed with significant change in both absorption and PL intensities. The previous results of Uv-vis displays highest intensity at 205 nm near (UV) for the concentration of 0.03 %, it was also consistent with the highest intensity obtained at 686 nm from PL spectra

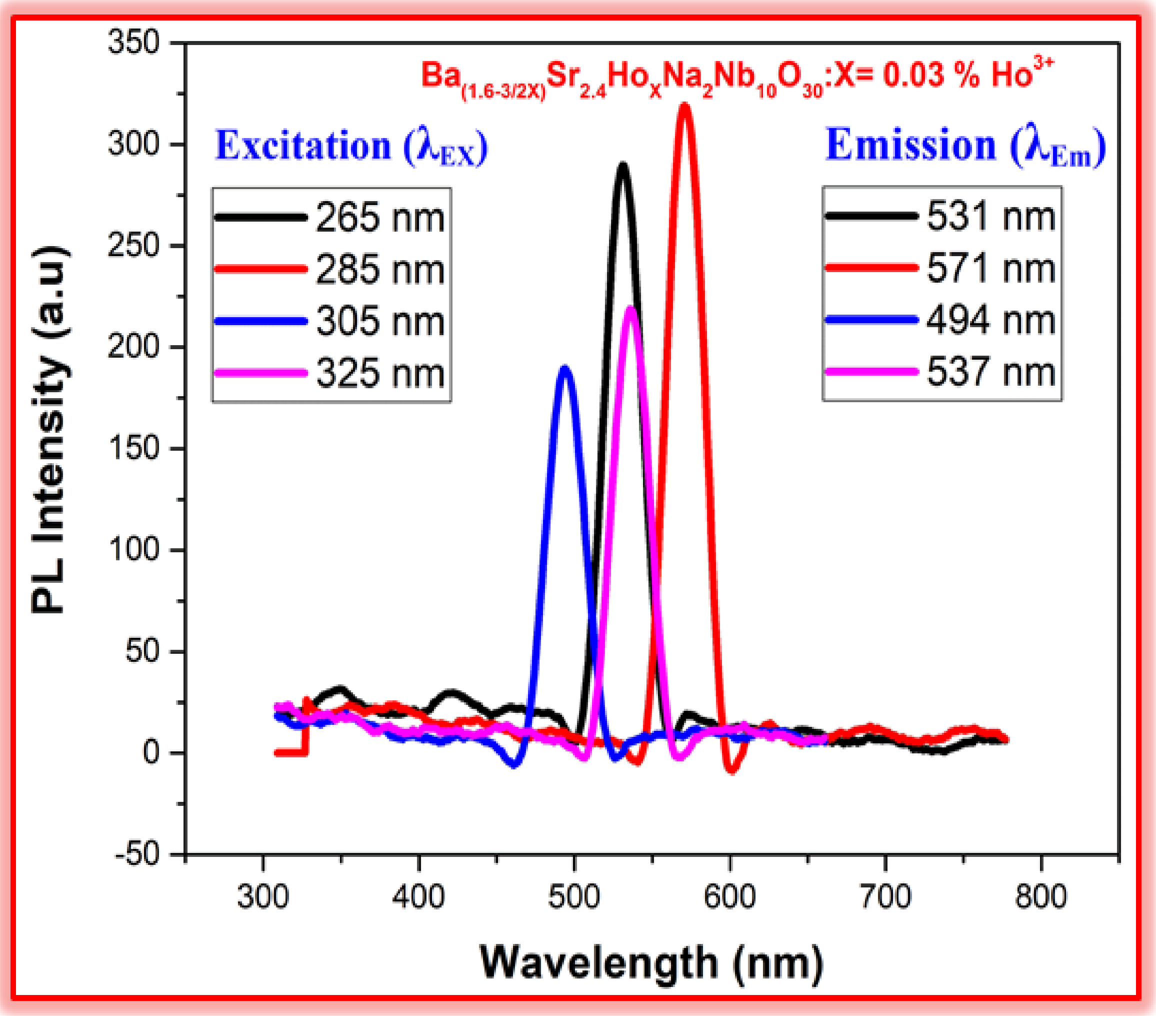

Figure 5.13: Photoluminescence spectra of 0.03 % $Ho^{3+}$ doped BSNN: xH excited from 265 nm to 325 nm wavelength ranges.

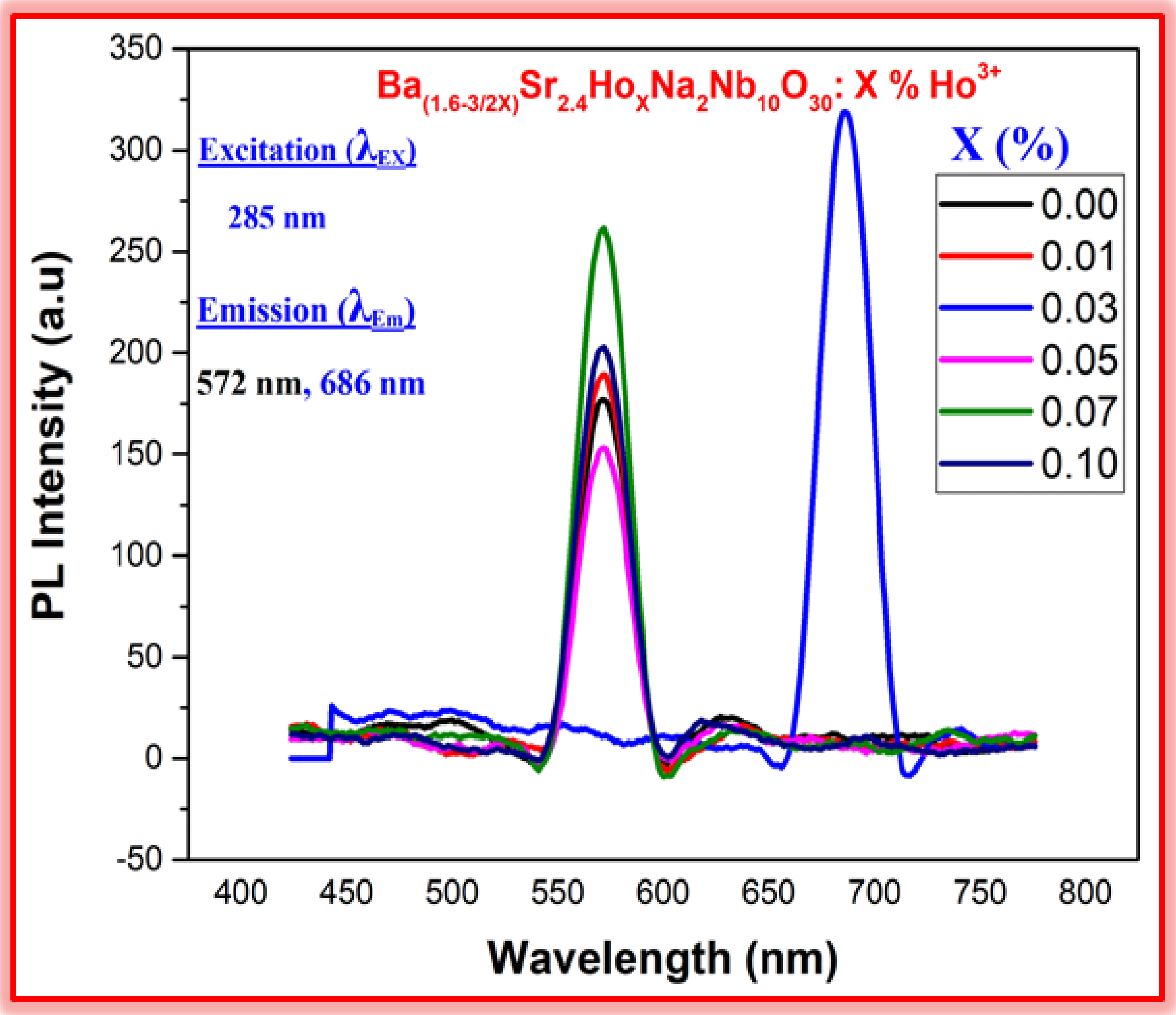

Figure 5.14: Photoluminescence spectra of 0.00 - 0.10 %$Ho^{3+}$ doped BSNN: xH excited 285 nm wavelengths..

for the same concentration value of 0.03 % $Ho^{3+}$. Figure 5.14 displays photoluminescence spectra of different concentration which was excited at wavelength of 285 nm. It shows almost the same wavelength of 572 nm for all concentrations except for x = 0.03 that has unique spectra that centered at wavelength of 686 nm with red shift. As we vary the concentrations from 0.00 to 0.03 their intensity increases in different scale. But for keeping increases from 0.03 to 0.05 it decreases, then it tends to increase for 0.07 finally it decreases as we still increase to 0.10 %. (See Figure 5.14)

## 5.4 Conclusion

The Tetragonal Tungsten Bronze structure was identified from the XRD result of the (BSNN: xH) ferroelectric nanomaterial prepared through the conventional solid-state reaction methods. The results of UV-Vis analysis showed that a good absorbance was occurred at 205 nm for a concentration of 0.03 $Ho^{3+}$. In addition, it showed that for the pure ferroelectric phase (x = 0.00 % $Ho^{3+}$), no absorption is observed. Again at a relatively excessive amount of dopant (x = 0.10 $Ho^{3+}$) there is no absorption. On the other hand, the EDX result with visible mapping, confirmed that all the elements that made up the compound were found in good ratio with standard stoichiometric proportions. Both pure and doped ferroelectric nanomaterials showed sharp and smooth photoluminescence peaks for various excitation wavelengths ranging from 265 nm - 325 nm. An intense PL spectra having a highest intensity of (322.8 a.u) for x=0.03 $Ho^{3+}$ was obtained at the excitation wavelength of 285 nm with its emission spectra centered at 686 nm. In increasing of the concentration from the reference x = 0.00 $Ho^{3+}$ to 0.03 $Ho^{3+}$, the PL experiment showed an increasing intensity with a unique red shift obtained for the concentration of 0.03 $Ho^{3+}$ with emission spectra of 686 nm that was excited at 285 nm. The experiment also revealed a significant effect of the holmium ion dopant optimum value which appeared at a specific point (0.03 $Ho^{3+}$) uniquely in relation to lower and higher dopant concentrations. Moreover, the results indicated that the synthesized nanomaterial is highly promising for optoelectronic applications inline to the characterized parameters values.

# 6

# Green Synthesis of Niobium doped Calcium Magnesium Silicate Phosphor Using Stenotaphrum Secundatum Grass Extract

## 6.1 Introduction

Currently, inorganic phosphor materials have drawn out a lot of attention because of their multiple applications, for instance, in cathode-ray tubes, photodiodes, lamps, and x-ray detectors, bio-detectors, color display, radiation dosimetry and dye removal [43-47]. Among the inorganic phosphor materials, silicate based became a lot of attention drawn materials for wide and multi-dimensional practical applications due to their unique features such as visible light transparency, good chemical resistance, high temperature strength, low thermal expansion, excellent conductivity, well known chemical and thermal stability, low cost and easy preparation [48, 49].

Calcium magnesium silicate (CMS) phosphor, with chemical formula ($Ca_2MgSi_2O_7 : xNb^{5+}$), has recently drawn too much interest due to its unique structure features with an extraordinary physical and chemical stability. It has been also extensively discussed in biological and medical areas of application [44]. Silicate with akermanite structure is becoming a possible and attractive bio-ceramics for tissue engineering applications [45, 95]. For instance akermanite calcium magnesium silicate has an extraordinary biocompatibity and excellent bioactivity properties. By now it is becoming a promising bio-ceramic bone tissue engineering materials in medical applications or a probable bone material [48, 96].

In the synthesis of silicate based phosphor materials, tetraethyl-orthosilicate (TEOS) is a primary precursor. Due to its high scarcity in most developing countries and difficulty to import it as well make the challenge magnified. This has been also a bottleneck for the growth of researches focusing on silicate based inorganic phosphor materials in such countries. Therefore, a new mechanism should be designed to alleviate this problem [58, 59]. Stenotaphrum secundatum grass is reported to be reach in silica [60] and it is widely available in almost all countries in the world. However, whether the extract of this grass can be used as a precursor for the synthesis of silicate based inorganic phosphors instead of TEOS is not really examined. The use of Stenotaphrum secundatum grass extract instead of TEOS has a double advantage in that it is also environmentally friendly.

In the synthesis of silicate based phosphor materials, tetraethyl-orthosilicate (TEOS) is a primary precursor. Due to its high scarcity in most developing countries and difficulty to import it as well make the challenge magnified. This has been also a bottleneck for the growth of researches focusing on silicate based inorganic phosphor materials in such countries. Therefore, a new mechanism should be designed to alleviate this problem [58, 59]. Stenotaphrum secundatum grass is reported to be reach in silica [60] and it is widely available in almost all countries in the world. However, whether the extract of this grass can be used as a precursor for the synthesis of silicate based inorganic phosphors instead of TEOS is not really examined. The use of Stenotaphrum secundatum grass extract instead of TEOS has a double advantage in that it is also environmentally friendly. In our present work, we reported the synthesis and characterization of niobium ion doped calcium magnesium silicate phosphor prepared via sol-gel methods. The structural analysis, optical properties, surface morphology and elemental mapping were studied by characterization of x-ray diffractometer, UV-Visible spectrometer, photoluminescence fluorescence spectrophotometer, scanning electron microscope and energy dispersive x-ray spectroscopy analysis, respectively. The different symmetric and asymmetric stretching and vibrational and bending peaks modes were analyzed using

Fourier transform infrared spectroscopy.

## 6.2 Experiment

### 6.2.1 Synthesis

Stenotaphrum secundatum grass was obtained and chopped in to pieces. The grass sample was dried for about one month. The dried sample was then converted to fine powder by grinding mortar and pestle which was precleared with deionized water and ethanol. The fine powder was then added to ten ml of de-ionized water and maintained under magnetic stirring for 30 minutes. Finally the solution was filtered using filter paper and the final stenotaphrum secundatum grass extract was stored. Niobium doped Calcium magnesium silicate $(Ca_2MgSi_2O_7 : xNb^{5+})$ was then synthesized via sol-gel route using calcium carbonate $(CaCo_3)$, Magnesim carbonate $(MgCo_3)$ and Stenotaphrum secundatum grass extract as a starting materials according to their stoichiometric ratio for various amounts of x (x = 0.2, 0.4, 0.6 and 1.0 % $Nb^{5+}$)) Some amount of the powder samples (0.2, 1.0 % $Nb^{5+}$) were grinned thoroughly for 2 hrs using $C155$ mortar and pestle (Diameter 100 mm, TNB 6EL, England) and the other kept as bulk sample for comparison. The milled sample was put in an alumina crucible and subsequently fired at 500 $^0C$ for one hour. Finally, pure white powder was obtained after cooling down the programmable furnace.

**The chemical reaction of the process is given as follows:**

$8CaCO_3+4MgCO_3+8SiO_2*H_2O+2Nb_2O_54Ca_{(2-x)}MgNbxSi_2O_7+12CO_2(\uparrow)+8H_2O(\uparrow) + 5O_2(\uparrow)$

### 6.2.2 Characterization

The XRD pattern has been obtained from DRAWELL (XRD-7000 Model: x-ray powder diffractometer using $Cu-K\alpha$ radiation $(\lambda = 1.5406\mathring{A})$ at 30 KV, 25 mA and the data were collected over the range of (2$\theta$ = 10 to $80^0$). FTIR spectra were recorded with the help of Agilent Technologies: Agilent-MicronLa FTIR transmittance a2m

Spectroscopy for examining the functional group (4000 to 400 $cm^{-1}$) of phosphor by direct use of as- prepared powder sample. The emission and excitation spectra of the samples were measured by Cary Eclipse serial number My1849002 model fluorescence spectrophotometer with slits of emission and excitation lights of 10 nm and 600 nm per minute scanning rates. SEM/EDX (OXFORD INSTRUMENTS; The Business of Science) model was used to identify the surface morphology and examine the elemental mapping and composition of the prepared $(Ca_2MgSi_2O_7 : xNb^{5+})$ phosphor and UV-Vis (the powder was made to solution using di-methyl-sulfoxide (DMSO) solvent keeping the standard proportion of 85:15 solutes to solvent ratio and centrifuge) was used for UV-Vis spectroscopy analysis.

## 6.3 Results and discussion

### 6.3.1 XRD analysis

To identify the phase structure, powder XRD analysis has been carried out. The typical XRD patterns of our sample phosphors were shown in Figure 6.1. (a, b, c ,d). The XRD pattern of the diffraction peaks of the synthesized samples $(Ca_2MgSi_2O_7 : xNb^{5+})$ Phosphors were matched to the reported results and it was consistent with the standard XRD pattern reported by joint committee on powder diffraction standard (JCPDS) No 77-1149 [170] and (COD card No. 96-900-6941) [171].

Fig.6.1: (c, d) were zooming image of (a, b) patterns respectively to show exact position and shifts of the phosphors for different $Nb^{+5}$ dopants concentrations. Furthermore we observed the effects of dopants in the bulk and milled samples. The XRD pattern analysis shows that the position of peaks slightly shifts to a higher degree position (2Θ= 29.355 to 29.869 0) as the concentration of dopant, increase from 0.2 % to 0.4 %. However, no such slight shift was observed for the dopant concentration between 0.4 % and 1.0 %. This indicates that the effect of dopants concentration is dominant at low concentration of the dopants. The summary of the first top 3 positions of peaks and intensities is given in Table 6.1.

Using Debye Scherer formula for prominent peak at (211), the average crystallite

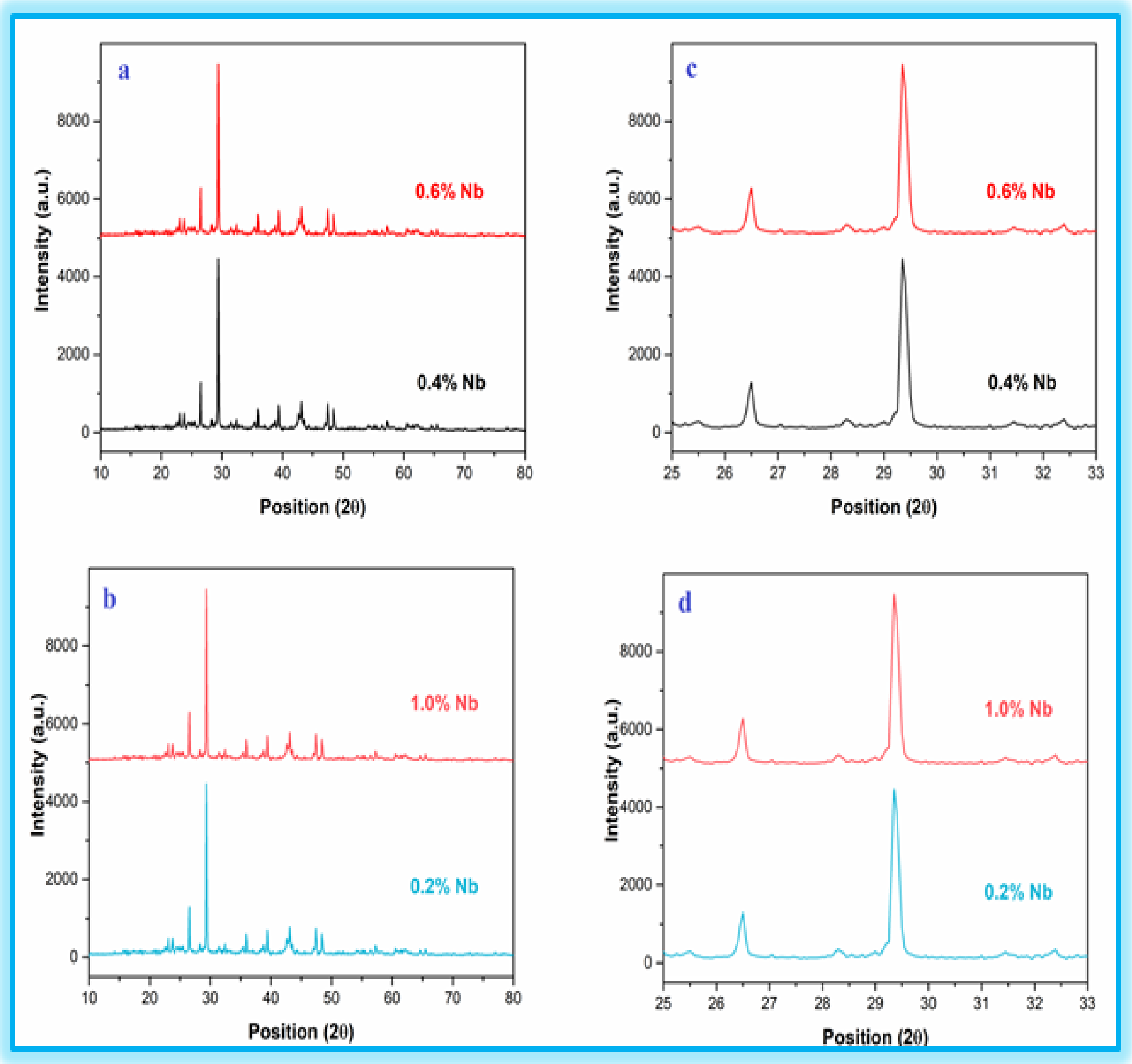

Figure 6.1: XRD pattern of Niobium doped Calcium Magnesium Silicate Phosphors: bulk (a, c), and milled (b, d).

size (D) of the $(Ca_2MgSi_2O_7 : xNb^{5+})$ phosphor was calculated as (186) nm. The formula is represented as follows:

$$D = \frac{\kappa\lambda}{\beta cos\Theta} \tag{6.1}$$

Where, $\kappa$ is the Debye-Scherer constant having value 0.94, $\lambda$ is wavelength of the incident x-ray ($\lambda$=1.5406 Å), $\beta$ = FWHM (Full Width Half Maximum) of the peaks and $\Theta$ corresponding to Braggs diffraction angle.

XRD pattern (Fig 6.1. a, b) of the powder calcined at a temperature of 500 $^0C$ confirms also the existence of akermanite $(Ca_2MgSi_2O_7)$ as the main phase, and merwinite $(Ca_2MgSi_2O_8)$( and diopside $(Ca_2MgSi_2O_6)$ as the secondary phases. With the increment of the calcination temperature the diopside phase completely disappeared and the intensity of the merwinite peaks reduced gradually. Finally it exists in tetragonal crystal system [171].

As shown in Figure 6.1. (a, b) and Table 1. For the bulk samples as concentration of dopant $(Nb^{5+})$ increases from 0.4 % at peak position of 29.80 0 to 0.6 % at 29.70 0, the intensity increases from 3354 to 3673 (a.u.). But for the milled one when the concentration of dopant vary from (0.2 %) at 29.65 0 to (1.0 %) at 29.35 0, the intensity decreases from 4859 (a.u) to 4464 (a.u). Therefore from our findings, there is significant effect of dopant concentration on the bulk and milled size samples.

### 6.3.2 Scanning electron microscopy (SEM)

We used SEM to examine the morphology of samples, since the luminescence characteristics of phosphor particles depend on the morphology of the particles such as size, shape, size distribution, and defects so on. The scanning of SEM was performed in the ranges of 1 to 10 micrometer dimension and 1000 to 10,000 times magnifications to see all aspects that demonstrate the morphology of $(Ca_2MgSi_2O_7 : xNb^{5+})$ phosphor. (See Fig. 6.2.) (a = 0.4, b = 0.6 % $(Nb^{5+})$ - bulk and C =0.2, d=1.0 % $(Nb^{5+})$ - milled). From the SEM image result, it was observed that the surface morphology of the particles distributions was not uniform

Table 6.1: XRD pattern of top 3 Peaks position (2 $\Theta$) and intensities with different dopant $(Nb^{5+})$ concentration of Calcium Magnesium silicate Phosphor.

| S.N | **Concentration of $(Nb^{5+})$ (%)** | **Position (2 $\Theta$) in (Deg.)** | **Intensity (a.u.)** | **Type** |
|---|---|---|---|---|
| 1 | 0.2 | 29.65 | 4859 | Milled |
| | | 26.80 | 1289 | |
| | | 43.10 | 785 | |
| | 1.0 | 29.35 | 4464 | Milled |
| | | 26.50 | 1288 | |
| | | 43.40 | 918 | |
| 2 | 0.4 | 29.80 | 3354 | Bulk |
| | | 26.90 | 1137 | |
| | | 47.90 | 683 | |
| | 0.6 | 29.70 | 3673 | Bulk |
| | | 26.80 | 911 | |
| | | 47.70 | 653 | |

and they were aggregated tightly with each other. Again from the SEM image, it was observed that as prepared samples consists of particles with different size distribution. For milled samples we found relatively uniform distribution of particles on the surface in comparison to bulk (see Fig. 6.2.). It also clearly observed that the surface is rough with different size and shape. At micro level the particles do not separated rather they are in mixed solid solution. Besides it was observed that, there were some large aggregates; it was present as a result of high temperature heat treatment.

SEM images at low magnification (See Fig. 6.2) clearly show significant high magnitude porosity in the bulk powder samples as compared to the grinned ones. When the magnifications become higher, the samples seem to have dense and flux microstructure surface morphology, but still having porosity with different relative density.

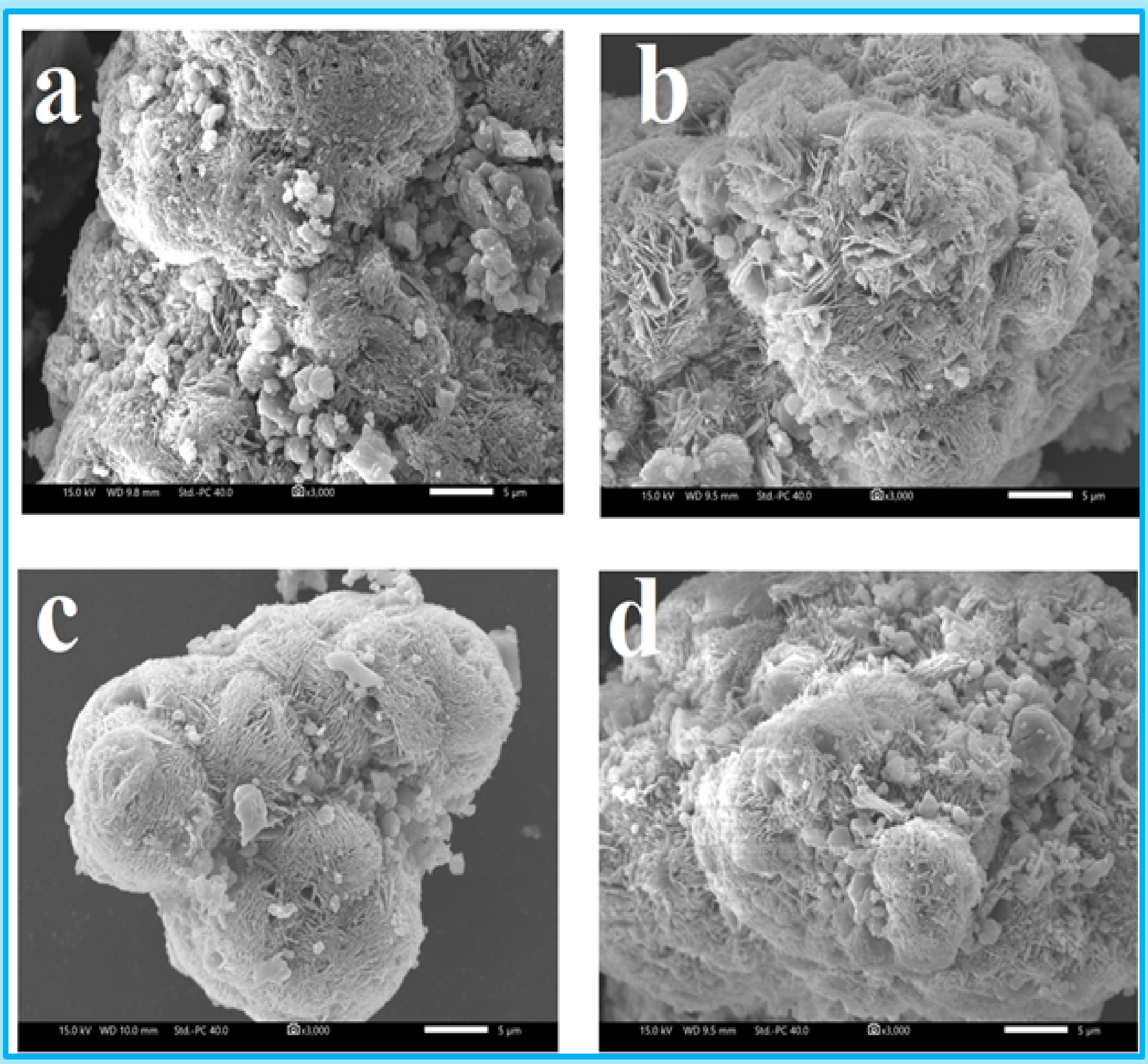

Figure 6.2: SEM Image of Niobium doped Calcium magnisium Silicate Phosphor : (a=0.4, b=0.6 % $(Nb^{5+})$ - bulk and C =0.2, d=1.0 % $(Nb^{5+})$ - milled).

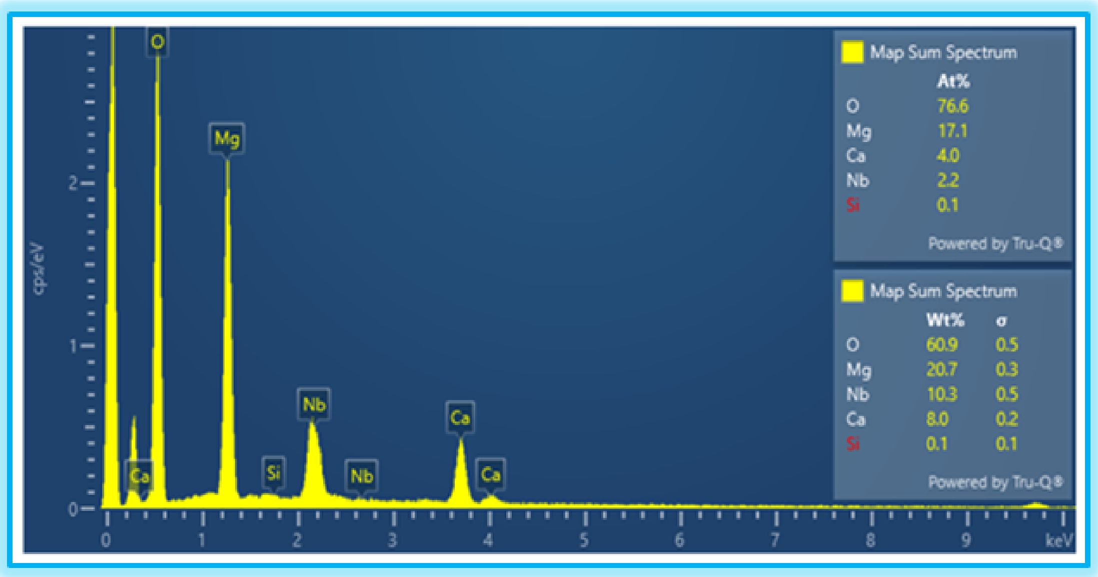

Map Sum Spectrum

| | At% |
|---|---|
| O | 76.6 |
| Mg | 17.1 |
| Ca | 4.0 |
| Nb | 2.2 |
| Si | 0.1 |

Powered by Tru-Q®

Map Sum Spectrum

| | Wt% | σ |
|---|---|---|
| O | 60.9 | 0.5 |
| Mg | 20.7 | 0.3 |
| Nb | 10.3 | 0.5 |
| Ca | 8.0 | 0.2 |
| Si | 0.1 | 0.1 |

Powered by Tru-Q®

Figure 6.3: EDX Spectra peaks of Niobium doped Calcium magnisium Silicate phosphor (Bulk).

### 6.3.3 Energy dispersive x-ray spectroscopy (EDX): Bulk CMS

The elemental composition and mapping of the powder samples were measured using energy dispersive x-ray spectroscopy (EDX). Since EDX spectroscopy is complementary and a standard procedures for determining and quantifying elemental composition of sample area as small as a few nanometers to micrometers, we used it to identify all constitute elements of the as-prepared samples. The existence of niobium or $(Nb^{5+})$ ion in the corresponding EDX mapping was clearly observed. As expected apart from calcium (Ca), Magnesium (Mg), silicon (Si), niobium (Nb) and oxygen (O) in $(Ca_2MgSi_2O_7 : xNb^{5+})$, there was no other emission observed in the EDX mapping of the phosphor (see Fig. 6.4). The existence of Ca, Mg, Si, O and Nb, intense peaks are present which preliminarily indicates the formation of $(Ca_2MgSi_2O_7 : xNb^{5+})$ phosphor as shown in (Fig.6.3).

The EDX Layered image confirms that all the components (calcium, magnesium,

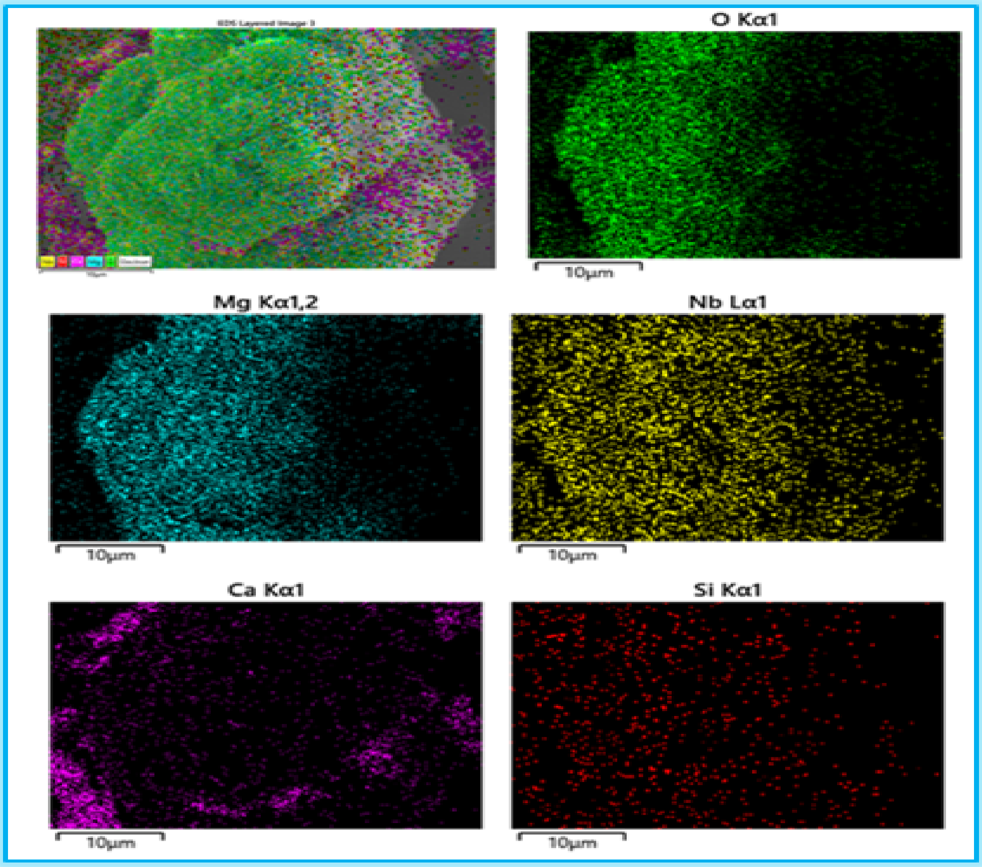

Figure 6.4: EDX Maping of Niobium doped Calcium magnisium Silicate phosphor (Map sum Specrum).

silicate, oxygen and dopant niobium) of the CMS are available in the phosphor. For the bulk system the EDX image shows the elemental compositions maps containing Ca, Mg, O, Si and Nb with different amount and proportion as expected. But very small amount of Si is found in the milled CMS, since it was used as catalyst for the solid state reaction in order to avoid sticking of particles with the container walls.

### 6.3.4 Energy dispersive x-ray spectroscopy (EDX): Milled CMS

For milled sample of Niobium doped Calcium Magnesium silicate phosphor, the silica components reduced and different composition in comparison to bulk was

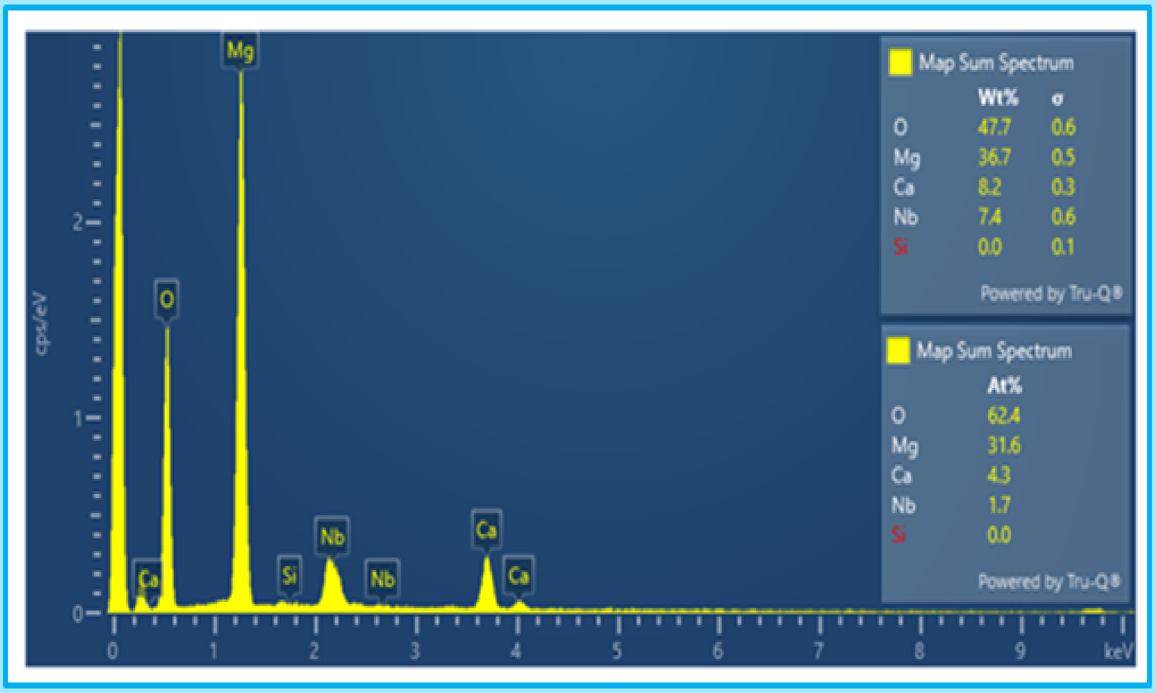

Map Sum Spectrum

| | Wt% | σ |
|---|---|---|
| O | 47.7 | 0.6 |
| Mg | 36.7 | 0.5 |
| Ca | 8.2 | 0.3 |
| Nb | 7.4 | 0.6 |
| Si | 0.0 | 0.1 |

Map Sum Spectrum

| | At% |
|---|---|
| O | 62.4 |
| Mg | 31.6 |
| Ca | 4.3 |
| Nb | 1.7 |
| Si | 0.0 |

Figure 6.5: EDX Map sum Spectra peaks of Niobium doped Calcium magnisium Silicate phosphor (Milled).

observed from the EDX layered images as expected since silica was used as catalyst for the reaction. The sum spectrum of the image shows different percentage amounts and weights of the elements.

### 6.3.5 Fourier transforms infrared Spectroscopy (FTIR)

The Fourier Transform Infra-Red Spectroscopy (FTIR) spectrum has been widely used for the identification of organic and inorganic compounds. The FTIR spectrum has been shown in (Fig. 6.7 A) grass extracted silicate (TEOS Substitute) and (Fig. 6.7 B) CMS: 1.0% $(Nb^{5+})$ phosphor. The FTIR spectra were recorded in the range of (4000 $cm^{-1}$ to 400 $cm^{-1}$) to obtain the figure print results. At 928.82 $cm^{-1}$ allocated a result of $(Si-O-Si)$ asymmetric stretch, 824.83 $cm^{-1}$ $(Si-O)$ symmetric

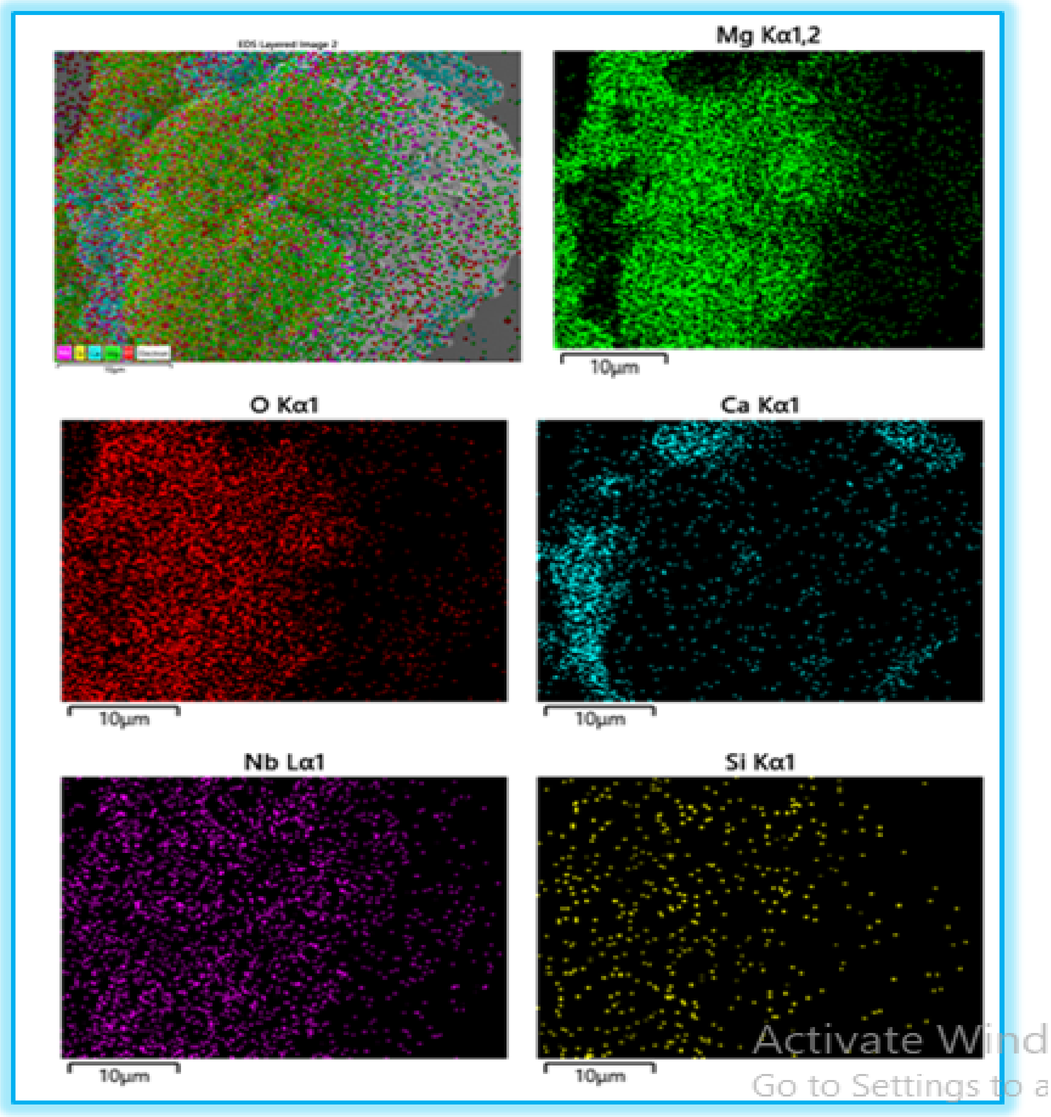

Figure 6.6: EDX Map sum Spectra peaks of Niobium doped Calcium magnisium Silicate phosphor (Milled).

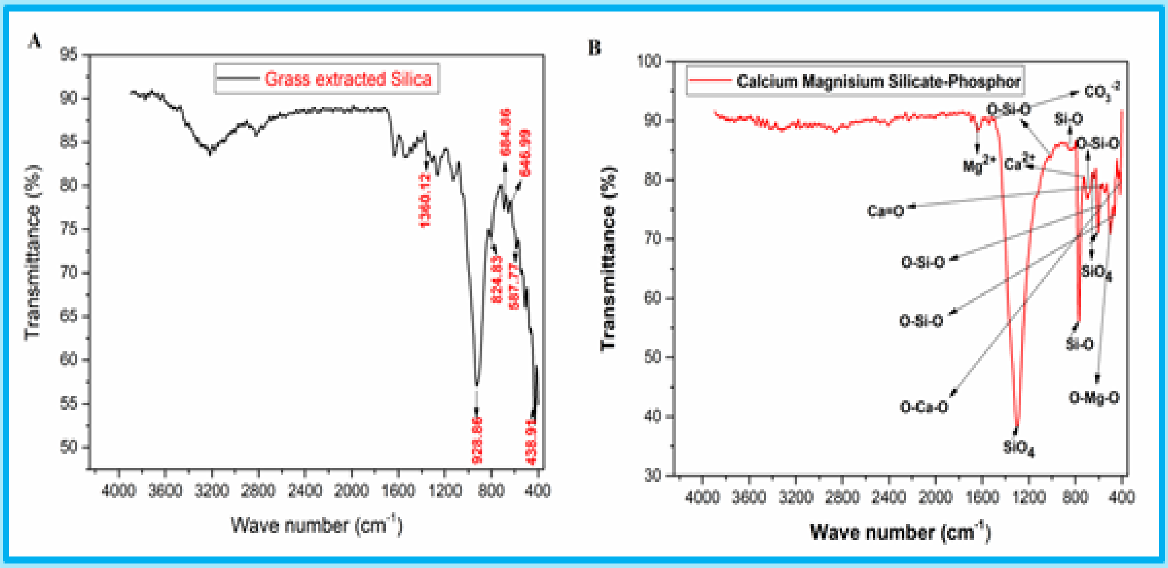

Figure 6.7: FTIR Spectra: A. (Green synthesized TEOS Substitute-Bulk), B. 1.0% Nb5+ doped Calcium Magnesium Silicate phosphor- -milled..

stretch, 587.77 $cm^{-1}$ and 438.91 cm-1 $(Si-O-Si)$ vibration mode and 1360.12 $cm^{-1}$, 68 6.81 $cm^{-1}$ and 646.91 $cm^{-1}$ allocated to existence of SiO4 group (see Fig. 6.7A). (Fig.6.7 B) show Calcium Magnesium Silicate phosphor;- At 842.92 $cm^{-1}$ allocated to $Si-O$ symmetric stretch, 586.52 and 482.82 $cm^{-1}$ were $Si-O-Si$ vibrational mode, 1300.61 $cm^{-1}$ $SiO_4$ group existence, 415.80 $cm^{-1}$ $O-Ca-O$ bending modes, 490.49 $cm^{-1}$ $O-Mg-O$ bending mode, 1024.89 $cm^{-1}$ symmetric stretching of $Si-O-Si$ , 1641.10 $cm^{-1}$ $Mg^{+2}$ vibrational bond, 1500 $cm^{-1}$ big vibration of carbonate and 737.90 $cm^{-1}$ $Ca^{+2}$ bending peak.

As concentrations of dopant vary from 0.2 % to 1.0 % the intensity became highly enhanced and slightly shifted to new position. This might be due to the shift in the wave number position following the variation in the dopant concentration. The FTIR spectrum of calcium magnesium silicate powders calcined at 500 $^0C$ in (Fig.6.7 B) is in a good agreement with what is reported in literature [171]. (Fig.6.7 A) Grass extracts FTIR spectra at bulk confirms the presence of TEOS substitute silica groups.

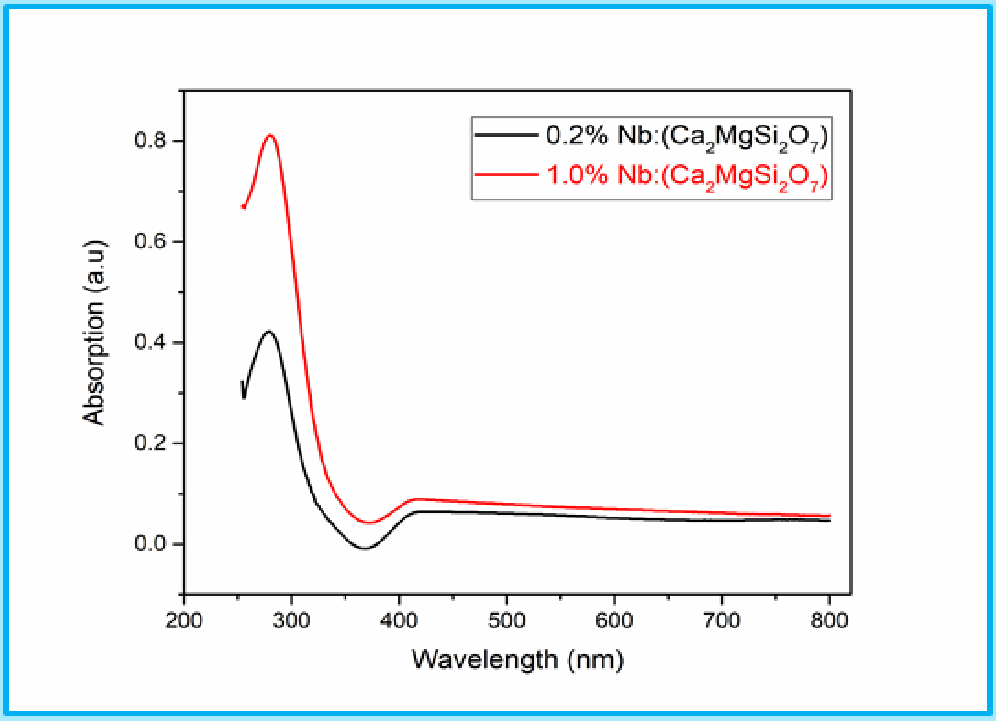

Figure 6.8: Shows UV-Vis absorption spectra of 0.2% and 1.0% $Nb^{5+}$: doped Calcium Magnesium Silicate phosphor.

### 6.3.6 UV-Visible Spectroscopy (UV-Vis)

Typical UV-Vis spectra of $(Ca_2MgSi_2O_7 : xNb^{5+})$ phosphor was shown by Fig.6.8. The result showed also the peak absorption occurs at wavelength of 280 nm for 1.0 % and at wavelength of 278 nm for 0.2 % that were excited at wavelength of 280 nm. From the results we observed that $Nb^{5+}$ doping has significant effects on the peaks intensity: when we vary the dopants concentration from 0.2 % to 1.0 % the intensity become doubled (See Fig.6.8).

### 6.3.7 Photoluminescence (PL)

We examine the excitation and emission spectra of milled 0.2 % and 1.0 % $Nb^{5+}$ doped $(Ca_2MgSi_2O_7)$ phosphor excited from 260 nm-360 nm wavelength ranges.

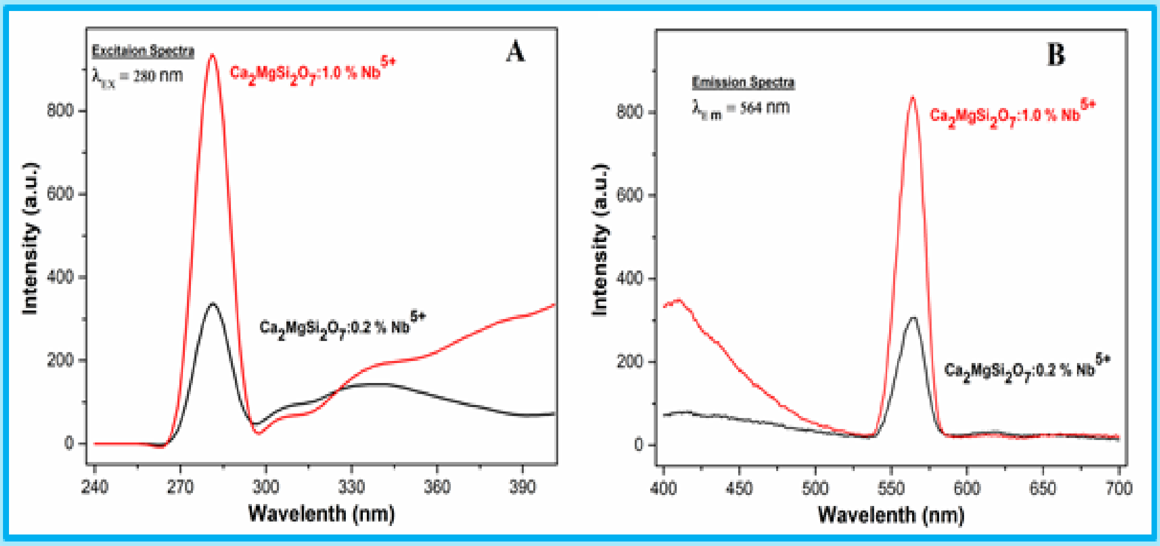

Figure 6.9: Photoluminescence spectra of 0.2% Nb5+ and 1.0% $Nb^{5+}$ doped Calcium Magnesium Silicate phosphor: (A = Excitation, B = Emission).

We obtained visible emission from blue to red region at different wavelength having various intensity (121 to 834) a.u. (See Fig. 6.9 (A, B). The excitation at (280 nm) spectrum of $(Ca_2MgSi_2O_7 : xNb^{5+})$ phosphor monitored at 564 nm emission given in Fig. 6.9 (B) has maximum emission intensity of 866 (a.u.). The spectrum of $(Ca_2MgSi_2O_7 : xNb^{5+})$ phosphor has also exhibited a broad band in the UV region centered at about 280 nm. For excitation at wavelength of (280 nm), as we increase the concentration of $Nb^{5+}$ from 0.2 % to 1.0 %, the emission intensity highly enhanced from (305 a.u. to 866 a.u.) See Fig.6.9 B. From the UV-Vis absorption and PL analysis, effects of the niobium ion dopant concentration were remains consistent in both analyses, since the previous results of Uv-vis i.e. as concentration of the dopant increases the intensity highly enhanced at the same wavelength of 280 nm for both absorption and excitation of Uv-Vis and PL results at the respective wavelength.

## 6.4 Conclusion

A novel luminescent phosphor of $(Ca_2MgSi_2O_7 : xNb^{5+})$ was successfully synthesized via sol gel methods using stenotaphrum secundatum grass extract as TEOS substitute and its optical properties were investigated. XRD pattern showed tetragonal akermanite crystal structure. FTIR confirms the existence of functional groups in the phosphor and it has also demonstrated stenotaphrum secundatum grass extract is a good source of silica. SEM image indicated the surface morphology is rough and aggregated having porous structure. The EDX spectra confirmed the existence of present elements in $(Ca_2MgSi_2O_7 : xNb^{5+})$ phosphor. The EDX results also revealed that there were relatively uniform distributions of particles in the system. The excitation spectra indicated the phosphor can be effectively excited by ultraviolet (UV) light, making it attractive as conversion phosphor for LED applications. The $(Ca_2MgSi_2O_7 : xNb^{5+})$ phosphor exhibits bright emission excited at wavelength of 280 nm. Photoluminescence measurements showed that the phosphor exhibited emission peak with good intensity (866 a.u.) at wavelength of 564 nm, corresponding to nearly green emission, indicating that it has favorable properties for application as near ultraviolet LED conversion phosphor. The concentration of niobium ion showed a significant effect on the intensity of absorptions and photoluminescence.

# 7

# Summary, Conclusion and Future Directions

## 7.1 Summary and Conclusion

With a broad goal of expanding the utilization of ferroelectric nanomaterials for device applications, this thesis focused on the synthesis of conventional tetragonal tungsten bronze structured ferroelectric nanomaterials through solid state reaction and their characterization. Various solid solutions based $(Ba_{(1.6-3/2X)}Sr_{2.4}Na_2Nb_{10}O_{30} : xHo^{3+})$ were synthesized and showed a tetragonal tungsten bronze structured phase. Testing procedures for the nanomaterials were developed to enable quantitative and quantitative determination of their morphology and compositional/mapping in addition to their UV-Vis and PL properties.

XRD analysis of Holmium doped Barium Strontium Sodium Niobate ferroelectrics nanomaterials revealed Tetragonal Tungsten Bronze structured nanomaterial successfully synthesized through conventional high temperature synthesis route. The identified crystal phase has an average crystallite size of 67.52 nm, having space group of p4bm and lattice parameters of a = 12.33 $\mathring{A}$, b = 12.33 $\mathring{A}$ and c = 3.93 $\mathring{A}$. The XRD pattern obtained showed also a best match with JCPDS card number-00-039-1453. Further analysis of XRD result indicated the highest intensity value (1845 a.u.) was obtained for the concentration of 0.05 % $Ho^{3+}$ ions. SEM and EDS analysis of surface morphology and elemental compositions of Holmium doped Barium Strontium Sodium Niobate ferroelectrics Tetragonal Tungsten Bronze structured nanomaterial showed clear and best quality surface morphology, microstructure and elemental mapping. The SEM images have also shown separate nanoparticles with different shapes, size and size distributions with random distributions. Moreover the micro level dimension showed relatively uniform distribution of particles and less porosity of the surface. The surface morphology is promising for enhancing optical properties of the system because of its homogeneous surface microstructure having dense nanoparticles distributions. The EDS results confirmed that all the constitute elements are found in correct proportion to the standard stoichiometric ratios. In addition it confirmed that there were no impurities added during the synthesis and characterization which in turn confirming high quality synthesis procedures were employed. The experimental and theoretical molecular weight and atomic percentage coincidence also indicating that the composites made in best quality and proportion synthesis approach. The FTIR analysis result indicated also the collective metal oxide single peak for the bond vibration at wave number of 540.60 $cm^{-1}$ as expected since in the finger print of FTIR values of metal oxides were commonly found 400 - 600 $cm^{-1}$ and the Holmium oxygen bond vibration modes at (0.05% $Ho^{3+}$), 415.77 (0.10 % $Ho^{3+}$) 429.92 $cm^{-1}$ which was not seen for the system without dopant.

The results of UV-Vis analysis showed that a good absorbance was occurred at 205 nm for a concentration of 0.03 $Ho^{3+}$). In addition, it showed that for the pure ferroelectric phase (x = 0.00 % $Ho^{3+}$)), no absorption is observed. Again at a relatively excessive amount of dopant (x = 0.10 $Ho^{3+}$)) there is no absorption. On the other hand, the EDX result with visible mapping, confirmed that all the elements that made up the compound were found in good ratio with standard stoichiometric proportions. Both pure and doped ferroelectric nanomaterials showed sharp and smooth photoluminescence peaks for various excitation wavelengths ranging from 265 nm - 325 nm. An intense PL spectra having a highest intensity of (322.8 a.u) for x=0.03 $Ho^{3+}$) was obtained at the excitation wavelength of 285 nm with its emission spectra centered at 686 nm. In increasing of the concentration from the reference x = 0.00 $Ho^{3+}$) to 0.03 $Ho^{3+}$), the PL experiment showed an increasing intensity with a unique red shift obtained for the concentration of 0.03 $Ho^{3+}$) with emission spectra of 686 nm that was excited at 285 nm. The experiment also revealed a significant effect of the holmium ion dopant optimum value which appeared at a specific point (0.03 $Ho^{3+}$)) uniquely in relation to lower and higher dopant concentrations. Moreover, the results indicated that the synthesized nanomaterial is highly promising for optoelectronic applications inline to the characterized parameters values.

A novel luminescent phosphor of $(Ca_2MgSi_2O_7 : xNb^{5+})$ was successfully synthesized via sol gel methods using stenotaphrum secundatum grass extract as TEOS substitute and its optical properties were investigated. XRD pattern showed tetragonal akermanite crystal structure. FTIR confirms the existence of functional groups in the phosphor and it has also demonstrated stenotaphrum secundatum grass extract is a good source of silica. SEM image indicated the surface morphology is rough and aggregated having porous structure. The EDX spectra confirmed the existence of present elements in $(Ca_2MgSi_2O_7 : xNb^{5+})$ phosphor. The EDX results also revealed that there were relatively uniform distributions of particles in the system. The excitation spectra indicated the phosphor can be effectively excited by ultraviolet (UV) light, making it attractive as conversion phosphor for LED applications. The $(Ca_2MgSi_2O_7 : xNb^{5+})$ phosphor exhibits bright emission excited at wavelength of 280 nm. Photoluminescence measurements showed that the phosphor exhibited emission peak with good intensity (866 a.u.) at wavelength of 564 nm, corresponding to nearly green emission, indicating that it has favorable properties for application as near ultraviolet LED conversion phosphor.

## 7.2 Future Directions

The approaches used to synthesize and characterize the tetragonal tungsten bronze structured ferroelectrics nanomaterials in this thesis could be applied to synthesize advanced ceramic nanomaterials for device and optoelectronics applications. Based on the experimentally tested and observed data, there were significant enhancements of the optical absorption and emission of stoichiometrically synthesized ferroelectric nanomaterias of $(Ba_{(1.6-3/2X)}Sr_{2.4}Na_2Nb_{10}O_{30} : xHo^{3+})$ with optimum $Ho^{3+}$. Considering the normal ferroelectric nature of $(Ba_{(1.6-3/2X)}Sr_{2.4}Na_2Nb_{10}O_{30} : xHo^{3+})$ and the availability of their crystals, investigations of this material may yield interesting properties in future with dual advantages in it are also lead free ferroelecris materials.

Many potential directions could also be explored for other co-doped tetragonal tungsten broze ferroelectric nanomaterials for further improvements of the properties and enhancing the magnitudes of the main ferroelecric propertis and its transition temperature. Other possibilities include investigation of alternate tetragonally enhanced ferroelectrics such as $(Ba_{(1.6-3/2X)}Sr_{2.4}Na_2Nb_{10}O_{30} : xHo^{3+})$ co-doped with $Eu^{3+}/Tb^{3+}/Dy^{3+}$ and $Y^{3+}$ ions, using rare earth ions substituents with Metals = Sr, Ba, etc.

As phase II of the project we plan to measure the piezoelectric, pyroelectric and ferroelectric properties of the nanomaterials in near future whenever we get any fund. Again it was intended to do the analysis of dielectric measurements, dielectric loss tangent and impedance analysis of the prepared nanomaterials at low and high frequency ranges. We plan to find and determine the transition temperature of the nanomaterials. Through hysteresis loop analysis and dc-resistivity measurement we intended to test its conductivity. Finally the effect of co-doping on their ferroelecric and dielectric properties will be determined.

## Publications

**1. Solomon H. Didu**, Menberu M. Woldemariam, Shimelis A. Kitte, Shimelis L. Beshawured, S. Bheemeswara Rao, Nebiyu G. Debelo, :Synthesis and Characterization of $(Ba_{(1.6-3/2X)}Sr_{2.4}Na_2Nb_{10}O_{30} : xHo^{3+})$ Ferroelectric nanomaterials by Solid state reaction routes for Device Applications, Solid State Sciences 146 (2023) 107357, ELSEVIER.

**2. Solomon H. Didu**, Menberu M. Woldemariam and Nebiyu G. Debelo: Green Synthesis of Niobium doped Calcium Magnesium Silicate Phosphor Using Stenotaphrum Secundatum Grass Extract: International Journal of Thin Films Science and Technology; (12, No. 2, 115-120 (2023))

**3. Solomon H. Didu**, Menberu M. Woldemariam, Shimelis A. Kitte, 2Fuad A. Bushira Nebiyu G. Debelo: Investigation of Barium Strontium Sodium Niobate Ferroelectric nanomaterial with Holmium ion additive for Optoelectronic Application: (XXX 2023): Submitted (Heliyon/ELSEVIER Journal)

## Conference and Workshop Presentations and participation

**1. Certificate of Achievement**: The 2024 EPSNA Scholarship for Ph.D. students is award in recognition of the highest scholastic achievement and service to the community. ETHIOPIAN PHYSICAL SOCIETY NORTH AMERICA, February 17, 2024.

**2. Certificate of Presentation**: In recognition to his research paper oral presentation at the 18Th Annual conference of the Ethiopia Physical Society, held at Addis Ababa University February 17, 2024.

**3. Certificate of Presentation**:Certificate Awarded to Solomon H.D. In recognition of the professional contribution as a Paper Presenter for the 3rd National Research Symposium on ” Emerging Technology for Building Green Economy”, which was held at ASTU, Adama, Ethiopia on May 24-25, 2024.

**4. Ethiopian Physical Society (EPS 15th Annual National Conference)** -The Role of Physics in Technology Advancement and Development of Society (February 26-27 2021, Wolkite University, Ethiopia) (Paper Presenter).

**5. Worksop participation** on Short term training on Advanced Analytical Instrumentation Techniques: (XRD,FTIR,SEM,TEM,EDX,UV-Vis, DSC,TGA,GC-MS, NMR,HPLC,BET) December, 23-28 /2021.

**6. Certificate of Participation:** This is to certify that Mr.Solomon Hailemariam Didu has successfully participated in the EPSNA Summer school on physics, applid phyics, physics education and mathematics held from August 14 to 18 2023. ETHIOPIAN PHYSICAL SOCITY IN NORTH AMERICA

**7. Certificate of Participation**: In recognition to his Participation at the 18Th Annual conference of the Ethiopia Physical Society, held at Addis Ababa University February 16 to 17, 2024.

**8. Certificate of Participation**: This certificate is awarded to Mr.Solomon Hailemariam Didu who has successfully completed the training on SCIENTFIC WRITING, PUBLICATIONS ETHICS, E-RESOURCE MANAGEMENT SOFTWARE Organized by College of Natural sciences from April 17-18 , 2018

**9. Certificate of Participation**: This certificate is awarded to Mr.Solomon Hailemariam Didu For his/her participation and successful completetion of training on Scientfic Writing and Publication Ethics organized for PhD students and Junior staffs of College of Natural sciences by Jimma University in collaboration with TDR/WHO/CRDF,30-31, March 2022

**10. Certificate of Participation**: This certificate is awarded to Mr.Solomon Hailemariam Didu In Recognition to active participation in the Ethiopian Universities curriculum (Four year BSc Natural Sciences Program Curriculum) Development process during the academic year 2020.

**11. Certificate of Participation**: This certificate is awarded to Mr.Solomon Hailemariam Didu IN RECOGNITION OF HIS VALUABLE CONTRIBUTION IN delivering and coordination of the community service project entitled Training Secondary Schoool Teachers of Jimma Town and Jimma Zone on Practical Activities of Basic Science Course: Biology, Chemistry and Physics Sponsored by office of Vice President for Research and Community Services, Jimma University. Held from July 13-14 2018.

**12. Certificate of Competency**: This to certify that Mr.Solomon Hailemariam Didu has successfully completed the Training program on Competency-based Teaching, Learning and Assessement conducted by Jimma University. The Training spanned three days, from 6-8 February 2024, comprising a total of 18 hours of intensive learning.

# REFERENCE

[1] Y. Saito, H. Takao, T. Tani, T. Nonoyama, K. Takatori, T. Homma, T. Nagaya, M. Nakamura, Lead-free piezoceramics, Nature, 432 (2004) 84-87.

[2] R. Zuo, X. Fang, C. Ye, Phase structures and electrical properties of new lead-free (Na0. 5K0. 5) NbO3-(Bi0. 5Na0. 5) TiO3 ceramics, Applied Physics Letters, 90 (2007).

[3] V.V. Shvartsman, D.C. Lupascu, Lead?free relaxor ferroelectrics, Journal of the American Ceramic Society, 95 (2012) 1-26.

[4] F.Z. Yao, K. Wang, W. Jo, K.G. Webber, T.P. Comyn, J.X. Ding, B. Xu, L.Q. Cheng, M.P. Zheng, Y.D. Hou, Diffused phase transition boosts thermal stability of high?performance lead?free piezoelectrics, Advanced Functional Materials, 26 (2016) 1217-1224.

[5] M.E. Lines, A.M. Glass, Principles and applications of ferroelectrics and related materials, Oxford university press, 2001.

[6] G.H. Haertling, Ferroelectric ceramics: history and technology, Journal of the American Ceramic Society, 82 (1999) 797-818.

[7] L.E. Cross, Relaxor ferroelectrics, Ferroelectrics, 76 (1987) 241-267.

[8] W. Liu, X. Ren, Large piezoelectric effect in Pb-free ceramics, Physical review letters, 103 (2009) 257602.

[9] Z. Kutnjak, J. Petzelt, R. Blinc, The giant electromechanical response in ferroelectric relaxors as a critical phenomenon, Nature, 441 (2006) 956-959.

[10] J.F. Scott, Room-temperature multiferroic magnetoelectrics, NPG Asia Materials, 5 (2013) e72-e72.

[11] Y.S. Oh, X. Luo, F.-T. Huang, Y. Wang, S.-W. Cheong, Experimental demonstration of hybrid improper ferroelectricity and the presence of abundant charged walls in (Ca, Sr) 3 Ti 2 O 7 crystals, Nature materials, 14 (2015) 407-413.

[12] L. Jin, F. Li, S. Zhang, Decoding the fingerprint of ferroelectric loops: comprehension of the material properties and structures, Journal of the American Ceramic Society, 97 (2014) 1-27.

[13] J. Scott, Applications of modern ferroelectrics, science, 315 (2007) 954-959.

[14] J.R. Oliver, R.R. Neurgaonkar, L.E. Cross, Ferroelectric properties of tungsten bronze morphotropic phase bounary systems, Journal of the American Ceramic Society, 72 (1989) 202-211.

[15] R. Neurgaonkar, W. Cory, J. Oliver, L.E. Cross, Growth and properties of tungsten bronze K3Li2Nb5O15 single crystals, Materials research bulletin, 24 (1989) 1025-1030.

[16] C. Yang, Y. Guo, B. Wang, Photorefractive properties of Mn doped K3Li2Nb5O15 crystal, Optics communications, 225 (2003) 383-386.

[17] A. Glass, Investigation of the electrical properties of Sr1? x Ba x Nb2O6 with special reference to pyroelectric detection, Journal of Applied Physics, 40 (1969) 4699-4713.

[18] T. Lukasiewicz, M. Swirkowicz, J. Dec, W. Hofman, W. Szyrski, Strontium-barium niobate single crystals, growth and ferroelectric properties, Journal of Crystal Growth, 310 (2008) 1464-1469.

[19] X. Zhu, M. Fu, M. Stennett, P. Vilarinho, I. Levin, C. Randall, J. Gardner, F. Morrison, I. Reaney, A crystal-chemical framework for relaxor versus normal ferroelectric behavior in tetragonal tungsten bronzes, Chemistry of Materials, 27 (2015) 3250-3261.

[20] G. Burns, Properties and improvements of tungsten bronze ferroelectrics, IEEE Transactions on Electron Devices, 16 (1969) 506-510.

[21] E. Giess, B. Scott, G. Burns, D. O'kane, A. Segmller, Alkali Strontium?Barium?Lead Niobate Systems with a Tungsten Bronze Structure: Crystallographic Properties and Curie Points, Journal of the American Ceramic Society, 52 (1969) 276-281.

[22] S. Jindal, A. Vasishth, S. Devi, G. Anand, A review on tungsten bronze ferroelectric ceramics as electrically tunable devices, Integrated Ferroelectrics, 186 (2018) 1-9.

[23] X. Chen, J. Yang, Dielectric characteristics of ceramics in BaO-Nd2O3-TiO2-Ta2O5 system, Journal of the European Ceramic Society, 19 (1999) 139-142.

[24] X. Chen, Z. Xu, J. Li, Dielectric ceramics in the BaO-Sm2O3-TiO2-Ta2O5 quaternary system, Journal of Materials Research, 15 (2000) 125-129.

[25] X. Chen, Y. Sun, X. Zheng, High permittivity and low loss dielectric ceramics in the BaO-La2O3-TiO2-Ta2O5 system, Journal of the European Ceramic Society, 23 (2003) 1571-1575.

[26] H. Sharma, K. Kumari, S. Giri, Studies of structural and dielectric properties of Ba 5 BiTi 3 Nb 7 O 30 ceramics, Bulletin of Materials Science, 22 (1999) 757-759.

[27] X. Zheng, X. Chen, Crystal structure and dielectric properties of ferroelectric ceramics in the BaO-Sm2O3-TiO2-Nb2O5 system, Solid State Communications, 125 (2003) 449-454.

[28] Y. Sun, X. Chen, X. Zheng, Tungsten bronze type dielectrics in SrO-Sm2O3-TiO2-Nb2O5 system and their dielectric anomaly, Journal of applied physics, 96 (2004) 7435-7439.

[29] S. Kamba, S. Veljko, M. Kempa, M. Savinov, V. Bovtun, P. Van?k, J. Petzelt, M. Stennett, I. Reaney, A. West, Dielectric spectra of a new relaxor ferroelectric system Ba2LnTi2Nb3O15 (Ln= La, Nd), Journal of the European Ceramic Society, 25 (2005) 3069-3073.

[30] M. Stennett, I. Reaney, G. Miles, D. Woodward, A. West, C. Kirk, I. Levin, Dielectric and structural studies of Ba2MTi2Nb3O15 (BMTNO15, M= Bi3+, La3+, Nd3+, Sm3+, Gd3+) tetragonal tungsten bronze-structured ceramics, Journal of applied physics, 101 (2007).

[31] I. Levin, M.C. Stennett, G.C. Miles, D. Woodward, A.R. West, I.M. Reaney, Coupling between octahedral tilting and ferroelectric order in tetragonal tungsten bronze-structured dielectrics, Applied physics letters, 89 (2006).

[32] C.A. Kirk, M.C. Stennett, I.M. Reaney, A.R. West, A new relaxor ferroelectric, Ba 2 LaTi 2 Nb 3 O 15, Journal of Materials Chemistry, 12 (2002) 2609-2611.

[33] G. Miles, M. Stennett, I. Reaney, A. West, Temperature-dependent crystal structure of ferroelectric Ba 2 LaTi 2 Nb 3 O 15, Journal of Materials Chemistry, 15 (2005) 798-802.

[34] X. Zhu, X. Chen, X. Liu, Y. Yuan, Dielectric characteristics and diffuse ferroelectric phase transition in Sr4La2Ti4Nb6O30 tungsten bronze ceramics, Journal of materials research, 21 (2006) 1787-1792.

[35] X.L. Zhu, X.M. Chen, X.G. Li, Dielectric relaxation and ultrasonic attenuation of Sr4La2Ti4Nb6O30 tungsten bronze ceramics, Applied physics letters, 90 (2007).

[36] X. Zhu, S. Wu, X. Chen, Dielectric anomalies in (BaxSr1? x) 4Nd2Ti4Nb6O30 ceramics with various radius differences between A1-and A2-site ions, Applied Physics Letters, 91 (2007).

[37] A. Magnli, The crystal structure of tetragonal potassium tungsten bronze, Ark. Kemi, 1 (1949) 213-221.

[38] M. Trubelja, E. Ryba, D. Smith, A study of positional disorder in strontium barium niobate, Journal of materials science, 31 (1996) 1435-1443.

[39] M. Said, T. Velayutham, W. Gan, W. Abd Majid, The structural and electrical properties of SrxBa (1 x) Nb2O6 (SBN) ceramic with varied composition, Ceramics International, 41 (2015) 7119-7124.

[40] M.-S. Kim, P. Wang, J.-H. Lee, J.-J. Kim, H.Y. Lee, S.-H. Cho, Site occupancy and dielectric characteristics of strontium barium niobate ceramics: Sr/Ba ratio dependence, Japanese journal of applied physics, 41 (2002) 7042.

[41] P. Patro, A. Kulkarni, C. Harendranath, Dielectric and ferroelectric behavior of SBN50 synthesized by solid-state route using different precursors, Ceramics international, 30 (2004) 1405-1409.

[42] I. Santos, D. Sp?nola, D. Garcia, J. Eiras, Dielectric behavior and diffuse phase transition features of rare earth doped Sr 0.61 Ba 0.39 Nb 2 O 6 ferroelectric ceramics, Journal of applied physics, 92 (2002) 3251-3256.

Ba 0.39 Nb 2 O 6 ferroelectric ceramics, Journal of applied physics, 92 (2002) 3251-3256.

[43] I.P.Sahu, D.P. Bisen, N. Brahme, L. Wanjari, R.K. Tamrakar, Structural characterization and luminescence properties of bluish-green-emitting SrCaMgSi2O7:Eu2+, Dy3+ phosphor by solid-state reaction method, Research on Chemical Intermediates, 41 (2015) 8797-8814.

[44] E. Karacaoglu, B. Karasu, Effect of activators and calcination on luminescence properties of akermanite type phosphors Indian Journal of Chemistry. Section A, 54 (2015) 1394-1401

[45] S.Sharma, S. Dubey, The significant properties of silicate based luminescent

nanomaterials in various fields of applications: a review, International Journal of Scientific Research in Physics and Applied Sciences, 9 (2021) 37-41.

[46] F. Wang, H. Chen ,Influenceof Mn2+ doping on the emission spectrum of Sr2La8(SiO4)6O2:Eu(2+,3+) phosphor, Inorganic Chemistry Communications, 142 (2022) 109625.

[47] N. Sboui, H. Agougui, M.Jabli , K. Boughzala, Synthesis, physico-chemical, and structural properties of silicate apatites: Effect of synthetic methods on apatite structure and dye removal, Inorganic Chemistry Communications, 142 (2022) 109628.

[48] T.G.V.M. Rao, A.R. Kumar,N. Veeraiah, M.R. Reddy, Optical and structural investigation of Sm3+-Nd3+ co-doped in magnesium lead borosilicate glasses, Journal of Physics and Chemistry of Solids, 74 (2013) 410-417.

[49] G.J. Talwar, C.P. Joshi, S.V. Moharil, S.M. Dhopte, P.L. Muthal, V.K. Kondawar, Combustion synthesis of Sr3MgSi2O8:Eu2+ andSr2MgSi2O7:Eu2+ phosphors, Journal of Luminescence, 129 (2009) 1239-1241.

[50] S.Vakhrushev, A. Naberezhnov, B. Dkhil, J.M. Kiat, V. Shwartsman, A. Kholkin, B. Dorner, A. Ivanov, Structure of nanodomains in relaxors, in: AIP Conference Proceedings, American Institute of Physics, 2003, pp. 74-83.

[51] F. Prokert, D. Sangaa, B. Savenko, Neutron diffraction studies of the incommensurate modulation structure in SrxBa1-xNb2O6 mixed crystals of various compositions, Ferroelectrics Letters Section, 13 (1991) 61-66.

[52] R. Neurgaonkar, W. Cory, J. Oliver, Growth and applications of ferroelectric tungsten bronze family crystals, Ferroelectrics, 51 (1983) 3-8.

[53] C. David, T. Granzow, A. Tunyagi, M. Whlecke, T. Woike, K. Betzler, M. Ulex, M. Imlau, R. Pankrath, Composition dependence of the phase transition temperature in SrxBa1? xNb2O6, physica status solidi (a), 201 (2004) R49-R52.

[54] A. Kumar, J. Prakash, D. Mehta, A. Biradar, W. Haase, Enhanced photoluminescence in gold nanoparticles doped ferroelectric liquid crystals, Applied Physics Letters, 95 (2009).

[55] S.-Y. Huang, C.-C. Peng, L.-W. Tu, C.-T. Kuo, Enhancement of luminescence of

nematic liquid crystals doped with silver nanoparticles, Molecular Crystals and Liquid Crystals, 507 (2009) 301-306.

[56] A. Trovarelli, Catalytic properties of ceria and CeO2-containing materials, Catalysis Reviews, 38 (1996) 439-520.

[57] P. Goel, M. Arora, A. Biradar, Evolution of excitation wavelength dependent photoluminescence in nano-CeO 2 dispersed ferroelectric liquid crystals, RSC Advances, 4 (2014) 11351-11356.

[58] Z. Gharari, P. Hanachi, T.R. Walker, Green synthesized Ag-nanoparticles using Scutellaria multicaulis stem extract and their selective cytotoxicity against breast cancer, Analytical Biochemistry, 653 (2022) 114786.

[59] D. Borah, P. Saikia, P.Sarmah, D. Gogoi, J. Rout, N.N. Ghosh, C.R. Bhattacharjee, Composition controllable alga-mediated green synthesis of covellite CuS nanostructure: An efficient photocatalyst for degradation of toxic dye, Inorganic Chemistry Communications, 142 (2022) 109608.

[60] S. Sharma, S.K. Dubey, A.K. Diwakar, S. Pandey, Novel White Light Emitting (Ca2MgSi2O7:Dy3+) Phosphor. , Journal of Materials Science Research and Reviews, 8 (2021) 164-171.

[61] Z. Gubinyi, C. Batur, A. Sayir, F. Dynys, Electrical properties of PZT piezoelectric ceramic at high temperatures, Journal of Electroceramics, 20 (2008) 95-105.

[62] A. Safari, R.K. Panda, V.F. Janas, Ferroelectric ceramics: processing, properties and applications, Applications of Ferroelectric Ceramic Materials, 37 (2011).

[63] J.F. Scott, J.F. Scott, Wafer Bonding, Ferroelectric Memories, (2000) 185-187.

[64] H. Fan, G.T. Park, J.J. Choi, H.E. Kim, Preparation and Characterization of Sol-Gel?Derived Lead Magnesium Niobium Titanate Thin Films with Pure Perovskite Phase and Lead Oxide Cover Coat, Journal of the American Ceramic Society, 85 (2002) 2001-2004.

[65] G. Anand, P. Kuchhal, P. Sarah, The structure and complex impedance spectroscopy of Sr1-xCaxBi4Ti4O15 (x= 0, 0.2, 0.4, 0.6, 0.8) ceramics, Procedia Materials Science, 10 (2015) 533-541.

[66] G. Anand, A. James, P. Sarah, Dielectric and Polarization Studies of Ca Substi-

tuted in Bi4SrTi4O15 Ceramics, Integrated Ferroelectrics, 116 (2010) 137-144.

[67] D. Bao, X. Yao, K. Shinozaki, N. Mizutani, Crystallization and optical properties of sol-gel-derived PbTiO3 thin films, Journal of Physics D: Applied Physics, 36 (2003) 2141.

[68] S. Sakka, Sol-Gel Science and Technology: Topics in Fundamental Research and Applications (4 Volume Set), Taylor & Francis US, 2002.

[69] G. Anand, A. James, T.R. Krishna, P. Sarah, Synthesis and characterisation of strontium bismuth titanate ceramics via high-energy mechanical milling, DEFENCE SCIENCE JOURNAL-NEW DELHI-, 57 (2007) 29.

[70] P. Jamieson, S. Abrahams, J. Bernstein, Ferroelectric tungsten bronze?type crystal structures. II. Barium sodium niobate Ba (4+ x) Na (2? 2x) Nb10O30, The Journal of Chemical Physics, 50 (1969) 4352-4363.

[71] X.L. Zhu, K. Li, X.M. Chen, Ferroelectric transition and low?temperature dielectric relaxations in filled tungsten bronzes, Journal of the American Ceramic Society, 97 (2014) 329-338.

[72] V. Bovtun, S. Kamba, S. Veljko, D. Nuzhnyy, K. Knek, M. Savinov, J. Petzelt, Relaxor-like behavior of lead-free Sr2LaTi2Nb3O15 ceramics with tetragonal tungsten bronze structure, Journal of Applied Physics, 101 (2007).

[73] X. Zhu, X. Chen, Thermal hysteresis of ferroelectric transition in Sr4R2Ti4Nb6O30 (R= Sm and Eu) tetragonal tungsten bronzes, Applied Physics Letters, 96 (2010).

[74] X.L. Zhu, X.M. Chen, Ferroelectric properties and polarization dynamics in Ba4Sm2Ti4Ta6O30 tungsten bronze ceramics, Applied Physics Letters, 108 (2016).

[75] W.B. Feng, X.L. Zhu, X.Q. Liu, X.M. Chen, Crystal structure, ferroelectricity and polar order in a Ba 4 R 2 Zr 4 Nb 6 O 30 (R= La, Nd, Sm) tetragonal tungsten bronze new system, Journal of Materials Chemistry C, 5 (2017) 4009-4016.

[76] D. Michau, A. Simon, M. Maglione, Lead-free relaxor thin films of tungsten bronze symmetry, Journal of Physics D: Applied Physics, 42 (2009) 075407.

[77] M. Josse, O. Bidault, F. Roulland, E. Castel, A. Simon, D. Michau, R. von Der Mhll, O. Nguyen, M. Maglione, The Ba2LnFeNb4O15 ”tetragonal tungsten bronze”: Towards RT composite multiferroics, Solid state sciences, 11 (2009) 1118-1123.

[78] X.L. Zhu, X.Q. Liu, X.M. Chen, Crystal structure and dielectric properties of Sr5RTi3Nb7O30 (R= La, Nd, Sm, and Eu) tungsten bronze ceramics, Journal of the American Ceramic Society, 94 (2011) 1829-1836.

[79] M.M. Mao, K. Li, X.L. Zhu, X.M. Chen, Incommensurate and commensurate modulations of Ba5RTi3Nb7O30 (R= La, Nd) tungsten bronzes and the ferroelectric domain structures, Journal of Applied Physics, 117 (2015).

[80] C. Kirk, I. Levin, MC Stennett, IM Reaney, GC Miles, DI Woodward, and AR West Department of Engineering Materials, University of Sheffield, Sheffield S1 3JD, United Kingdom, JOURNAL OF APPLIED PHYSICS, 101 (2007) 104114.

[81] M. Prades, H. Beltrn, N. Mas, E. Cordoncillo, A.R. West, Phase transition hysteresis and anomalous Curie-Weiss behavior of ferroelectric tetragonal tungsten bronzes Ba2RETi2Nb3O15: RE= Nd, Sm, Journal of Applied Physics, 104 (2008).

[82] K. Li, X. Li Zhu, X. Qiang Liu, X. Ming Chen, Relaxor ferroelectric characteristics of Ba5LaTi3Nb7O30 tungsten bronze ceramics, Applied Physics Letters, 100 (2012).

[83] J. Gardner, F.D. Morrison, A-site size effect in a family of unfilled ferroelectric tetragonal tungsten bronzes: Ba 4 R 0.67 Nb 10 O 30 (R= La, Nd, Sm, Gd, Dy and Y), Dalton transactions, 43 (2014) 11687-11695.

[84] N. Wakiya, J.-K. Wang, A. Saiki, K. Shinozaki, N. Mizutani, Synthesis and dielectric properties of Ba1? xR2x/3Nb2O6 (R: rare earth) with tetragonal tungsten bronze structure, Journal of the European Ceramic Society, 19 (1999) 1071-1075.

[85] E. Subbarao, G. Shirane, F. Jona, X-ray dielectric, and optical study of ferroelectric lead metatantalate and related compounds, Acta Crystallographica, 13 (1960) 226-231.

[86] M. Francombe, The relation between structure and ferroelectricity in lead barium and barium strontium niobates, Acta Crystallographica, 13 (1960) 131-140.

[87] T. Shrout, L. Cross, D. Hukin, Ferroelectric properties of tungsten bronze lead barium niobate (PBN) single crystals, Ferroelectrics, 44 (1982) 325-330.

[88] M. Yokosuka, A new transparent ferroelectric ceramic, lanthanum modified lead-barium metaniobate (PBLN), Japanese Journal of Applied Physics, 16 (1977) 379.

[89] J.P. Dougherty, P.S.U.U.P.M.R. LAB, U. S./Japan Seminar on Dielectric and Piezoelectric Ceramics Held in Kyoto, Japan on 11-14 December 1990, in, 1991.

[90] K. Nagata, Y. Kawatani, K. Okazaki, Anisotropies of hot-pressed transparent (Pb, Ba, La) Nb2O6 ceramics, Japanese journal of applied physics, 22 (1983) 1353.

[91] R.R. Neurgaonkar, W. Cory, J. Oliver, M. Ewbank, W. Hall, Development and modification of photorefractive properties in the tungsten bronze family crystals, Optical Engineering, 26 (1987) 392-405.

[92] K. Umakantham, K. Chandramouli, G. Nageswara Rao, A. Bhanumathi, Structural properties of inorganic materials: tungsten bronze SBN ceramics, Bulletin of Materials Science, 19 (1996) 345-355.

[93] F. Guerrero, H. Amori n, J.J. Portelles, A. Fundora, J.s.M. Siqueiros, G.A. Hirata, S. Aguilera, Dielectric Properties of La 3+ Doped Sr 0.3-3y/2 La y Ba 0.7 Nb 2 O 6 Ceramics Prepared under Different Sintering Conditions, Journal of electroceramics, 3 (1999) 377-385.

[94] H. Amorin, M. Venet, F. Guerrero, A. Fundora, E. Martinez, J. Portelles, J. Siqueiros, Thermally stimulated depolarization current in a modified SBN ferroelectric ceramic system, in: ISAF 2000. Proceedings of the 2000 12th IEEE International Symposium on Applications of Ferroelectrics (IEEE Cat. No. 00CH37076), IEEE, 2000, pp. 775-778.

[95] I.P. Sahu, D.P. Bisen, N. Brahme, R.K. Tamrakar, Photoluminescence properties of europium doped di-strontium magnesium di-silicate phosphor by solid state reaction method, Journal of Radiation Research and Applied Sciences, 8 (2015) 104-109.

[96] P. Imchen, M. Ziekhr, B.K. Zhimomi, T. Phucho, Biosynthesis of silver nanoparticles using the extract of Alpinia galanga rhizome and Rhus semialata fruit and their antibacterial activity, Inorganic Chemistry Communications, 142 (2022) 109599.

[97] P. Jamieson, S. Abrahams, J. Bernstein, Ferroelectric tungsten bronze?type crystal structures. I. Barium strontium niobate Ba0. 27Sr0. 75Nb2O5. 78, The Journal of Chemical Physics, 48 (1968) 5048-5057.

[98] M.T. Buscaglia, M. Bassoli, V. Buscaglia, R. Vormberg, Solid?state synthesis of

nanocrystalline BaTiO3: reaction kinetics and powder properties, Journal of the American Ceramic Society, 91 (2008) 2862-2869.

[99] A.M. Nartowski, I.P. Parkin, M. Mackenzie, A.J. Craven, Solid state metathesis: synthesis of metal carbides from metal oxides, Journal of Materials Chemistry, 11 (2001) 3116-3119. [100] C. Kittel, Introduction to solid state physics, John Wiley & sons, inc, 2005.

[101] I. Grinberg, D.V. West, M. Torres, G. Gou, D.M. Stein, L. Wu, G. Chen, E.M. Gallo, A.R. Akbashev, P.K. Davies, Perovskite oxides for visible-light-absorbing ferroelectric and photovoltaic materials, Nature, 503 (2013) 509-512.

[102] E. Kaidashev, M.v. Lorenz, H. Von Wenckstern, A. Rahm, H.-C. Semmelhack, K.-H. Han, G. Benndorf, C. Bundesmann, H. Hochmuth, M. Grundmann, High electron mobility of epitaxial ZnO thin films on c-plane sapphire grown by multistep pulsed-laser deposition, Applied Physics Letters, 82 (2003) 3901-3903.

[103] D.K. Bowen, B.K. Tanner, High resolution X-ray diffractometry and topography, CRC press, 1998.

[104] Y. Leng, Materials characterization: introduction to microscopic and spectroscopic methods, John Wiley & Sons, 2013.

[105] J. Gilfrich, Structural and Chemical Analysis of Materials: X?ray, Electron and Neutron Diffraction, X?ray, Electron and Ion Spectrometry, Electron Microscopy. JP Eberhart Published by John Wiley & Sons Ltd, Chichester, 1991; 545 pages; ISBN 0 471 92977 8, in, Wiley Online Library, 1993.

[106] V. Craciun, J. Elders, a.J. Gardeniers, I.W. Boyd, Characteristics of high quality ZnO thin films deposited by pulsed laser deposition, Applied physics letters, 65 (1994) 2963-2965.

[107] T.Y. Ma, S.C. Lee, Effects of aluminum content and substrate temperature on the structural and electrical properties of aluminum-doped ZnO films prepared by ultrasonic spray pyrolysis, Journal of Materials Science: Materials in Electronics, 11 (2000) 305-309.

[108] V. Pet??ek, M. Duek, L. Palatinus, Crystallographic computing system JANA2006: general features, Zeitschrift fr Kristallographie-Crystalline Materials, 229 (2014)

345-352.

[109] A. Charlesby, Atomic radiation and polymers: international series of monographs on radiation effects in materials, Elsevier, 2016.

[110] K. Heister, M. Zharnikov, M. Grunze, L. Johansson, A. Ulman, Characterization of X-ray induced damage in alkanethiolate monolayers by high-resolution photoelectron spectroscopy, Langmuir, 17 (2001) 8-11.

[111]F.-Y. Zhu, Q.-Q. Wang, X.-S. Zhang, W. Hu, X. Zhao, H.-X. Zhang, 3D nanostructure reconstruction based on the SEM imaging principle, and applications, Nanotechnology, 25 (2014) 185705.

[112] J.I. Goldstein, D.E. Newbury, P. Echlin, D.C. Joy, A. Romig, C.E. Lyman, C. Fiori, E. Lifshin, J.I. Goldstein, D.E. Newbury, Coating and conductivity techniques for SEM and microanalysis, Scanning Electron Microscopy and X-Ray Microanalysis: A Text for Biologists, Materials Scientists, and Geologists, (1992) 671-740.

[113] E. Gottardini, S. Rossi, F. Cristofolini, L. Benedetti, Use of Fourier transform infrared (FT-IR) spectroscopy as a tool for pollen identification, Aerobiologia, 23 (2007) 211-219.

[114] I. Taniguchi, Powder properties of partially substituted LiMxMn2? xO4 (M= Al, Cr, Fe and Co) synthesized by ultrasonic spray pyrolysis, Materials chemistry and physics, 92 (2005) 172-179.

[115] B.C. Smith, Fundamentals of Fourier transform infrared spectroscopy, CRC press, 2011.

[116] D.B. Williams, C.B. Carter, D.B. Williams, C.B. Carter, Other Imaging Techniques, Transmission Electron Microscopy: A Textbook for Materials Science, (2009) 511-532.

[117] S.L. King, J.G. Gardeniers, I.W. Boyd, Pulsed-laser deposited ZnO for device applications, Applied surface science, 96 (1996) 811-818.

[118] J.-H. Lee, B.-O. Park, Characteristics of Al-doped ZnO thin films obtained by ultrasonic spray pyrolysis: effects of Al doping and an annealing treatment, Materials Science and Engineering: B, 106 (2004) 242-245.

[119] N.R. Council, Condensed-matter and Materials Physics: Basic Research for To-

morrow's Technology, National Academies Press, 1999.

[120] G.C. Miles, M.C. Stennett, D. Pickthall, C.A. Kirk, I.M. Reaney, A.R. West, X-ray diffraction data for the new ferroelectric tetragonal tungsten bronze phases, Ba2RETi2M3O15: M= Nb and RE= La, Pr, Nd, Sm, Gd, Dy,(Bi); M= Ta and RE= La, Nd, Powder diffraction, 20 (2005) 43-46.

[121] S. Chavan, P. Sastry, A. Tyagi, Combustion synthesis of nano-crystalline Nd-doped ceria and Nd2O3 and their fractal behavior as studied by small angle X-ray scattering, Journal of alloys and compounds, 456 (2008) 51-56.

[122] N. Mir, M. Salavati-Niasari, Effect of tertiary amines on the synthesis and photovoltaic properties of TiO2 nanoparticles in dye sensitized solar cells, Electrochimica Acta, 102 (2013) 274-281.

[123] S. Zinatloo-Ajabshir, M. Salavati-Niasari, Novel poly (ethyleneglycol)-assisted synthesis of praseodymium oxide nanostructures via a facile precipitation route, Ceramics International, 41 (2015) 567-575.

[124] M. Zawadzki, Microwave-assisted synthesis and characterization of ultrafine neodymium oxide particles, Journal of alloys and compounds, 451 (2008) 297-300.

[125] G.A. Mekhemer, Surface acid-base properties of holmium oxide catalyst: in situ infrared spectroscopy, Applied Catalysis A: General, 275 (2004) 1-7.

[126] K. Shafiq, M. Aadil, W. Hassan, Q. Choudhry, S. Gul, A. Rais, A.A. Fattah, K.H. Mahmoud, M.Z. Ansari, Cobalt and holmium co-doped nickel ferrite nanoparticles: synthesis, characterization and photocatalytic application studies, Zeitschrift fr Physikalische Chemie, 237 (2023) 1325-1344.

[127] I.-E. Nylund, N.S. Lndal, J. Walker, P.E. Vullum, M.-A. Einarsrud, T. Grande, Cation Disorder in Ferroelectric Ba4M2Nb10O30 (M= Na, K, and Rb) Tetragonal Tungsten Bronzes, Inorganic Chemistry, 61 (2022) 15540-15546.

[128] J.F. Scott, J.F. Scott, Frequency dependence, Ferroelectric Memories, (2000) 145-147.

[129] G. Anand, P. Kuchhal, P. Sarah, AC and DC Conductivity Studies on Lead-Free Ceramics: Sr1-x Ca x Bi4Ti4O15 (x= 0, 0.2, 0.4, 0.6, 0.8), Particulate Science and Technology, 33 (2015) 41-46.

[130] S. Wemple, M. DiDomenico Jr, I. Camlibel, Relationship between linear and quadratic electro?optic coefficients in LiNbO3, LiTaO3, and other oxygen?octahedra ferroelectrics based on direct measurement of spontaneous polarization, Applied Physics Letters, 12 (1968) 209-211.

[131] J. Scott, Ferroelectrics go bananas, Journal of Physics: Condensed Matter, 20 (2007) 021001.

[132] R. Neurgaonkar, W. Cory, J. Oliver, E. Sharp, G. Wood, G. Salamo, Growth and optical properties of ferroelectric tungsten bronze crystals, Ferroelectrics, 142 (1993) 167-188.

[133] A. Magnli, B. Blomberg, Contribution to the knowledge of the alkali tungsten bronzes, Acta chem. scand, 5 (1951) 372-378.

[134] J.B. Felder, W. Wong-Ng, R.A. Qabbani, R.S. Roth, B.H. Toby, J.Y. Chan, Structural investigation of the ”tripled-tetragonal-tungsten-bronze” phases Sr2M10? xO27? y (M= Nb, Ta), Polyhedron, 170 (2019) 359-363.

[135] A. Wadsley, Crystal chemistry of non-stoicheiometric compounds, (1955).

[136] C.-W. Nan, M. Bichurin, S. Dong, D. Viehland, G. Srinivasan, Multiferroic magnetoelectric composites: Historical perspective, status, and future directions, Journal of applied physics, 103 (2008).

[137] M.-L. Hicks, A.C. Pakpour-Tabrizi, R.B. Jackman, Diamond Etching Beyond 10 ? m with Near-Zero Micromasking, Scientific Reports, 9 (2019) 15619.

[138] J. Ma, J. Hu, Z. Li, C.W. Nan, Recent progress in multiferroic magnetoelectric composites: from bulk to thin films, Advanced materials, 23 (2011) 1062-1087.

[139] N.J. Vickers, Animal communication: when i’m calling you, will you answer too?, Current biology, 27 (2017) R713-R715.

[140] R. Gao, X. Qin, Q. Zhang, Z. Xu, Z. Wang, C. Fu, G. Chen, X. Deng, W. Cai, A comparative study of the dielectric, ferroelectric and anomalous magnetic properties of Mn0. 5Mg0. 5Fe2O4/Ba0. 8Sr0. 2Ti0. 9Zr0. 1O3 composite ceramics, Materials Chemistry and Physics, 232 (2019) 428-437.

[141] W. Abbass, M.I. Khan, S. Mourad, Experimentation and predictive models for properties of concrete added with active and inactive SiO2 fillers, Materials, 12

(2019) 299.

[142] M.l. Josse, P. Heijboer, M. Albino, F. Molinari, F. Porcher, R. Decourt, D. Michau, E. Lebraud, P. Veber, M. Velazquez, Original crystal-chemical behaviors in (Ba, Sr) 2Ln (Fe, Nb, Ta) 5O15 tetragonal tungsten bronze: Anion-driven properties evidenced by cationic substitutions, Crystal growth & design, 14 (2014) 5428-5435.

[143] L.-J. Gao, X.-L. Liu, J.-Q. Zhang, S.-Q. Wang, J.-F. Chen, Grain-controlled barium titanate ceramics prepared from high-gravity reactive precipitation process powder, Materials chemistry and physics, 88 (2004) 27-31.

[144] T. Mitsui, W.B. Westphal, Dielectric and X-Ray Studies of Ca x Ba 1? x Ti O 3 and Ca x Sr 1? x Ti O 3, Physical Review, 124 (1961) 1354.

[145] G. Distler, V. Konstantinova, Y.M. Gerasimov, G. Tolmacheva, Interaction of defect and domain structures of triglycine sulphate crystals in ferroelectric and paraelectric states, Nature, 218 (1968) 762-765.

[146] M. Rashid, W. Hassan, M. Aadil, H. Somaily, N.M. Mahdi, R. Lataef, A.G. Taki, K. Srithilat, D.F. Baamer, S.M. Albukhari, Solar-light-driven and magnetically recoverable doped nano-ferrite: an ideal photocatalyst for water purification applications, Optical Materials, 135 (2023) 113192.

[147] S.Y. Mulushoa, M.T. Wegayehu, G.T. Aregai, N. Murali, M.S. Reddi, B.V. Babu, T. Arunamani, K. Samatha, Synthesis of spinel MgFe2O4 ferrite material and studying its structural and morphological properties using solid state method, Chemical Science, 6 (2017) 653-661.

[148] S.Y. Mulushoa, C.V. Kumari, V. Raghavendra, K.E. Babu, B. Murthy, K. Suribabu, Y. Ramakrishna, N. Murali, Effect of Zn-Cr substitution on the structural, magnetic and electrical properties of magnesium ferrite materials, Physica B: Condensed Matter, 572 (2019) 139-147.

[149] B. Madhavilatha, D. Parajuli, K. Jayadev, C. Komali, N. Murali, V. Veeraiah, K. Samatha, Effect of Cu substitution on magnetic properties of Co0. 6Ni0. 4Fe2O4 nanoferrites, Biointerface Res. Appl. Chem, 12 (2022) 1899-1906.

[150] M. Aadil, T. Kousar, M. Hussain, H. Somaily, A.K. Abdulla, E.R. Muhammad, E.A. Al-Abbad, M.A. Salam, S.M. Albukhari, D.F. Baamer, Generation of meso-

porous npn (ZnO-CuO-CeO2) heterojunction for highly efficient photodegradation of micro-organic pollutants, Ceramics International, 49 (2023) 4846-4854.

[151] K. Chandramouli, B. Suryanarayana, P.P. Varma, V. Raghavendra, K. Emmanuel, P. Taddesse, N. Murali, T.W. Mammo, D. Parajuli, Effect of Cr3+ substitution on dc electrical resistivity and magnetic properties of Cu0. 7Co0. 3Fe2? xCrxO4 ferrite nanoparticles prepared by sol-gel auto combustion method, Results in Physics, 24 (2021) 104117.

[152] H. Klung, L. Alexander, X-ray diffraction procedures, John Wiley & Sons, New York, 1 (1962) 974.

[153] T. Li, M. Aadil, S. Zulfiqar, A. Anwar, S.M. Yakout, N.M. Panduro-Tenazoa, S. Mubeen, Synthesis of doped and porous CuO with boosted light-harvesting features for the photocatalytic mineralization of azo dyes, Ceramics International, 49 (2023) 27827-27836.

[154] S. Zinatloo-Ajabshir, M. Salavati-Niasari, Nanocrystalline Pr 6 O 11: synthesis, characterization, optical and photocatalytic properties, New Journal of Chemistry, 39 (2015) 3948-3955.

[155] M. Pudukudy, A. Hetieqa, Z. Yaakob, Synthesis, characterization and photocatalytic activity of annealing dependent quasi spherical and capsule like ZnO nanostructures, Applied surface science, 319 (2014) 221-229.

[156] Z. Liu, W. Xu, J. Fang, X. Xu, S. Wu, X. Zhu, Z. Chen, Decoration of BiOI quantum size nanoparticles with reduced graphene oxide in enhanced visible-light-driven photocatalytic studies, Applied Surface Science, 259 (2012) 441-447.

[157] J. Petersen, C. Brimont, M. Gallart, G. Schmerber, P. Gilliot, C. Ulhaq-Bouillet, J.-L. Rehspringer, S. Colis, C. Becker, A. Slaoui, Correlation of structural properties with energy transfer of Eu-doped ZnO thin films prepared by sol-gel process and magnetron reactive sputtering, Journal of applied physics, 107 (2010).

[158] K. Fabitha, M.R. Rao, Ho 3+-doped ZnO nano phosphor for low-threshold sharp red light emission at elevated temperatures, JOSA B, 34 (2017) 2485-2492.

[159] S. Babu, Y. Ratnakaram, Emission characteristics of holmium ions in fluorophosphate glasses for photonic applications, in: AIP Conference Proceedings, AIP

Publishing, 2016.

[160] S.S. Aamlid, S.M. Selbach, T. Grande, Structural evolution of ferroelectric and ferroelastic barium sodium niobate tungsten bronze, Inorganic Chemistry, 59 (2020) 8514-8521.

[161] J. Varghese, R.W. Whatmore, J.D. Holmes, Ferroelectric nanoparticles, wires and tubes: synthesis, characterisation and applications, Journal of Materials Chemistry C, 1 (2013) 2618-2638.

[162] L. Liang, X. Kang, Y. Sang, H. Liu, One?dimensional ferroelectric nanostructures: synthesis, properties, and applications, Advanced Science, 3 (2016) 1500358.

[163] N. Setter, D. Damjanovic, L. Eng, G. Fox, S. Gevorgian, S. Hong, A. Kingon, H. Kohlstedt, N. Park, G. Stephenson, Ferroelectric thin films: Review of materials, properties, and applications, Journal of applied physics, 100 (2006).

[164] J. Zhang, Q. Guo, L. Liao, Y. Wang, M. He, H. Ye, L. Mei, H. Liu, T. Zhou, B. Ma, Structure and luminescence properties of La 6 Ba 4 (SiO 4) 6 F 2: Dy 3+ phosphor with apatite structure, RSC advances, 8 (2018) 38883-38890.

[165] D. Singh, J. Kaur, N. Suryanarayana, R. Shrivastava, V. Dubey, Synthesis and luminescent behavior of UV induced Dy 3+ activated LaAlO 3, Journal of Materials Science: Materials in Electronics, 28 (2017) 2462-2470.

[166] M.R. Babu, N.M. Rao, A.M. Babu, N. Jaidass, C.K. Moorthy, L.R. Moorthy, Effect of Dy3+ ions concentration on optical properties of lead borosilicate glasses for white light emission, Optik, 127 (2016) 3121-3126.

[167] I. Kashif, A. Ratep, Cool white light emission from Dy3+-doped SiO2-Bi2O3-Ga2O3-B2O3-GeO2-TeO2 glasses: Structural and spectroscopic properties, Materials Science and Engineering: B, 275 (2022) 115488.

[168] M. Mariyappan, K. Marimuthu, Concentration dependent spectroscopic properties of Dy3+ ions doped boro-phosphate glasses, in: AIP Conference Proceedings, AIP Publishing, 2016.

[169] D.R. Golja, M.M. Woldemariam, F.B. Dejene, J.Y. Kim, Photoluminescence processes in ?-phase Ba1. 3Ca0. 7-x-y SiO4: x D y 3+/y Tb3+ phosphors for solid-state lighting, Royal Society Open Science, 9 (2022) 220101.

[170] JOINT COMMITTEE ON POWDER DIFFRACTION STANDARDS, Analytical Chemistry, 42 (1970) 81A-81A.

[171] R. Choudhary, S. Koppala, S. Swamiappan, Bioactivity studies of calcium magnesium silicate prepared from eggshell waste by sol-gel combustion synthesis, Journal of Asian Ceramic Societies, 3 (2015) 173-177.